THE UNIVERSITY OF QUEENSLAND

AUSTRALIA

Gradient coil design and intra-coil eddy currents in MRI systems

Fangfang Tang

Bachelor of Engineering – Software Engineering

A thesis submitted for the degree of Doctor of Philosophy at

The University of Queensland in 2016

School of Information Technology and Electrical Engineering

Abstract

The work in this thesis is primarily concerned with the enhancement of gradient coil performance in magnetic resonance imaging (MRI). In MRI, gradient coils are used to produce gradient fields to spatially encode magnetic resonance signals. However, rapid switching on and off of the gradient coils induces fields and eddy currents in the human tissues and surrounding conducting structures. This thesis will provide novel solutions for the design of gradient coils and the reduction of eddy currents.

Gradient switching induces electric fields in human tissue that can cause safety problems, in particular peripheral nerve stimulation (PNS), which limits the gradient performance such as the slew rate and maximum gradient strength. One approach to solve this problem is to use local insertable gradient coils to achieve high gradient performance over localised regions of interest (ROI) yet not trigger PNS. Head only coils or head and neck coils are by far the most commonly used local coils. However, due to the constraints of the human head and shoulder, the head gradient coils are usually designed in an asymmetric configuration, with the region-of-uniformity (ROU) close to the patient end of the coil. This asymmetric configuration leads to technical difficulties in maintaining a high gradient performance for the head coil inserts given the very limited space available. Therefore, in this thesis, a practical configuration of an insertable asymmetric gradient head coil that offers improved performance was proposed. In the proposed design, at the patient end, the primary and secondary coils were connected using an additional radial surface, thus allowing the coil conductors distributed on the flange to ensure an improvement in the coil performance. At the service end, the primary and shielding coils were not connected, to permit access to shim trays, cooling system piping, cabling, and so on. It was found that with a similar field quality in the ROI, the proposed coil pattern improved construction characteristics (open service end, well-distributed wire pattern) and offers a better coil performance (lower inductance, higher efficiency etc.) than conventional head coil configurations.

Another obstacle to the advancement of MRI is the eddy currents induced in the surrounding conducting structures including the gradient coils themselves. The eddy currents induced in the surrounding conductors depend on the geometry of the conductor and the excitation waveform. These alternating fields caused by the switching gradient coils change the spatial profile of the current density within the coil tracks and surrounding coils with the applied frequencies of the input waveform and by their proximity to other conductors. Therefore, in this thesis, inductive coupling between coil tracks and gradient coils themselves was first investigated and then solutions for mitigation of the eddy current effects were provided.

First, the inductive coupling between coil tracks was studied, considering skin and proximity effects. In this investigation, the impact of the conductor width and the excited frequency over the parameters that characterise the performance of split transverse gradient coils was considered. A significant difference was found between the parameters calculated using filamentary coils and those obtained when the coil was simulated using finite size tracks. A coil with a wider track width produced superior efficiency and lower resistance than narrower tracks. It was demonstrated that rapidly changing current paths must be avoided in order to mitigate the power loss and the spatial asymmetry in the current density profile. The decision to use narrow or wide tracks in coils should be carefully investigated, and furthermore, a comprehensive temperature analysis is required that includes a detailed study of skin and proximity effects.

Second, the cross-talk between gradient coils was comprehensively investigated. It was found that the eddy currents induced in the un-energised coils (hereby referred to as passive coils) were positively correlated to track width and frequency. The magnetic field induced by the eddy currents in passive coils with wide tracks was several times larger than that induced by eddy currents in a cryostat cold shield. The power loss in the passive coils increased with the track width. The performance showed a significant difference taking into consideration the surrounding passive coils. Therefore, intra-coil interactions should be included in the coil design and analysis process, otherwise calculations of the coil performance are likely to be inaccurate.

Third, a novel solution was proposed for reducing the intra-coil eddy currents by applying a lamination technique on the coil tracks. With a slit coil configuration, the power dissipated by a passive coil with cuts was reduced significantly, thus reducing the total power and the impurity of the gradient field. Furthermore, the cutting of the coil tracks significantly improved coil performance such as the resistance, figure of merit (FoM), coil efficiency and so on.

The research described in this thesis suggests that it is critical to design MRI gradient coils taking into consideration eddy currents, and in particular, the skin and proximity effect and intra-coil eddy currents have to be taken into account during the analysis of gradient coil performance. The slitting of the coil track and local coil design are promising techniques to provide better engineering solutions for gradient coil design and development in MRI.

Declaration by author

This thesis is composed of my original work, and contains no material previously published or written by another person except where due reference has been made in the text. I have clearly stated the contribution by others to jointly-authored works that I have included in my thesis.

I have clearly stated the contribution of others to my thesis as a whole, including statistical assistance, survey design, data analysis, significant technical procedures, professional editorial advice, and any other original research work used or reported in my thesis. The content of my thesis is the result of work I have carried out since the commencement of my research higher degree candidature and does not include a substantial part of work that has been submitted to qualify for the award of any other degree or diploma in any university or other tertiary institution. I have clearly stated which parts of my thesis, if any, have been submitted to qualify for another award.

I acknowledge that an electronic copy of my thesis must be lodged with the University Library and, subject to the policy and procedures of The University of Queensland, the thesis be made available for research and study in accordance with the Copyright Act 1968 unless a period of embargo has been approved by the Dean of the Graduate School.

I acknowledge that copyright of all material contained in my thesis resides with the copyright holder(s) of that material. Where appropriate I have obtained copyright permission from the copyright holder to reproduce material in this thesis.

Publications during candidature

Peer-reviewed journal papers

1. **Fangfang Tang**, Feng Liu, Fabio Freschi,Yu Li, Maurizio Repetto, Luca Giaccone,Yaohui Wang, Stuart Crozier, An improved asymmetric gradient coil design for highresolution MRI head imaging, *Physics in Medicine and Biology, 2016* (accepted).

2. **Fangfang Tang**, Fabio Freschi, Maurizio Repetto, Yu Li, Feng Liu, Stuart Crozier, Mitigation of Intra-coil Eddy Currents in Split Gradient Coils for a Hybrid MRI-LINAC System, *IEEE Transaction on Biomedical Engineering, 2016* (accepted).

3. **Fangfang Tang**, Fabio Freschi, Hector Sanchez Lopez, Maurizio Repetto, Feng Liu, Stuart Crozier, Intra-coil interactions in split gradient coils in a hybrid MRI–LINAC system, *Journal of Magnetic Resonance*, vol. 269, pp. 203-212, 2016.

4. **Fangfang Tang**, Hector Sanchez Lopez, Fabio Freschi, Elliot Smith, Yu Li, Miguel Fuentes, Feng Liu, Maurizio Repetto, Stuart Crozier, Skin and proximity effects in the conductors of split gradient coils for a hybrid Linac-MRI scanner, *Journal of Magnetic Resonance*, vol. 242, pp. 86-94, 2014.

5. Yaohui Wang, Feng Liu, Yu Li, **Fangfang Tang**, Stuart Crozier, Asymmetric gradient coil design for use in a short, open bore magnetic resonance imaging scanner, *Journal of Magnetic Resonance*, vol. 269, pp. 203-212, 2016.

6. Fabio Freschi, Hector Sanchez Lopez, **Fangfang Tang**, Maurizio Repetto, and Stuart Crozier, Coupled magneto-thermal analysis of gradient coils in MRI scanners, *IEEE Transactions on Magnetics*, vol. 52, no. 3, pp. 1-4, 2016.

7. Fabio Freschi, Hector Sanchez Lopez, Elliot Smith, **Fangfang Tang**, Maurizio Repetto, and Stuart Crozier, Mixed-dimensional elements in transient thermal analysis of gradient coils, *Numerical Heat Transfer, Part A: Applications*, vol. 69, pp. 265-282, 2016.

8. Yaohui Wang, Feng Liu, Ewald Weber, **Fangfang Tang**, Jin Jin, Yas Tesiram, Stuart Crozier, "Acoustic analysis for a split MRI system using FE method," *Concepts in Magnetic Resonance Part B: Magnetic Resonance Engineering*, vol. 45, no. 2, pp. 85-96, 2015.

9. Hector Sanchez Lopez, Michael Poole, Adnan Trakic, Fabio Freschi, Elliot Smith, Jeremy Herbert, Miguel Fuentes, Yu Li, **Fangfang Tang**, Maurizio Repetto, Stuart Crozier, "Modal analysis of

currents induced by magnetic resonance imaging gradient coils," *IEEE Transactions on Magnetics*, vol. 50, pp. 945-948, 2014.

Conference abstracts

10. **Fangfang Tang**, Fabio Freschi, Maurizio Repetto, Feng Liu, Stuart Crozier, Crosstalk between gradient coils, in: *Proceedings of the International Society for Magnetic Resonance in Medicine*, 24, Singapore, 2016.

11. **Fangfang Tang**, Hector Sanchez Lopez, Fabio Freschi, Feng Liu , Yu Li, Stuart Crozier,Which is the impact of the coil track width and frequency over a split gradient coil performance? in: *Proceedings of the International Society for Magnetic Resonance in Medicine*, 22, Milan, Italy 2014.

12. Yu Li, **Fangfang Tang**, Bassem Henin, Fabio Freschi,Feng Liu, Stuart Crozier, Analysis of Eddy Currents for High Field RF Coil Design, in: *Proceedings of the International Society for Magnetic Resonance in Medicine*, 24, Singapore, 2016.

13. Yaohui Wang, **Fangfang Tang**, Yu Li, Feng Liu, Stuart Crozier, Theoretical investigation of gradient pulse alterations for acoustic noise reduction in an MRI-LINAC system, in: *Proceedings of the International Society for Magnetic Resonance in Medicine*, 24, Singapore, 2016.

14. Hector Sanchez-Lopez, **Fangfang Tang**, Stuart Crozier,A Robust guideline to design a split gradient coil for a hybrid Linac-MRI scanner, in: *Proceedings of the International Society for Magnetic Resonance in Medicine*, 22, Milan, Italy 2014.

15. Hector Sanchez-Lopez, **Fangfang Tang**, Stuart Crozier, Balancing a 500 mm central gap split gradient coil for a hybrid MRI-linac scanner, in: *Proceedings of the International Society for Magnetic Resonance in Medicine*, 22, Milan, Italy 2014.

16. Hector Sanchez-Lopez, Luca Zilberti, Oriano Bottauscio, Jeffrey Hand, Annie Papadaki, **Fangfang Tang**, Mario Chiampi, and Stuart Crozier, Heating of bilateral hip prostheses in a human body model induced by a multi-axis gradient coil set, in: *Proceedings of the International Society for Magnetic Resonance in Medicine*, 22, Milan, Italy 2014.

Publications included in this thesis

Publication citations – incorporated as Chapter 4.

Fangfang Tang, Feng Liu, Fabio Freschi,Yu Li, Maurizio Repetto, Luca Giaccone,Yaohui Wang, Stuart Crozier, An improved asymmetric gradient coil design for highresolution MRI head imaging, *Physics in Medicine and Biology*, *2016* (accepted).

Contributor	**Statement of contribution**
Fangfang Tang	Numerical modelling (100%), code implementation (100%), analysis and interpretation (90%), manuscript preparation (100%)
Feng Liu	Analysis and interpretation (5%), manuscript reviews (50%)
Fabio Freschi	Analysis and interpretation (5%), manuscript reviews (5%)
Yu Li	Manuscript reviews (10%)
Maurizio Repetto	Manuscript reviews (15%)
Luca Giaccone	Manuscript reviews (5%)
Yaohui Wang	Manuscript reviews (5%)
Stuart Crozier	Manuscript reviews (10%)

Publication citations – incorporated as Chapter 5.

Fangfang Tang, Hector Sanchez Lopez, Fabio Freschi, Elliot Smith, Yu Li, Miguel Fuentes, Feng Liu, Maurizio Repetto, Stuart Crozier, Skin and proximity effects in the conductors of split gradient coils for a hybrid Linac-MRI scanner, *Journal of Magnetic Resonance,* vol. 242, pp. 86-94, 2014.

Contributor	**Statement of contribution**
Fangfang Tang	Numerical modelling (40%), code implementation (40%), analysis and interpretation (45%), manuscript preparation (100%), experiment implementation (20%)
Hector Sanchez Lopez	Numerical modelling (40%), code implementation (20%),

	analysis and interpretation (20%), manuscript reviews (55%), experiment implementation (10%)
Fabio Freschi	Numerical modelling (20%), code implementation (40%), analysis and interpretation (20%), manuscript reviews (20%)
Elliot Smith	Experiment implementation (50%), manuscript reviews (5%)
Yu Li	Experiment implementation (10%)
Miguel Fuentes	Experiment implementation (10%)
Feng Liu	Analysis and interpretation (5%), manuscript reviews (10%)
Maurizio Repetto	Analysis and interpretation (5%), manuscript reviews (5%)
Stuart Crozier	Analysis and interpretation (5%), manuscript reviews (5%)

Publication citations – incorporated as Chapter 6.

Fangfang Tang, Fabio Freschi, Maurizio Repetto, Feng Liu, Stuart Crozier, Crosstalk between gradient coils, in: *Proceedings of the International Society for Magnetic Resonance in Medicine*, 24, Singapore, 2016.

Contributor	**Statement of contribution**
Fangfang Tang	Numerical modelling (80%), code implementation (80%), analysis and interpretation (60%), manuscript preparation (100%)
Fabio Freschi	Numerical modelling (20%), code implementation (20%), analysis and interpretation (10%), manuscript reviews (30%)
Maurizio Repetto	Analysis and interpretation (10%), manuscript reviews (40%)
Feng Liu	Analysis and interpretation (10%), manuscript reviews (20%)
Stuart Crozier	Analysis and interpretation (10%), manuscript reviews (10%)

Fangfang Tang, Fabio Freschi, Hector Sanchez Lopez, Maurizio Repetto, Feng Liu, Stuart Crozier, Intra-coil interactions in split gradient coils in a hybrid MRI-LINAC system, *Journal of Magnetic Resonance*, vol. 269, pp. 203-212, 2016.

Contributor	**Statement of contribution**
Fangfang Tang	Numerical modelling (60%), code implementation (50%), analysis and interpretation (40%), manuscript preparation (100%)
Fabio Freschi	Numerical modelling (30%), code implementation (50%), analysis and interpretation (20%), manuscript reviews (30%),
Hector Sanchez Lopez	Numerical modelling (10%), analysis and interpretation (10%), manuscript reviews (10%)
Maurizio Repetto	Analysis and interpretation (10%), manuscript reviews (10%)
Feng Liu	Analysis and interpretation (10%), manuscript reviews (40%)
Stuart Crozier	Analysis and interpretation (10%), manuscript reviews (10%)

Publication citations – incorporated as Chapter 7.

Fangfang Tang, Fabio Freschi, Maurizio Repetto, Yu Li, Feng Liu, Stuart Crozier, Mitigation of Intra-coil Eddy Currents in Split Gradient Coils for a Hybrid MRI-LINAC System, *IEEE Transaction on Biomedical Engineering, 2016* (accepted).

Contributor	**Statement of contribution**
Fangfang Tang	Numerical modelling (80%), code implementation (80%), analysis and interpretation (50%), manuscript preparation (100%), experiment implementation (30%)
Fabio Freschi	Numerical modelling (20%), code implementation (20%), analysis and interpretation (20%), manuscript reviews (25%), experiment implementation (10%)

Maurizio Repetto	Analysis and interpretation (10%), manuscript reviews (40%), experiment implementation (20%)
Yu Li	Experiment implementation (40%), manuscript reviews (5%)
Feng Liu	Analysis and interpretation (10%), manuscript reviews (20%)
Stuart Crozier	Analysis and interpretation (10%), manuscript reviews (10%)

Contributions by others to the thesis

Prof. Feng Liu (primary supervisor), Prof. Stuart Crozier (associate supervisor), Hector Sanchez Lopez (ex-associate supervisor), Associate Prof. Fabio Freschi (collaborator), Prof. Maurizio Repetto (collaborator), and Dr Yu Li (colleague) have all made contributions towards generating research ideas, experimental design, data collection and the interpretation of the simulation results. Their individual contributions are detailed in the previous section and are listed at the beginning of Chapters 4–6. All work presented in the remainder of this thesis (Chapters 1, 2, 3 and 8) was drafted entirely by the author. Prior to submission, the thesis was reviewed by all PhD supervisors with corrections being made by the author.

Statement of parts of the thesis submitted to qualify for the award of another degree

None

Acknowledgements

I would like to take this opportunity to express my gratitude to all those that have helped me during my PhD study.

First and foremost, I would like to thank my supervisors Prof. Feng Liu, Prof. Stuart Crozier, and Dr Hector Sanchez Lopez (ex- associate supervisor) for providing me this great opportunity to work in such an excellent research environment. I am particularly grateful for Feng Liu's patience and the immeasurable time he has spent providing me with invaluable insights into magnetic resonance imaging technology. Thanks to Stuart Crozier for the insightful discussions, meticulous editing and encouragement. Special thanks go to Hector Sanchez Lopez for helping me when I first stepped in this new area and for his solid contributions and great communication in projects we have worked on together.

I am extremely grateful to Fabio Freschi and Maurizio Repetto for their professional guidance and incredible support throughout my study. They have provided me with a lot of mathematical input, in both modelling and analytical computations. I also want to thank them for the time they have devoted to me and for the discussions we shared during their visit to UQ and via Email and Skype. Their patience, enthusiasm and immense knowledge have been priceless treasures throughout my PhD study.

I also acknowledge Yu Li for his assistance in the experimental validation of my method. I would like to thank all colleagues in our group: Dr Adnan Trakic, Mr Miguel Fuentes, Mr Elliot Smith, Ms Yanmin Zhu, Mr Ewald Weber, Mr Yang Yang, Mr Yaohui Wang, Dr Jin Jin, and Dr Mingyan Li for their advice and suggestions. Special appreciation is extended to Ms Kimberley Nunes and Ms Celia Giumelli, who have given their generous help and kind advice in regard to all my paperwork during my study.

The research in this thesis was funded by a CSC–UQ (China Scholarship Council–The University of Queensland) PhD Scholarship and the Top Up Assistance Program. I am also appreciative of support in the form of travel grants from the University of Queensland and the International Society for Magnetic Resonance in Medicine.

Last, but not least, I would like to thank my parents, my brother and my husband for their love, understanding and endless encouragement.

Keywords

Gradient coil design, skin and proximity effects, split-gradient coil, intra-coil eddy currents, cross-talk, gradient performance, slit coil tracks, electromagnetic interactions, insertable head coil, asymmetric configuration.

Australian and New Zealand Standard Research Classifications (ANZSRC)

ANZSRC code: 090304, Medical Devices, 50%

ANZSRC code: 090399, Biomedical Engineering not elsewhere classified, 50%

Fields of Research (FoR) Classification

FoR code: 0903, Biomedical Engineering, 60%

FoR code: 0906, Electrical and Electronic Engineering, 40%

Contents

List of Figures

List of Tables

List of Abbreviations

MRI	magnetic resonance imaging
MR	magnetic resonance
LINAC	linear accelerator
DSV	diameter of spherical volume
PET	positron emission tomography
NMR	nuclear magnetic resonance
RF	radio frequency
FID	free induction decay
ROI	region of interest
CT	computed tomography
FOV	field-of-view
SNR	signal-to-noise
IGRT	image-guided radiotherapy
EPI	echo planar imaging
FoM	figure of merit
FEM	finite element
FDTD	finite difference time domain
3D	three-dimensional
BEM	boundary element method
MIM	multi-layer integral method
ROU	region-of-uniformity

HGV	homogeneous-gradient-volume
EMC	equivalent magnetisation current method
ARC	Australian Research Council
PNS	peripheral nerve stimulation
T	Tesla

1. Introduction

This opening chapter outlines the technology behind magnetic resonance imaging (MRI), and particularly discusses the challenging technical problems relevant to the existing gradient coil system with a view to improve the performance of the gradient coils. The technical problems and the motivation for this study will first be introduced in section 1.1, followed by the scope of this thesis in section 1.2.

1.1 Research Problem and motivation

MRI technology has developed rapidly since the 1970s and has become a powerful medical imaging technique. The significant technological development of MRI has been motivated by its ability to produce high resolution images of soft tissue contrast. MRI is a widely used imaging technique to assist in diagnosis of diseases or other issues with the brain or other early clinical diagnosis especially for oncology, cardiovascular and neurological diseases [1].

The principal components of the MRI scanner include the main magnet, gradient coils and radio frequency (RF) coils. The main magnet is used to produce a homogeneous static magnetic field to stimulate the hydrogen protons in water within the human body to align with the field. The RF coils are applied to excite and receive electromagnetic signals emitted by the protons. To obtain MR images from the resonant radio signals detected by RF systems, gradient coils are needed to encode the positions of the signals. An essential part of MRI scanners, the gradient coil set plays an important role in determining how fast and accurately an image is obtained [1]. Gradient coils are driven by pulsed current to produce linear and uniform gradients in the ROI to encode spatial information. Instead of being energised all the time, gradient coils are switched on when required for signal collection, therefore, they are switched on and off rapidly. The rapid switching gradient coils generates a changing magnetic field, thus inducing an electric field in the human tissues and eddy currents in the surrounding conductors because of their inductive properties.

The electric field induced in the human body can result in undesirable PNS [2, 3], which limits the gradient performance such as its strength and slew rate [4]. However, some techniques such as echo planar imaging (EPI) and diffusion imaging require enhanced gradient coils with rapid switching speed and high gradient strength to improve the imaging speed and diffusion contrast [5]. An approach to enhance gradient capacities without the onset of PNS is to use local gradient coils. As smaller gradient coils produce less magnetic flux than the whole-body coils, therefore, local coils can be switched faster than whole-body

coils without causing PNS [6-8]. Although local gradient coils have been demonstrated to be faster and more effective to achieve high performance and high gradient strength compared to the whole-body gradient coils [4, 9, 10], the applications of head coils have been restricted by the coil design and implementation [5]. Because the local gradient coils such as head coil inserts are designed to be asymmetric due to constraints from the dimensions of human shoulders and head, this leads to technical difficulties in maintaining a high gradient performance for the head coil inserts with very limited space. Therefore, the asymmetric gradient coil inserts need to accommodate the patient geometry as well as achieve coil performance.

Eddy currents induced in the surrounding conducting materials are another deleterious effect caused by the rapid switching gradient coils. The time-varying gradient field produced by the switched gradient coils induces undesirable time-varying eddy currents in the nearby conductive materials such as cryostat, RF shield and the gradient coils themselves. These eddy currents result in many deleterious effects, such as ohmic heating, mechanical vibration and acoustic noise in conductive parts in MRI scanners [11, 12]. Moreover, the secondary magnetic field generated by the eddy currents leads to perturbations on the expected gradient field, resulting in image artefacts, ghosting, compression and other distortions [13, 14]. Because of the degradation effects, eddy currents are considered one of the major bottlenecks in the design and construction of MRI scanners [11, 15], and therefore need to be controlled as much as possible. Nevertheless, it is difficult to predict the eddy currents, especially in the gradient coils themselves, because of the geometrical complexity of the coils. Moreover, the intra-coil eddy currents cannot be neglected due to their deleterious effects, especially when wide windings and tracks are used for power dissipation purposes in modern MRI scanners [16-18]. Furthermore, the intra-coil eddy currents are more accentuated in fast sequences, such as the aforementioned EPI. Therefore, the eddy currents induced in the coil tracks and in the surrounding coils need to be investigated in detail and mitigated as much as possible.

1.2 Objective and scope

As mentioned above, rapid switching of the gradient coils induces electric fields in the human body and eddy currents in the nearby conductors. The induced electric fields in human tissues may cause PNS, which can be mitigated or eliminated by the use of local gradient coils such as head coil inserts. But because of the constraints of the anthropometry data, the head coil inserts are usually designed to be of an asymmetric configuration, which degrades the coil performance. Another problem caused by the

switching gradient coils—eddy currents between the coil tracks and gradient coils which have been neglected in the previous studies. Therefore, this thesis aims to investigate the following research topics:

- To improve electromagnetic performance of asymmetric head gradient coils: a novel and practical coil configuration of asymmetric head gradient coil insert will be proposed to offer improved performance for human brain imaging.
- To investigate inductive coupling between coil tracks in a gradient coil system: the interactions between the gradient coil tracks will be theoretically/experimentally studied with the consideration of skin and proximity effects.
- To study cross-talk between gradient coil sets: interaction between gradient coils will be investigated in detail, with the consideration of track widths and frequencies.
- To mitigate cross-talk between coils: based upon the above electromagnetic interaction studies, novel engineering solutions for mitigating eddy current and system component coupling will be proposed.

This thesis is made up of two major parts. The first part in Chapters 2 and 3 introduces the underlying principles and methods related to the research interests. Then the details of the research are presented in Chapters 4–7. Outlines of individual chapters are as follows:

Chapter 2 provides some basic physical principles of MRI systems that are required to understand the rest of the thesis. Nuclear magnetic resonance (NMR) and its application in magnetic resonance imaging (MRI) systems is described. Then, diagrams present the hardware components of an MRI system and a hybrid MRI-linear accelerator (LINAC) system. Particular attention is paid to the gradient coils and the nature of the complex interactions of the gradient field with other conductors.

Chapter 3 covers a mathematical characterisation of the equivalent magnetisation current (EMC) and the multi-layer integral method (MIM), which are engaged to design the gradient coils used in this thesis and to analyse the designed gradient coils.

Chapter 4 presents a design of whole-body head gradient coil inserts using the coil design method mentioned in Chapter 3. Novel one-end-connect asymmetric head gradient coils will be designed and compared with the conventional asymmetric coils. The performance of the head coils as a function of the distance between the coil edges and the ROU will also be analysed.

Chapter 5 discusses the eddy currents between the tracks of the gradient coils in a conventional whole-body MRI system and an MRI-LINAC system. The impact of the coil track width and the frequency on the coil performance taking into account skin and proximity effects for transverse gradient coils will be studied. The work will also compare the differences in the analyses of gradient coils using filamentary and finite track widths.

Chapter 6 details the intra-coil eddy currents in terms of different track widths and frequencies. The eddy currents induced in the surrounding coils and cold shield will be compared to demonstrate the importance of the intra-coil eddy currents. The study in this chapter provides an insight into the effect of coil track widths on the intra-coil eddy currents in the conventional MRI scanner and MRI-LIANC system.

Chapter 7 describes a solution for mitigating the intra-coil eddy currents studied in Chapter 6 by slitting the coil tracks along the direction of the current flow. The impact of the slits on the energised and surrounding un-energised coils will be investigated in detail. This work will provide a detailed theoretical analysis of the benefits of slitting the coil tracks.

Chapter 8 draws conclusions and discusses possible future works.

2. Basic principles

The phenomenon of nuclear magnetic resonance (NMR) was first discovered by Felix Bloch [19] and Edward Purcell [20] independently in 1946. Magnetic resonance imaging techniques were developed from the original NMR phenomenon from the 1970s, when Paul Lauterbur and Sir Peter Mansfield employed gradients to localise the resonating nuclei to obtain the first MR images. This technical development has been motivated by the tremendous use MR images are in clinical diagnosis and treatment because of their excellent soft tissue contrast, non-ionising nature and the high resolution images that can be produced. MRI with powerful imaging capability has proven to be a reliable biomedical device in the early diagnosis of many diseases.

To understand the research presented in this thesis, it is essential to discuss the basic physical principles and instrumentation of MRI. First, the phenomenon of NMR is briefly described in Section 2.1, followed by the formation of MR images in Section 2.2, and then the major system components of standard MRI systems and hybrid MRI-LINAC systems are explained in Section 2.3. Lastly, a full review of gradient coils, which are of essential components of MRI scanners, is given in Section 2.4.

2.1 Nuclear Magnetic Resonance

As MRI is based on the phenomenon of NMR, to understand MRI, we first must understand the basic physical principles of NMR. This section outlines the basic NMR theory.

2.1.1 Spin and Magnetisation

In quantum mechanics, atomic nuclei consist of elementary particles like neutrons and protons which exhibit the intrinsic quantum property of spin, which is the fundamental property of nature [21]. Atoms with even numbers of neutrons and protons have zero spin. And all atoms with an odd number of nucleons such as 1H in water exhibit a non-zero spin with angular momentum. 1H in water is an ideal media particle for spin based on NMR, because water is the most abundant constituent of the human body.

The magnetic moment of the water hydrogen is randomly oriented as shown in Figure 2.1a, therefore, the macroscopic magnetic moment is zero before impressing the external field. With the external magnetic field B_0 applied, by convention in the z direction, each spinning proton tends to align itself with (parallel to) or against (anti-parallel to) the direction of the applied field B_0 (Figure 2.1b).

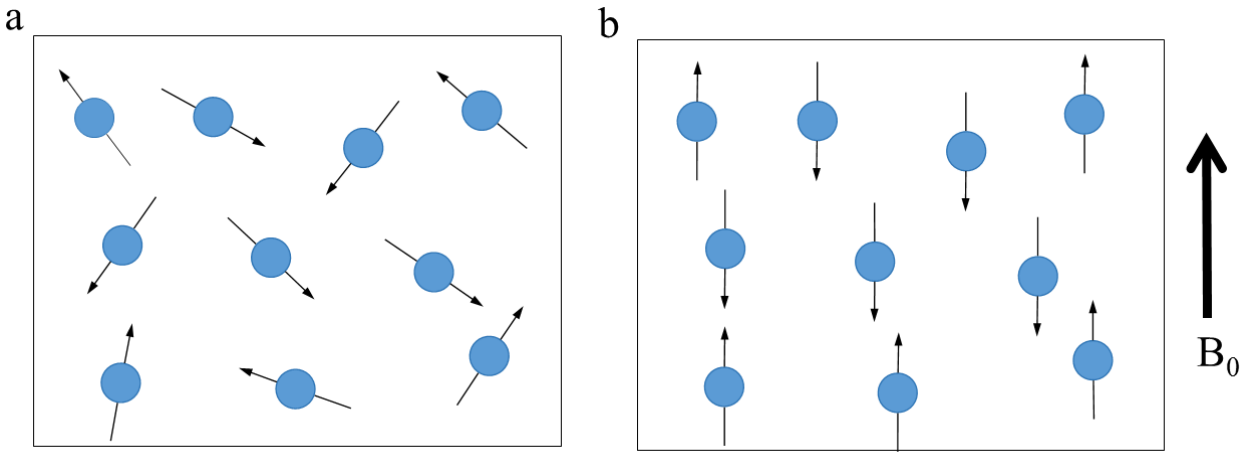

Figure 2.1 (a) The random water hydrogen protons orient in random directions resulting in a zero microscopic magnetic moment in the absence of the external magnetic field, (b) the random water hydrogen protons are parallel or anti-parallel to the direction of B_0 resulting in a non-zero magnetic moment.

The alignment directions are determined by the states of the protons: high energy level or and low energy level (Figure 2.2). The energy is related to the external magnetic field, which is called Zeeman energy [22]:

$$E_{parallel} = -\frac{1}{2}\hbar\gamma B_0$$
$$E_{anti-parallel} = \frac{1}{2}\hbar\gamma B_0 \qquad (2.1)$$

where $\hbar$ = 6.629 $\times 10^{-34}$ J s is called Planck's constant, and γ is the gyromagnetic ratio (γ = 2.657×10^{8} $s^{-1}T^{-1}$ for ^{1}H). From Boltzmann's law [23], the ratio of the number of the two states anti-parallel and parallel can be expressed by the energy level difference ΔE:

$$\frac{N_{anti-parallel}}{N_{parallel}} = e^{\frac{-\Delta E}{kT}} = e^{\frac{E_{parallel}-E_{anti-parallel}}{kT}} = e^{\frac{-\hbar\gamma B0}{kT}} \quad (2.2)$$

where k = 1.3806 $\times 10^{-23}$ J K^{-1} is the Boltzmann's constant and T is the absolute temperature. At the temperature of 20℃,ΔE and kT are in the order of 10^{-26} and 10^{-21}, respectively. Thus, Eq.(2.2) can be approximated as:

$$\frac{N_{anti-parallel}}{N_{parallel}} \approx 1 + \frac{\hbar\gamma B_0}{kT} \quad (2.3)$$

In thermal equilibrium, the net magnetic moments per unit volume (magnetisation M_0), are proportional to the difference in the numbers of the nuclei in the parallel and anti- parallel directions [24, 25]:

$$M_0 \approx (N_{anti-parallel} - N_{parallel})N \approx \frac{N\hbar\gamma B_0}{2kT} = \frac{\hbar\gamma}{2}\frac{\rho\hbar\gamma B_0}{2kT} = \frac{\rho\hbar^2\gamma^2 B_0}{4kT} \quad (2.4)$$

where ρ is proton density. The net magnetisation M_0 is the signal source of the MR imaging. As the magnetisation is proportional to the external magnetic field strength, a straightforward way to improve the image quality is to raise the external magnetic field strength B_0 [26, 27]. However, there are some challenges when using a high-field MRI, such as keeping the constant homogeneity of B_0 and ensuring patient safety [28, 29] that are difficult to realise at 7 Tesla and above.

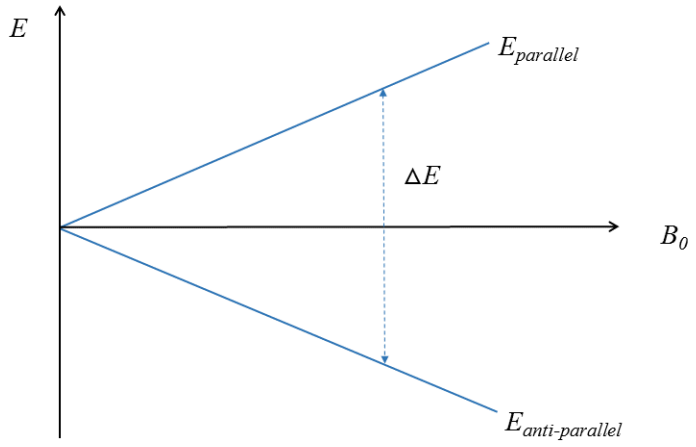

Figure 2.2 The energy levels caused by a static magnetic field

2.1.2 NMR signals

As described in Section 2.1.1, the spinning protons tend to parallel to or anti-parallel to the direction of the external field B_0, however, when the magnetisation of the nuclei is not perfectly parallel to B_0, the nuclei will experience a torque, leading to their rotation around the direction of B_0 (Figure 2.3). This is called the Larmor precession, which is expressed as $\omega = \gamma B_0$, where ω is the angular velocity of the procession, and γ is the gyromagnetic ratio.

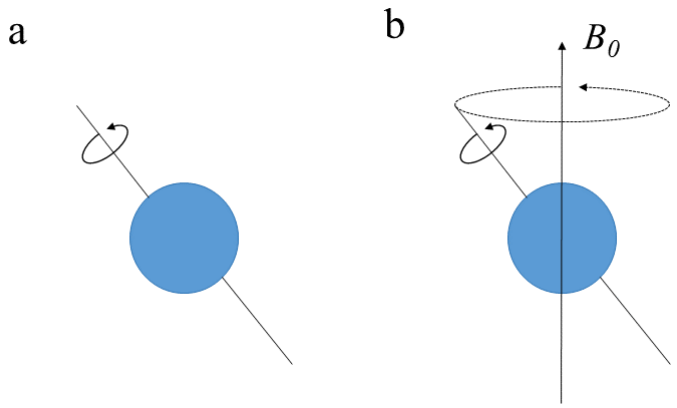

Figure 2.3 (a) the nuclei spinning in the absence of an external field, (b) the spinning nuclei experience a toque in the presentence of the applied external magnetic field.

When applying RF pulses at the Larmor frequency, the nuclei absorb or emit photons to change spin states, and the protons at low energy level absorb RF energy and transit to a high energy level. The oscillating electromagnetic field B_1 produced by the RF excitation, which is perpendicular to the static magnetic field B_0, will produce a torque on the net magnetisation. Therefore, M_0 is not along the *z*-axis, but a spiral movement towards the transverse plane as shown in Figure 2.4.

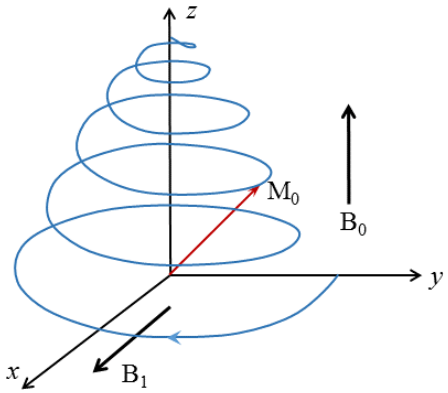

Figure 2.4 The net magnetisation flipped by RF pulses.

After the application of the RF pulses, all the nuclei return to their initial states, and the net magnetisation will recover to its original values, this process is called relaxation. After a 90 ° pulse, the net magnetisation can be decomposed into longitudinal and transverse components, therefore causing two types of relaxation: longitudinal relaxation (*T1*, also known as spin-lattice relaxation) and transverse relaxation (*T2*, also known as spin-spin relaxation). The change in the magnetisation induces an electrical current in a nearby receiver coil (orthogonal to the *XY* plane) according to Faraday's Law, and this current signal called a free induction decay (FID, Figure 2.5) signal carries all the NMR information and can be used for creating images.

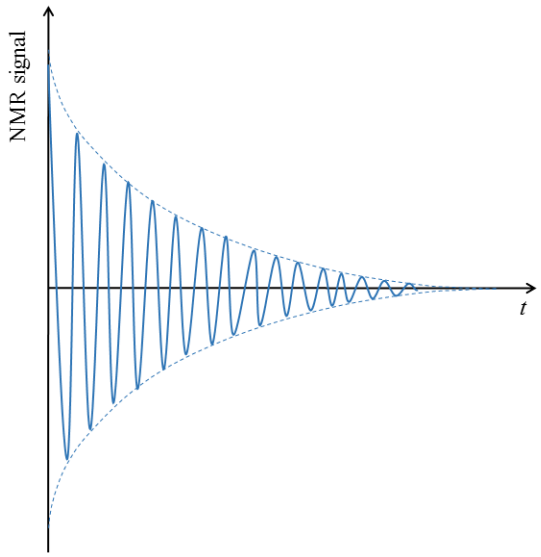

Figure 2.5 The free induced decay (FID) signal.

2.2 Magnetic Resonance Imaging

The B_1 field produced by the radiofrequency coils excites a volume of nuclei spins regardless of the positions of the nuclei in the Cartesian coordinate system. To provide the positions of the NMR signals to obtain the MR images, a localisation method called gradient field is superimposed on the uniform static magnetic field B_0. The gradient field is a small linear and homogeneous magnetic field that is applied to ensure the total field of each spatial element is unique in the ROI.

2.2.1 Gradients

In MRI, three orthogonal linear gradient fields are applied within an ROI in order to provide the spatial information of the MR signals. The spatial variations are generated by a set of specially designed gradient coils. The *z*-component of the magnetic field varies linearly along the *x*, *y* and *z* directions, which are defined as:

$$Gx = \frac{dB_z}{dx}, Gy = \frac{dB_z}{dy}, \text{and } Gz = \frac{dB_z}{dz} \tag{2.5}$$

where G_x (Figure 2.6a) and G_y (Figure 2.6b) are transverse gradients, which are also called phase encoding and frequency encoding gradients, and G_z (Figure 2.6c) is known as the longitude gradient and also called the slice selection gradient. The ideal gradient fields should be uniform along each axis in the ROI for imaging purposes.

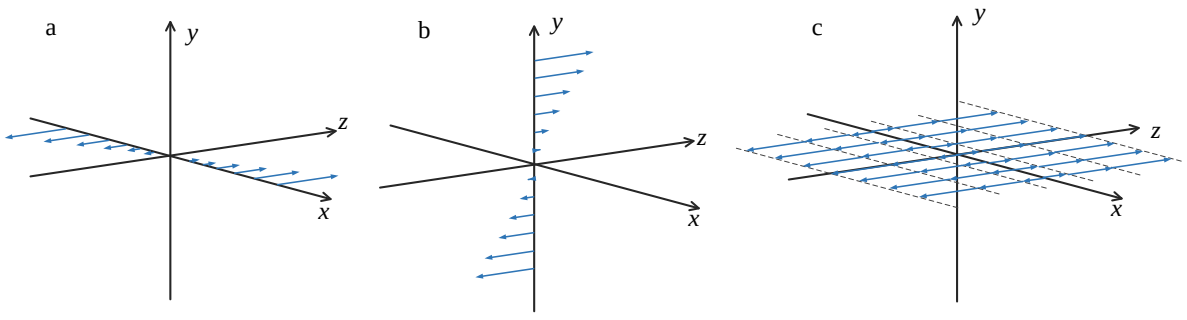

Figure 2.6 Gradient field B_z in a slice, (a) *x*-field, (b) *y*-field, (c) *z*-field. The field is along the arrow direction and the length of the arrows indicate the magnitude of the magnetic field at the corresponding points.

2.2.2 Slice selection

To excite the desired slice in MR imaging, it needs a slice-selection gradient and an RF-pulse applied. The imposed gradient is in the direction perpendicular to the plane of the slice [30]. If we assume we are selecting a slice at place z_0, the gradient field is imposed on the main magnetic field, thus the field $B_{z,\,total} = B_0 + zG_z$, so in order to excite the slice, an RF pulse which is centred around $\omega_0 = \gamma(B_0 + z_0G_z)$ and a bandwidth of $\Delta\omega = \gamma\Delta zG_z$ are needed. The particular RF pulse in the range of $\omega_0 - \Delta\omega/2 < \omega < \omega_0 + \Delta\omega/2$ can only excite the nuclei in the range of $z_0 - \Delta z/2 < z < z_0 + \Delta z/2$, and the outside spins will not be affected by this RF pulse. It can be seen from Figure 2.7 that the slice thickness depends on the excitation frequency and the gradient strength, and to achieve a thinner slice, a narrower RF bandwidth and a stronger gradient strength are needed [31].

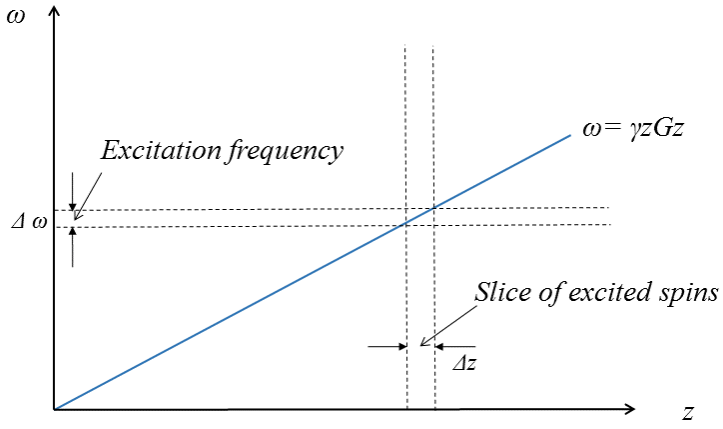

Figure 2.7 Illustration of a slice selection.

2.2.3 Frequency and Phase Encoding

In order to determine the spatial position within the slice or between the slices, other gradients are needed to reconstruct the two-dimensional image of a slice and three-dimensional images based on a combination of successive slices. Therefore, the frequency gradient *Gx* is turned on and this gradient field varies linearly along the *x*-axis as shown in Figure 2.6a and is superimposed over the static magnetic field, thus the total magnetic field is $B_{z,\,total} = B_0 + xGx$. Thus, the frequency encoding gradient can produce a one-dimension image of the selected slice of the subject, whereas for multidimensional localisation, multiple encoded signals are needed.

Since the *x*-gradient is turned on during the FID recording process, it is also called read-out gradient.

Finally, a third gradient called a phase encoding gradient is imposed to read the signals along the *y*-direction, and is therefore called the *y*-gradient. Using the *y*-gradient, a two-dimension image can be reconstructed from the selected slice and three-dimensional images can be created using a combination of successive slices.

2.3 The MRI scanner

2.3.1 Standard MRI system overview

As described previously, an external field B_0 is needed for nuclei magnetisation (Section 2.1.1), an oscillating electromagnetic field B_1 is required for transmitting and receiving signals (Section 2.2.2) and a gradient field is required for encoding the spatial information from the signals (Section 2.3) to produce MR imaging. To generate the desired fields, an MRI scanner employs three important components: a main magnet to produce the static magnetic field, gradient coils to create the gradient field and a radio frequency coil to create the radiofrequency (RF) field (see Figure 2.8). MRI uses the interaction between the fields and hydrogen atoms to produce detailed images of internal human structures. So, in terms of ionising radiation, MRI is safer than other imaging techniques such as *x*-ray, computed tomography (CT) and Positron Emission Tomography (PET) [1].

The external static magnetic field B_0 is produced by permanent magnets or superconducting electromagnets. Permanent magnets are made of ferromagnetic materials and do not require an extra power supply but they are extremely bulky. Superconducting magnets are the most commonly used in MRI applications because the fields they produce are stronger, more homogenous and more stable as compared to permanent magnets. In superconducting magnets, the windings are immersed in liquid helium at a temperature of 4 Kelvin [32]. Therefore, there are usually three conductive layers called cryostat outside of the helium vessel to help to maintain the low temperature of the liquid helium.

The gradient coils are used to spatially encode the positions of the signals emitted by the excited spinning protons. Three orthogonal linear gradient fields are created along *x*, *y* and *z*-directions

with a gradient strength in the order of tens of *mT/m* in a field-of-view (FOV) (shown in Figure 2.6) for the purpose of slice selection, frequency encoding and phase encoding as described in section 2.2.

The RF coils create the pulse excitation, rotate the net magnetisation and collect the signals emitted by the nuclei during the magnetisation recovery process. There are three types of RF coils: transmit only coils, receive only coils, and transmit and receive coils. The transmit coils generate field B_1 in the FOV, which is perpendicular to the main magnetic field B_0. To ensure the image quality, B_1 should be homogeneous in the FOV at Larmor frequency. When the RF coil is used as a receiving coil, it must have a high signal-to-noise (SNR) ratio. So the transmit and receive coils must produce uniform fields and at the same time maintain a high SNR.

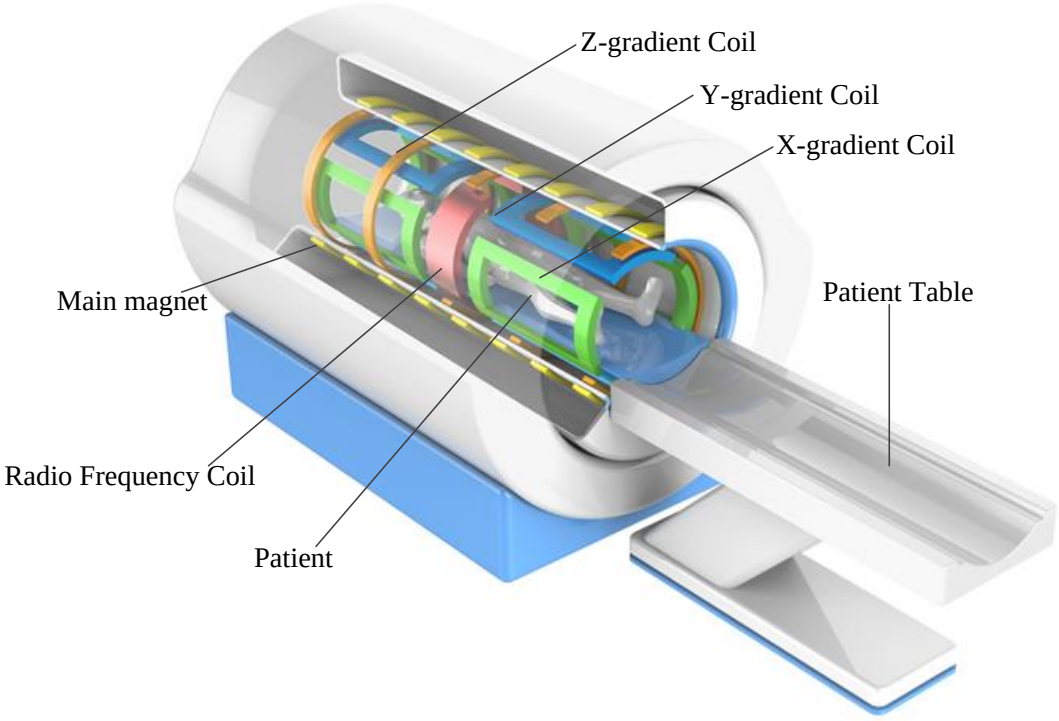

Figure 2.8 A simplified MRI system with cut-away section.

2.3.2 MRI-LINAC system

MRI is attractive for the visualisation of both tumours and surrounding organs, as it can provide accurate anatomical images because of its excellent soft tissue contrast [33, 34]. Radiation therapy has been shown to be an effective way to kill tumours or malignant tissue; therefore,

integrating the equipment used for radiation therapy into an MRI scanner can provide accurate information about a tumour's shape and position for accurate diagnosis and treatment.

In radiation therapy, a linear accelerator (LINAC) is applied to deliver radiation from outside the body directly towards the tumour or cancer and the surrounding tissues where it is possible the cancer has spread. However, during the treatment process, the tumours can move with the movement of the human body or organs. This may lead to the tumour receiving less radiation than planned or the surrounding healthy tissues receiving higher doses of radiation. To provide the exact position of the tumours and thus improve the accuracy of the dose of radiation being applied, the imaging technique can be used during the treatment; this is called image-guided radiotherapy (IGRT) [35]. Techniques based on cone-beam or megavolt computed tomography (CT) [36-38], ultrasound [39, 40] and positron emission tomography (PET) scanning [41, 42] have presented their capabilities of IGRT. The main problem in IGRT is still the limited visibility of the tumour and producing real-time intrafraction imaging [43].

Because of the advantages of its excellent soft tissue contrast, combining an MRI scanner with a radiation therapy LINAC system has motivated researchers to improve IGRT technology [43, 44]. A hybrid MRI-LINAC system has the capacity to image moving tumours and direct the radiation beam to follow this motion and therefore continue to target the tumour throughout the treatment procedure. Potential advantages of the combined system on intrafractional tumour tracking were reported by the authors in [45, 46].

So far, there are three types of combined MRI and LINAC apparatuses. One type mounts the LINAC onto an opened bi-planar MRI system, and the radiation beam is aimed through the space between the magnets. In another design which integrates a 1.5 T MRI and an accelerator [43, 47-49], the radiation beam travels through the MRI system before entering the patient, leading to beam attenuation and scatter, thus affecting the accuracy of the radiation therapy [48]. Another design compromises by splitting the magnetic resonance (MR) magnet and gradient coils into two halves to allow the insertion of the accelerator [44, 50-53], and consequently the radiation beam can travel through the gap between the halves or in the bore of the MRI scanner as shown in Figure 2.9. However, splitting the MRI system creates challenges in regard to the performance of the magnet and gradient coils, especially the gradient coils which will be covered in more detail in Section 2.4 [54].

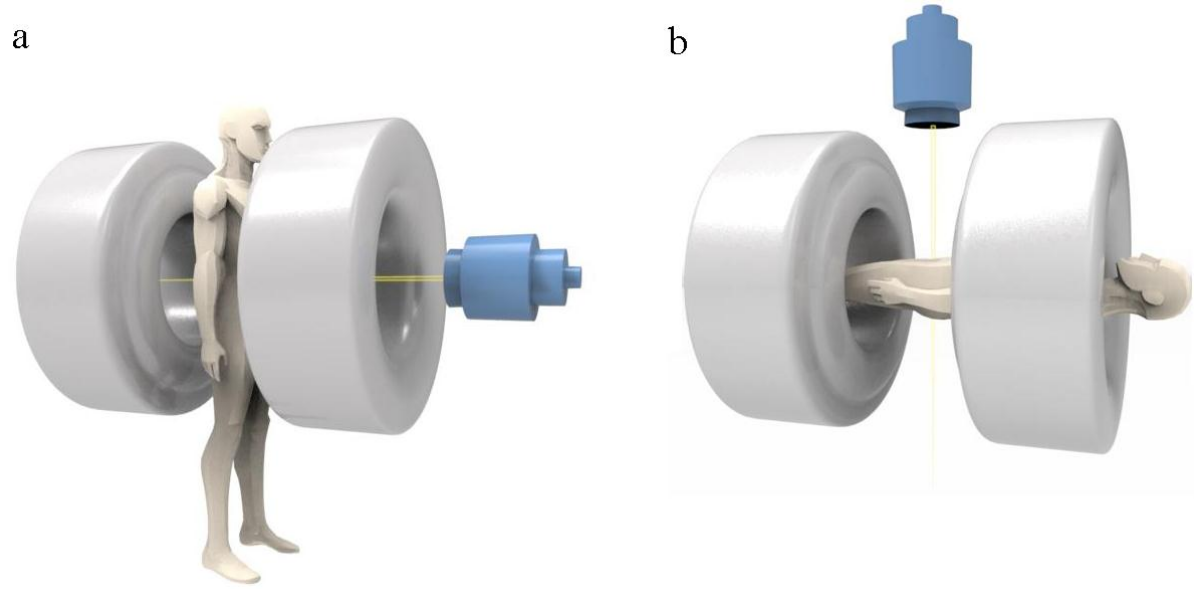

Figure 2.9 Schematic representation of the MRI-LINAC system, (a) the treatment beam aligned with main magnet B_0, (b) the LINAC is perpendicular to B_0.

2.4 Gradient coils

2.4.1 Introduction to gradient coils

As an important part of MRI, gradient coils provide spatial encoding to the nuclear magnetic resonance signals emitted from magnetised hydrogen protons in human tissues. They also play an important role in determining how fast and accurately an image is obtained. In order to generate a linear gradient field as described in Section 2.2.1, gradient coils are appropriately arranged conductors carrying passing electric current. Gradient coils are usually made of copper sheets wound around the surface of a cylinder and casted in epoxy resins [55]. The copper sheets are etched with an appropriate pattern such as strips, circular loops, arcs and their combinations, with track width varying from a few millimetres to a few centimetres.

Gradient coils are driven by electric current to produce the three orthogonal gradient fields as shown in Figure 2.6. The transverse gradients G_x and G_y are produced by the transverse x and y-gradient coils. The y-gradient coil can be obtained by rotating the x-coil by 90 ° along the z-axis. The longitude gradient field is produced by the longitude z-coil (Figure 2.10).

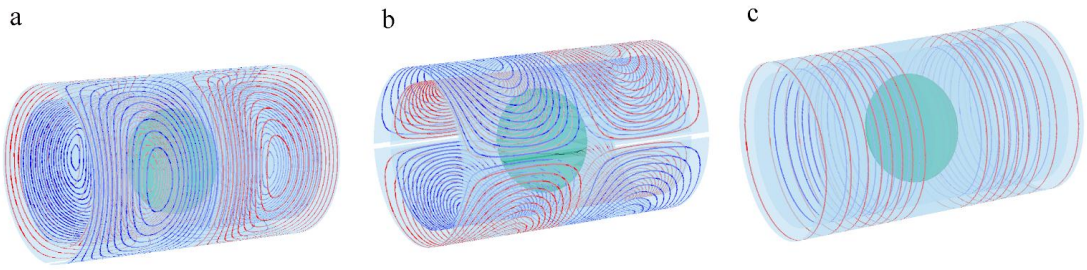

Figure 2.10 Conventional gradient coil patterns, (a) *x*-coil, (b) *y*-coil, (c) *z*-coil.

2.4.2 Split gradient coils

As described in Section 2.3.2, combining an MRI system and a LINAC system can provide IGRT in real-time during the treatment of the tumours. However, in an MRI-LINAC system, the gradient coils have to be split into two halves to accommodate the human body or the LINAC system [50, 53]. This precludes the use of conventional cylindrical gradient coils and the performance of the coils is inevitable reduced [56]. For instance, in splitting gradient coils, high wire density is needed in the central region to maintain the gradient strength, thus the stored magnetic energy produced by the coil increases with the central gap [57]. A high current must be applied to maintain the gradient strength and that requires more powerful amplifiers. High wire density and current density can potentially produce hot spots in the coils [50].

For example, in the traditional split whole-body gradient coils designed to minimise the force/torque exerted by the magnetic fields and to minimise the eddy currents, the current density was found to be higher and the coil efficiency lower than for the conventional non-split coils [50, 56]. In order to reduce the performance loss, some designs use a three-dimensional (3D) coil that connects the primary coil and the secondary coils using an additional annular surface. The additional surface allows the wire paths to link the inner and outer cylindrical surfaces and provide extra contribution to the magnetic field, thus improving the coil performance [58-60].

Some split gradient coils connect the primary and secondary coils at the ends further from the ROI to reduce the eddy currents induced by the radial connection [61, 62]. To further improve coil performance, some split gradient coils are designed to add additional surface area close to the central gap (shown as Figure 2.11). The comparison result of the split gradient coils and conventional coils shows that splitting the gradient coils does not have significant influence on

the longitudinal coils, as the *z*-coil naturally has a low current density close to the central area (shown as Figure 2.10c) [56]. On the contrary, the performance of the transverse coils are significantly affected by the split configuration and the performance of the gradient coils tends to decrease with increments of the gap size [62]. Moreover, the eddy currents produced by the split gradient coils are amplified by the split configuration [62]. Therefore, the split gradient coils need to be designed carefully to meet performance requirements and the eddy currents induced by the split coils need to be investigated and mitigated.

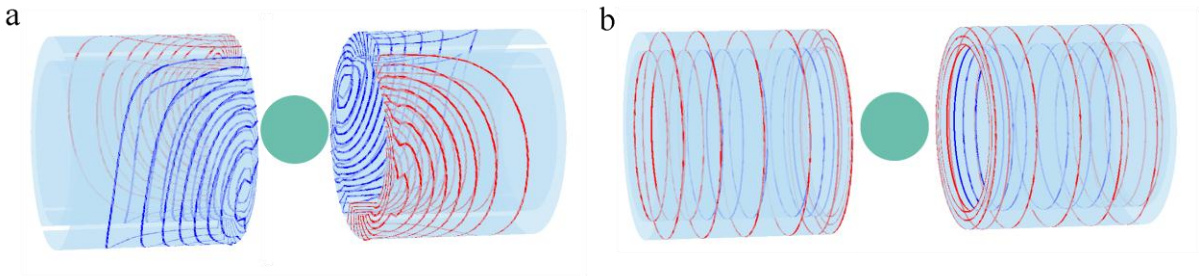

Figure 2.11 Split gradient coil, (a) *x*-coil, (b) *z*-coil.

2.4.3 Insert gradient coils

There are many MRI applications focusing on specific anatomical regions of interest to improve gradient system performance. In modern MRI, diffusion weighted EPI and other advanced imaging approaches require rapid switching of the gradient coils [63]; however, whole-body gradient coils cannot switch fast enough for diffusion encoding because of the limitations in slew rate and maximum gradient strength to avoid PNS [2, 9, 64, 65].

One approach to improve performance and gradient strength as well as to solve PNS issues is to use local gradient coils, as in smaller gradient coils, coil wires are placed closer to the ROI can increase coil performance [4, 66]. Local gradient coils do not need high-voltage amplifiers as do whole-body gradient systems at high gradient strength and fast switching speed. Local gradient coils generate a smaller magnetic flux, so they can switch faster than whole-body gradient coils without the onset of PNS. Therefore, the insert gradient coils can be used for high-performance diffusion imaging over a specified organ such as a brain, breast, knee and so on.

The most common gradient insert system is local head only or head and neck gradient coils. Head gradient coils have demonstrated their fast switching speed and high performance [67-69]. Because of the utility of the echo-planar and diffusion imaging in the brain, some commercial head gradient coil inserts have been implemented in whole-body MRI scanners and some head only gradient coils have been built specifically for brain imaging [70-72].

Head gradient coils are usually built as asymmetric coils due to the anatomical constraints imposed by the human head and shoulders and also the MRI scanner bore. This asymmetric configuration reduces coil performance. Therefore, to keep the field uniformity in the ROU, the ROU was designed to be relatively small in some early designs [5, 10, 69, 73]. In [74], a coil with a 26 cm ROU was designed for whole head coverage in a head only scanner, the inner bore of the head only gradient coils was designed to be large to maximise the shoulder insertion length. In spite of this, the gradient coil inserts still have their advantages because their integration with the resonator module and magnet reduces the upfront cost of the system. However, the gradient coil inserts need to be designed carefully to meet the stringent requirements for coil performance and the anthropometric data of the shoulders and head [75].

2.4.4 Coil performance

The gradient coil design poses a complex electromagnetic inverse problem. During the design process, several important aspects must be considered such as the linear gradient field (as described in Section 2.2.1), low stored magnetic energy, minimal torque/force, low resistance, and minimal inductive interaction with conductive surrounding structures [76, 77]. Low magnetic energy is required in order to quickly switch coils on and off to obtain images in a short period of time. Lower power loss and high dissipation are required for fast current sequences such as EPI [78], therefore, coils with low resistance are needed in order to exploit the duty cycle. These parameters are also factors used to evaluate the quality of the gradient coils. The performance of a gradient coil can be evaluated by looking at the following aspects:

Field error: ideally, the gradient field produced by the gradient coil should be linear in the ROU, otherwise, the excited nuclei may not belong to the selected slice, resulting in image distortion or even complete organs appearing in the wrong position. Thus, it is necessary to assess the accuracy of the gradient field. One of the most popular parameters used to do this is gradient field error, which is defined as [79]:

$$Field_{error} = \frac{\left|B_z(\mathrm{r}) - B_z^t(\mathrm{r})\right|}{\max(|B_z^t|)} \times 100 \tag{2.6}$$

where $B_z(\mathrm{r})$ is the gradient field produced at the target points in an ROU and $B_z^t(\mathrm{r})$ is the target field at the same point, and $\max(|B_z^t|)$ is the maximum value of $B_z^t(r)$ in the ROU.

Stray fields: The gradient coils generate magnetic fields inside and outside of the coil, and the external field produces eddy currents in the surrounding conductors, which affects the expected field produced by the coil. Therefore, the stray field must be as small as possible to protect gradient linearity and reduce eddy currents.

Field leakage ratio or shielding ratio: In the defined diameter spherical volume (DSV), a secondary magnetic field is created by the eddy currents in the surrounding conductors. To evaluate the secondary magnetic field, a leakage field ratio is defined as the ratio of the maximum absolute *z*-component of the secondary magnetic field and the field generated by the energised gradient coil.

$$\lambda_{leakratio} = \frac{\max(|Bz_{eddy}|)}{\max(|Bz_{coil}|)} \times 100 \tag{2.7}$$

Field linearity: To further evaluate the gradient linearity of the secondary magnetic field, the linear regression is used to fit the secondary magnetic field to a linear model, where the gradient offset and r^2 reflect the linearity of the field. r^2 is the coefficient of determination and the closer r^2 is to the value 1, the better the model can predict the data.

Inductance and resistance: The switching speed of the gradient coils is related to the coil inductance and to reduce the switching speed, the coil inductance should be as small as possible [80]. Because the relaxation time is the time ($\tau = \frac{L}{R}$ where L is inductance and R is resistance) it takes for the current to rise to 63% of its full value. Therefore, a small inductance can reduce the rise time, while at the same time, the resistance must be kept small to limit power dissipation in the coil.

Figure of merit (FoM): FoM is another useful performance parameter used to measure the quality of the coil [81, 82] and is defined as:

$$FoM = \frac{\eta^2}{L} \tag{2.8}$$

Where η is coil efficiency, defined as the ratio of the gradient and current (the coil efficiency is sometimes referred to as coil sensitivity; a gradient coil with high efficiency produces a larger gradient by unit of current). FoM is a parameter that is dependent on the number of turns of the gradient coil. The FoM is useful because of the gradient power amplifier to supply the required voltage.

$$P = IV = \frac{G^2 L}{\eta^2 \tau} = \frac{L}{\tau} \frac{1}{FoM} \tag{2.9}$$

Where P is the power of the amplifier, G is the field gradient and τ is the rise time. P is proportional to the $\frac{1}{FoM}$, which implies that if the gradient coil is designed with a high FoM, a lower power requirement is needed for the gradient amplifier. Another often used FoM is merit of resistance (η^2/R), where the larger the η^2/R of a gradient coil, the less heat dissipates from the coil [83].

A gradient coil of high quality should have uniform gradient homogeneity, low inductance and resistance, high efficiency, low power dissipation, high FoMs and a small stray field. So, the gradient coil design process is a trade-off between these parameters.

2.4.5 Eddy currents

In previous sections, some important concerns have been discussed during the gradient coil design process, however, these parameters are not the only concerns in coil design. Another major concern is eddy currents induced in the surrounding conductors by the switching of the gradient coils. In MRI applications, due to the high electric current and fast switching speed in the gradient coils, a time-varying electrical field is induced in the conductive surrounding structures according to Faraday's Law. Therefore, eddy currents are inevitably induced in the conductors of MRI scanners including the gradient coils themselves and their surroundings. Eddy currents produce a secondary magnetic field that opposes the field produced by the gradient coils thus deteriorating the linearity and producing distortion and artefacts in the reconstructed images [84]. Moreover, eddy currents lead to energy loss, mechanical vibration

and consequent acoustic noise, and Joule power deposition in conductive parts of MRI scanners [76, 85-87]. Eddy currents may deteriorate the coil performance in terms of power loss when very fast pulse sequences such as EPI are used [88]. Due to the inductive coupling between coils and surroundings, where the surroundings could be the radiofrequency shield, magnet cryostat or other devices that are part of the MRI scanner, a possible lengthening of the coil rise time may occur. The induction of eddy currents is one of the main causes of cross-talk between the gradient coils and hybrid components in MRI scanners [89].

Several solutions have been developed to mitigate the deleterious effects of eddy currents. One solution is to employ a higher current or modulated waveform to compensate the desired current and magnetic field [90, 91], a technique known as pre-emphasis. However, eddy currents are still induced in the surrounding conductors. Passive shielding has been used to mitigate the induction of currents in the surrounding structures containing the superconductive magnet [92]. This approach places a thick copper cylinder between gradient coils and other conductors to reduce the field leaked outside of the shield [92]. However, for passive shielding to be effective it requires a very thick wall or chilled superconductor metal to dissipate the current flux through the thickness of the wall [92]. This solution is impractical and expensive. A better solution is to employ active shielding [93], whereby the gradient coils are designed as two sets of coils with a different size radius. The inner coil is usually called the primary coil and the outer one, the secondary coil or shield coil [94]. The primary coil mainly produces the desired gradient field while the secondary coil is employed to cancel out the field leaked by the primary coil outside of the shielding (see Figure 2.10 and Figure 2.11).

Although active shielding is a widely used and relatively successful solution, eddy currents induced in the gradient coils and the surroundings still persist as a problem to overcome in the new era of highly demanding MRI experiments [95]. Rapid pulse sequences usually produce an accumulation of eddy currents in surrounding conductors while increasing possible drift in the B_0 central frequency due to the additional heat generated by the eddy currents in the gradient coils [95]. Therefore, understanding and mitigating the undesired effects of the eddy currents in MRI is of paramount importance for MRI scanners.

Several methods have been proposed to understand and mitigate eddy current effects induced by gradient coils. Finite element (FEM) and finite difference time domain (FDTD) methods

have been developed to calculate eddy currents at the cost of massive computer calculations and inaccurate handling of complex boundary conditions [63, 96]. The boundary element method (BEM) discretises active parts only while avoiding simulating the air [97]. The network methods based on a semi-analytical solution of the diffusion equation of the eddy currents in thick cylinders and the multi-layer integral method (MIM) have been employed to simulate eddy current phenomena in irregular geometries induced by gradient coils of arbitrary geometry [77, 98]. Based on the MIM described in Chapter 3, the work in chapter 5 to chapter 7 of this thesis studies the skin and proximity effects in the coil tracks and the coupling interactions between the gradient coils.

3. Electromagnetic design and modelling methods

In this chapter, the electromagnetic methodologies used in the thesis will be described. The gradient coil design method used to design the head coils, and conventional and split coils will be presented in Section 3.1. The designed coils will be analysed and evaluated using the method described in Section 3.2.

3.1 Coil design method

3.1.1 Physical problem

The equivalent magnetisation current (EMC) method is used to design the head coils in Chapter 4, and conventional coil and split actively shielded gradient coils in Chapter 5 to Chapter 7 [99]. In the EMC coil design process, the arbitrary geometry of the thin volume is discretised to triangles [66, 99]; it assumes that the current flows through a thin volume Ω with a thickness of *h* and a surface of *S*, as shown in Figure 3.1.

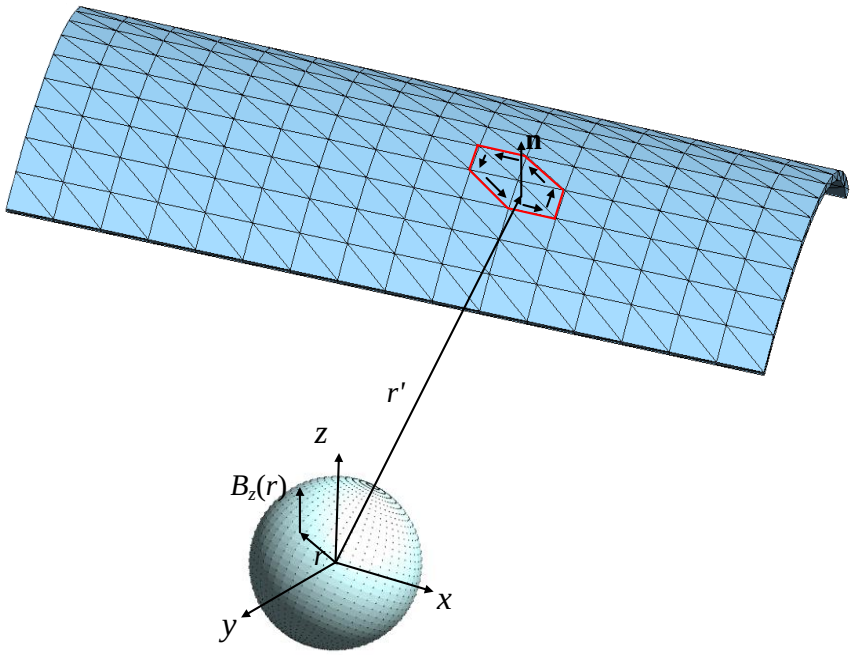

Figure 3.1 Illustration of the geometry model.

The purpose of the gradient coil design is to find the optimal current distribution to guarantee a uniform gradient field in the ROI. Moreover, the magnetic energy needs to be low, which implies a minimisation of the total inductance of the coil as described in Section 2.4.4. In addition, the average power loss and the torque need be minimised as well. Therefore, the cost function Φ can be expressed as:

$$\Phi = \sum_j W(\mathbf{r}_j)[\mathrm{B_z}(\mathbf{r}_j)\text{-}\mathrm{B_z^t}(\mathbf{r}_j)]^2 + \alpha W + \beta P - \sum_k (\lambda_{kx}\mathrm{T}_{kx} + \lambda_{ky}\mathrm{T}_{ky} + \lambda_{kz}\mathrm{T}_{kz}) \tag{3.1}$$

3.1.2 Discretising the problem

On surface *S*, assuming magnetic quasi-static approximation, the current density is solenoidal (div-free), making the use of a vector potential possible:

$$\nabla \cdot \mathbf{J} = 0 \Rightarrow \mathbf{J} = \nabla \times \mathbf{T} \tag{3.2}$$

Where ***T*** is the electric vector potential. The study is restricted to the case when *S* can be approximated by 2D curved surfaces, i.e. the current density lies on these surfaces. In this case the vector potential can be represented as the scalar stream function ψ:

$$\mathbf{T} = \mathbf{n}\psi \tag{3.3}$$

Where ***n*** is the unit normal to the current density plane Figure 3.2. When *S* is discretised by planar patches (triangles or quadrilaterals shown as in Figure 3.1), the stream function can be expanded by nodal basis functions λ_k:

$$\psi = \sum_k \lambda_k \psi_k \tag{3.4}$$

where ψ_k are the values of the stream function at the mesh nodes. The current density in the generic triangle can be interpolated by means of Eq.(3.5):

$$\mathbf{J}^{\alpha} = \nabla \times (\mathbf{n}\psi) = \nabla \times (\mathbf{n}^a \sum_k \lambda_k \psi_k) = \sum_k \psi_k \nabla \times (\lambda_k \mathbf{n}^{\alpha}) = \sum_k \psi_k \mathbf{f}_k \tag{3.5}$$

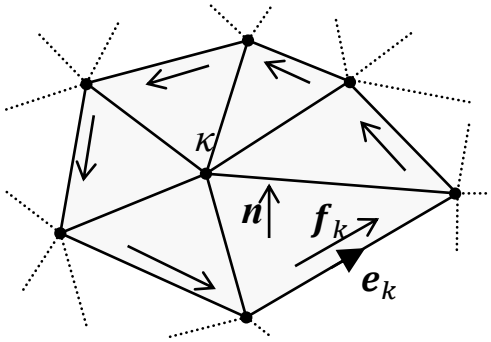

Figure 3.2 Node *k* and corresponding nodal function λ_k and edge vector $\mathbf{e}_k$. Note that the direction of the edge is associated with the orthogonal unit normal $\boldsymbol{n}$ according to the right-hand rule.

In the case of triangular discretisation (see [100]):

$$\mathbf{f}_\mathbf{k} = \nabla \times (\lambda_\mathrm{k} \mathbf{n}^a) = \frac{\mathbf{e}_k}{2\mathbf{A}^a} \tag{3.6}$$

$\mathbf{e}_k$ is associated with the orthogonal unit normal **n** according to the right-hand rule and $\mathbf{A}^a$ is the triangle area.

3.1.3 Computational issues

A magnetic field **B** is calculated as the curl of the magnetic vector potential **A**:

$$\mathbf{B} = \nabla \times \mathbf{A} \tag{3.7}$$

According to Ampere's Law:

$$\nabla \times \mathbf{B} = \mu_0 \mathbf{J} \tag{3.8}$$

where μ_0 is the permeability of the free space. Substituting Eq.(3.7) with Eq.(3.8), it becomes:

$$\nabla \times \nabla \times \mathbf{A} = \mu_0 \mathbf{J} \tag{3.9}$$

Using the identity:

$$\nabla \times \nabla \times \mathbf{A} = \nabla^2 \mathbf{A} - \nabla(\nabla \cdot \mathbf{A}) \tag{3.10}$$

Because of the Coulomb's gauge, $\nabla \cdot \mathbf{A} = 0$ and combing Eq.(3.9) and Eq.(3.10), it becomes:

$$\nabla^2 \mathbf{A} = \mu_0 \mathbf{J} \tag{3.11}$$

The solution of Eq.(3.11) is:

$$\mathbf{A}(\mathbf{r}) = \frac{\mu_0}{4\pi} \int_{\Omega} \frac{\mathbf{J}(\mathbf{r}')}{|\mathbf{r} - \mathbf{r}'|} \mathbf{d}\Omega \tag{3.12}$$

The magnetic vector potential in Eq.(3.12) can be expressed by the discretised surface current density in Eq.(3.5):

$$\mathbf{A}(\mathbf{r}) \approx \frac{\mu_0}{4\pi} \sum_i \psi_i \int_{S'} \left(\frac{\mathbf{f}_i(\mathbf{r}')}{|\mathbf{r} - \mathbf{r}'|} \right) \mathrm{dS}' \tag{3.13}$$

From Eq.(3.7) and (3.13), the magnetic flux density generated by the current-carrying surface S can be calculated from the stream function vector ψ:

$$\begin{aligned} \mathbf{B}(\mathbf{r}) &= \nabla \times \mathbf{A}(\mathbf{r}) \\ &= \frac{\mu_0}{4\pi} \sum_i \psi_i \int_{S'} \nabla \left(\frac{1}{|\mathbf{r} - \mathbf{r}'|} \right) \times \mathbf{f}_i(\mathbf{r}') \mathrm{dS}' \end{aligned} \tag{3.14}$$

If only the z-component is considered, Eq.(3.14) becomes:

$$\begin{aligned} B_z(\mathbf{r}) &= \frac{\mu_0}{4\pi} \sum_i \psi_i \int_{S'} \left(\frac{-f_{ny}(\mathbf{r}')(x - x') + f_{nx}(\mathbf{r}')(y - y')}{|\mathbf{r} - \mathbf{r}'|^3} \right) \mathrm{dS}' \\ &= \sum_i \psi_i c_n(\mathbf{r}) \end{aligned} \tag{3.15}$$

Where

$$c_n(\mathbf{r}) = \frac{\mu_0}{4\pi} \int_{S'} \left(\frac{-f_{ny}(\mathbf{r}')(x - x') + f_{nx}(\mathbf{r}')(y - y')}{|\mathbf{r} - \mathbf{r}'|^3} \right) \mathrm{dS}' \tag{3.16}$$

The stored magnetic energy is defined as:

$$\begin{aligned} W &= \frac{\mu_0}{8\pi} \int_S \int_{S'} \left(\frac{\mathbf{J}(\mathbf{r}) \cdot \mathbf{J}(\mathbf{r}')}{|\mathbf{r} - \mathbf{r}'|} \right) \mathrm{dS}' \mathrm{dS} \\ &\approx \frac{\mu_0}{8\pi} \sum_j \sum_i \psi_j \psi_i \mathbf{f}_j \cdot \mathbf{f}_i \int_S \int_{S'} \left(\frac{1}{|\mathbf{r} - \mathbf{r}'|} \right) \mathrm{dS}' \mathrm{dS} \end{aligned} \tag{3.17}$$

The inductive coupling terms are:

$$L_{ij} = \frac{\mu_0}{4\pi}\mathbf{f}_j \cdot \mathbf{f}_i \int_S \int_{S'} \left(\frac{1}{|\mathbf{r} - \mathbf{r}'|}\right) \mathrm{dS}' \, \mathrm{dS} \tag{3.18}$$

Re-expressing Eq.(3.17) using the inductance calculated in Eq.(3.18) yields (Eq.18 in [101]):

$$W \approx \frac{1}{2}\sum_j \sum_i \psi_i \psi_j L_{ij} \tag{3.19}$$

The power dissipated in the coil domain P can be expressed as:

$$\begin{aligned} P &= \frac{\rho}{2t}\int_S |\mathbf{J}(\mathbf{r}')|^2 \, \mathrm{dS} \\ &= \frac{\rho}{2t}\sum_j \sum_i \psi_j \cdot \psi_i \int_S \mathbf{f}_j \cdot \mathbf{f}_i dS \end{aligned} \tag{3.20}$$

Where t is the thickness of the conducting layer and ρ is the resistivity of the conducting material. If the nodes share no triangles then $R_{ij} = 0$, but if two nodes share the same triangle, the resistive coupling is defined as:

$$R_{ij} = \frac{\rho}{t}\int_S \mathbf{f}_j \cdot \mathbf{f}_i dS \tag{3.21}$$

Re-expressing Eq.(3.20) using the resistance in Eq.(3.21), the electric power loss can be:

$$P \approx \frac{1}{2}\sum_j \sum_i \psi_i \psi_j R_{ij} \tag{3.22}$$

The torque because of the external magnetic field $\mathbf{B_0}(\mathbf{r}')$ is given by:

$$T = \int_S \mathbf{r} \times \mathbf{J}(\mathbf{r}') \times \mathbf{B_0}(\mathbf{r}') \mathrm{dS} \tag{3.23}$$

Since $\mathbf{B}_0(\mathbf{r}')$ is parallel to the z-axis, then Eq.(3.23) can be discomposed into equations:

$$
\begin{aligned}
T_x &= B_0 \int_S J_x z dS \approx B_0 \sum_i \psi_i \int_S f_{nx} z dS \\
T_y &= B_0 \int_S J_y z dS \approx B_0 \sum_i \psi_i \int_S f_{ny} z dS \\
T_z &= -B_0 \int_S \left(J_x x + J_y y \right) dS \approx -B_0 \sum_i \psi_i \int_S (f_{nx} x + f_{ny} y) dS
\end{aligned}
\tag{3.24}
$$

Thus, from Eq.(3.15), Eq.(3.19), Eq.(3.22), Eq.(3.24), each component in the object function Eq.(3.1): the gradient field $\mathrm{B}_z(\mathbf{r}_j)$, inductance *L*, resistance *R*, stored energy *W*, power loss *P*, torque T_x, T_y and T_z can be expressed by the steam function ψ, which is the only unknown value and can be solved by quadratic equations [79].

$$
\begin{aligned}
\Phi &= \sum_j W(\mathbf{r}_j)[\mathrm{B}_z(\mathbf{r}_j) - \mathrm{B}_z^t(\mathbf{r}_j)]^2 \\
&+ \frac{\alpha}{2} \sum_j \sum_i \psi_i \psi_j L_{ij} \\
&+ \frac{\beta}{2} \sum_j \sum_i \psi_i \psi_j R_{ij} \\
&- \sum_k (\lambda_{kx} B_0 \sum_i \psi_i \int_S f_{nx} z dS + \lambda_{ky} \mathrm{T}_{ky} + \lambda_{kz} \mathrm{T}_{kz})
\end{aligned}
\tag{3.25}
$$

3.2 Multi-layer Integral Method

3.2.1 Physical problem

The multi-layer integral method (MIM) was used for eddy current simulations and to analyse inductive interaction between the gradient coil and surrounding metallic conductors [77]. The unbounded 3D domain is subdivided into three complementary regions:

- the source domain Ω_s with imposed currents i_s, e.g. filamentary coils with known currents;
- the domain where eddy currents are induced Ω with finite conductivity σ, including coils with unknown current distribution, e.g. tracks;
- the nonconductive ($\sigma = 0\ \mathrm{Sm}^{-1}$) domain Ω_0 , rigorously accounted by Green's formula in the integral formulation.

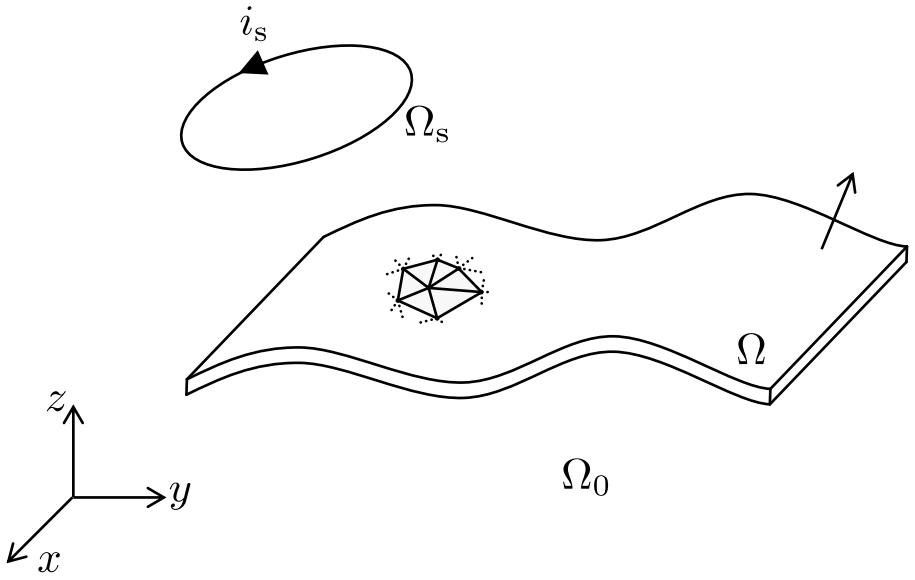

Figure 3.3 Domain division: sources Ω_s, eddy currents Ω and nonconductive region Ω_0.

The purpose of MIM was to calculate the current density distribution in Ω_s and the eddy current profile in the surrounding structure Ω.

3.2.2 Computational issues

From Maxwell's equations, the electric field in the frequency domain can be expressed as:

$$\mathbf{E} = -jw\mathbf{A} - \nabla\varphi \tag{3.26}$$

where φ is the electric scalar potential and w is the angular frequency. The non-retarded magnetic vector potential is expressed in terms of Green's function:

$$\mathbf{A}(\mathbf{r}) = \frac{\mu_0}{4\pi}\int_{\Omega'}\frac{\mathbf{J}(\mathbf{r}')}{|\mathbf{r}-\mathbf{r}'|}\mathrm{d}\Omega + \mathbf{A}_s(\mathbf{r}) \tag{3.27}$$

where $\mathbf{r}'$ is the vector pointing to the source point, $\mathbf{r}$ is the vector pointing to the field point and $\mathbf{A_s(r)}$ is the magnetic vector potential due to the known sources in Ω_s.

With Eq.(3.27) and the constitutive equation $\mathbf{E} = \rho\mathbf{J}$, Eq.(3.26) becomes:

$$\rho\mathbf{J}(\mathbf{r}) + jw\frac{u_0}{4\pi}\int_{\Omega'}\frac{\mathbf{J}(\mathbf{r}')}{|\mathbf{r}-\mathbf{r}'|}\mathrm{d}\Omega + jw\mathbf{As} + \nabla\varphi = 0 \tag{3.28}$$

Now the Galerkin scheme limited to the triangle α is applied to Eq.(3.28), using Eq.(3.6) as weights. For each node of the mesh:

$$\int_{\Omega_\alpha} \mathbf{f}_j \cdot \rho_\alpha \mathbf{J}_\alpha(\mathbf{r}) \mathrm{d}\Omega + jw\frac{u_0}{4\pi} \int_{\Omega_\alpha} \mathbf{f}_j \cdot \int_{\Omega'} \frac{\mathbf{J}(\mathbf{r})}{|\mathbf{r}-\mathbf{r}'|} \mathrm{d}\Omega \mathrm{d}\Omega + jw \int_{\Omega_\alpha} \mathbf{f}_j \cdot \mathbf{A}\mathbf{s} \mathrm{d}\Omega + \int_{\Omega_\alpha} \mathbf{f}_j \cdot \nabla\varphi \mathrm{d}\Omega = 0 \tag{3.29}$$

The last term of including $\nabla\varphi$ vanishes from Eq.2 in [102]. When $\mathbf{J}_\alpha$ is expanded by means of Eq.(3.6) and the resistance coupling between the adjacent nodes in Eq.(3.21), Eq.(3.29) is:

$$\begin{aligned} \int_{\Omega_\alpha} \rho_\alpha \mathbf{f}_j \cdot \sum_k \psi_k \mathbf{f}_k \mathrm{d}\Omega &= \sum_k \psi_k \int_{\Omega_\alpha} \rho_\alpha \mathbf{f}_j \cdot \mathbf{f}_k \mathrm{d}\Omega \\ &= \sum_k \psi_k \delta_\alpha \int_{\Sigma_\alpha} \rho_\alpha \mathbf{f}_j \cdot \mathbf{f}_k \mathrm{d}\Sigma \\ &= \sum_k \psi_k R_{jk} \end{aligned} \tag{3.30}$$

Both *j* and *k* refer to the nodes of the triangle *α*, giving rise to a local coupling (limited to triangles sharing the same common node) of the resistive terms.

In the second integral of Eq.(3.29), the coupling inductance is calculated as Eq.(3.18), and the integration over the conductive domain is split into the elementary patches Ω_β of the mesh $\Omega = \bigcup \Omega_\beta$:

$$\begin{aligned} jw\frac{\mu_0}{4\pi} \int_{\Omega_\alpha} \mathbf{f}_j \cdot \int_{\Omega'} \frac{\mathbf{J}(\mathbf{r}')}{|\mathbf{r}-\mathbf{r}'|} \mathrm{d}\Omega \mathrm{d}\Omega &= jw\frac{\mu_0}{4\pi} \int_{\Omega_\alpha} \mathbf{f}_j \cdot \sum_\beta \int_{\Omega'_\beta} \frac{\mathbf{J}_\beta(\mathbf{r}')}{|\mathbf{r}-\mathbf{r}'|} \mathrm{d}\Omega \mathrm{d}\Omega \\ &= jw\frac{\mu_0}{4\pi} \int_{\Omega_\alpha} \mathbf{f}_j \cdot \sum_\beta \int_{\Omega'_\beta} \frac{1}{|\mathbf{r}-\mathbf{r}'|} \sum_i \psi_i \mathbf{f}_j \mathrm{d}\Omega \mathrm{d}\Omega \\ &= jw\frac{\mu_0}{4\pi} \sum_\beta \sum_i \psi_i \mathbf{f}_j \cdot \mathbf{f}_i \int_{\Omega_\alpha} \int_{\Omega'_\beta} \frac{1}{|\mathbf{r}-\mathbf{r}'|} \mathrm{d}\Omega \mathrm{d}\Omega \\ &= jw\frac{\mu_0}{4\pi} \sum_\beta \sum_i \psi_i \delta_\alpha \delta_\beta \mathbf{f}_j \cdot \mathbf{f}_i \int_{\Sigma_\alpha} \int_{\Sigma'_\beta} \frac{1}{|\mathbf{r}-\mathbf{r}'|} \mathrm{d}\Sigma \mathrm{d}\Sigma \\ &= jw\frac{\mu_0}{4\pi} \sum_\beta \sum_i \psi_i L_{ij} \end{aligned} \tag{3.31}$$

Finally, the source term in Eq.(3.29) is:

$$jw\int_{\Omega_\alpha}\mathbf{f}_j\cdot\mathbf{As}\mathrm{d}\Omega = jw\int_{\Sigma_\alpha}\mathbf{f}_j\cdot\mathbf{As}\mathrm{d}\Sigma=jwa_{s,j} \tag{3.32}$$

The Galerkin equation Eq.(3.29) is referred to the *j*th node of triangle α. By looping over the mesh elements, the same node can appear many times. In this case, the corresponding terms are summed up, giving rise to a global $N\times N$ system, where N is the number of mesh nodes:

$$(\mathbf{R}+jw\mathbf{L}) = jw\boldsymbol{\alpha}_\mathbf{s} \tag{3.33}$$

The integral in Eq.(3.21) is singular but can be effectively and efficiently calculated using analytical formulas [103, 104]. The double integral in Eq.(3.18) is calculated by combining analytical and numerical quadrature [105], even though analytical formulas exist for the double self-integral [106, 107]. A numerical quadrature is used to solve Eq.(3.32) because of the unknown spatial distribution of the magnetic vector potential of the sources **As**.

3.2.3 Boundary conditions

The stream function is not univocally defined. In a general 3D domain, from Eq.(3.2) a gradient of an arbitrary scalar function can be added to the electric vector potential **T** without affecting the physical quantity **J**. With the layer approximation and the use of the stream function ψ, this condition is relaxed and the stream function is unaffected if a constant is added. In order to guarantee the uniqueness of the solution (mandatory when using direct solvers, optional if iterative ones) the stream function must be specified in one arbitrary node for each independent structure. To correctly apply the boundary conditions, it is important to first understand the physical meaning of the stream function ψ in the layered formulation: the difference between stream functions between two points is the total current through every line connecting those two points.

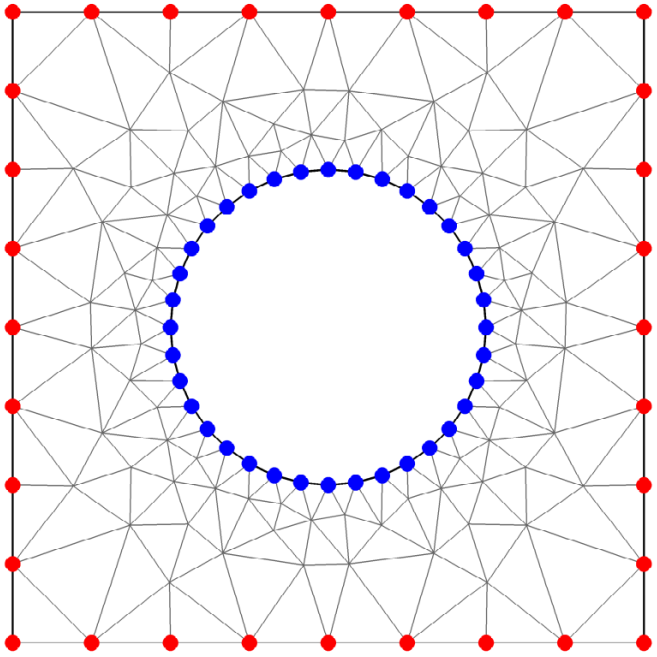

Figure 3.4: Example of domain Ω with distinction between the inner and outer boundaries. One is arbitrarily set to zero, the other is unknown.

To enforce the fact that the current must lie inside the domain Ω, nodes belonging to the same boundary are characterised by the same value of the stream function. In this way, the current cannot cross the boundary. In general, the value of the boundary stream function is unknown. Different boundaries of the same structure are characterised by different values of the stream function (see Figure 3.4), otherwise the total net current will be set to zero. It is easy (but not mandatory) to set the stream function of one boundary to zero, in order to simultaneously fulfil the uniqueness requirement.

When dealing with structures with known total current, e.g. the tracks of Figure 3.5, but unknown current distribution through the structure width, the boundary values must be carefully set in order to obtain the desired behaviour. In this case, one boundary is set to zero and the other to the total current, taking care of the current orientation.

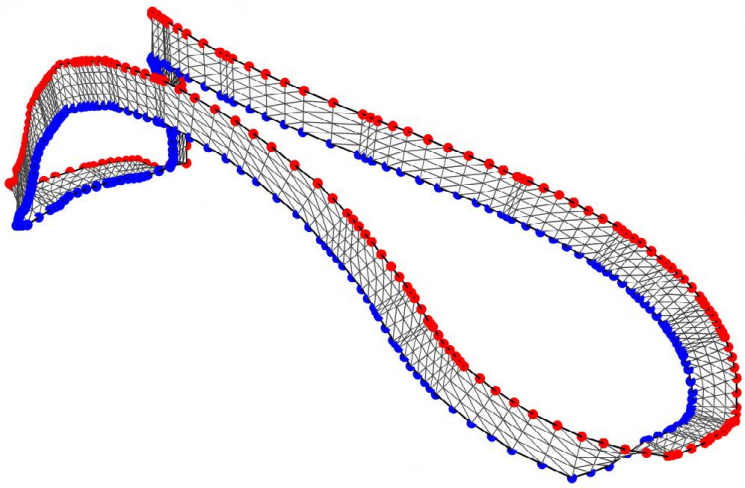

Figure 3.5: Example of a complex track and boundary identification. Blue dots represent nodes where the stream function is set to zero, whereas at red nodes the stream function is set equal to the total current. Note that the only requirement is the difference between the stream function values.

The MIM described in this section has advantages in calculating the induced eddy currents in arbitrary thin volumes [108]. This method was extended to calculate the current distribution in the gradient coils themselves in Chapter 5, the eddy current profile in surrounding gradient coils in Chapter 6 and the current density distribution in the coils after slitting the coil tracks by carefully setting the boundary conditions in Chapter 7.

4. An improved asymmetric head gradient coil design

As described in Section 2.4.2, head gradient coil inserts improve gradient strength and performance and support fast switching, therefore, enabling rapid brain imaging. However, the head gradient coils are usually designed to be of asymmetric geometry because of the constraints of human shoulders and head, and this design degrades the coil performance. In this chapter, a novel coil model will be proposed to improve the coil performance for high-resolution imaging.

This chapter is largely based on the journal article "An improved asymmetric gradient coil design for high-resolution MRI head imaging" under review by the journal *Physics in Medicine and Biology*. The research presented in this chapter aims to improve the performance of the asymmetric head gradient coils. Editing has been mainly carried out in the introduction for the best coherence with other chapters.

Publication details

Fangfang Tang, Feng Liu, Fabio Freschi, Yu Li, Maurizio Repetto, Luca Giaccone, Yaohui Wang, Stuart Crozier, An improved asymmetric gradient coil design for high-resolution MRI head imaging, *Physics in Medicine and Biology*, 2016 (accepeted).

Manuscript revision history

Submitted to *Physics in Medicine and Biology*	9 June 2016
Interim Decision (major revision)	29 July 2016
Revision submission	17 August 2016
Interim Decision (minor revision)	16 September 2016
Revision submission	28 September 2016
Accepted	3 November 2016

Author contributions

Fangfang Tang	Numerical modelling, code implementation, analysis and interpretation, manuscript preparation
Feng Liu	Analysis and interpretation, manuscript reviews
Fabio Freschi	Analysis and interpretation, manuscript reviews
Yu Li	Manuscript reviews
Maurizio Repetto	Manuscript reviews
Luca Giaccone	Manuscript reviews
Yaohui Wang	Manuscript reviews
Stuart Crozier	Manuscript reviews

4.1 Introduction

In modern magnetic resonance imaging (MRI), high-strength and high performance gradient coils are desired to improve image quality and imaging speed for diffusion-weighted imaging, echo planar imaging (EPI), and other advanced imaging protocols [8, 109, 110]. Gradient coils with a high gradient strength can improve the diffusion contrast in diffusion imaging, shorten the echo time and enable high resolution EPI images [111, 112]. The gradient coils should have a minimum inductance for a given target gradient strength to ensure rapid switching capability [81] .

One approach for improving the gradient coil performance is to use local gradient coils. Smaller gradient coils can generate a high gradient strength, meanwhile decreasing the inductance and improving switching speeds. The voltage applied can be smaller to produce the desired gradient strength than the whole-body coil, because the whole-body coil requires more powerful and expensive gradient amplifiers [113]. In addition, local gradient coils dissipate less power and minimize the stored energy.

A number of local gradient coils have been designed for head imaging. For example, Alsop et al. proposed a torque-balanced asymmetric head coil using a modified singular value decomposition algorithm [5]. Chronik et al. developed a three-axis edge coil for head and neck imaging using an analytic method [10]. Tomasi et al. considered an asymmetric coil that matched the region-of-uniformity (ROU) and homogeneous-gradient-volume (HGV) using a fast simulated annealing approach [114]. Handler et al. devised a new insertable head gradient coil in combination with whole-body coils using novel cooling methods [115]. Crozier et. al. designed an asymmetric gradient set for a compact superconducting MRI magnet for head and neck imaging [6]. Jean-Baptiste developed a force and torque balanced gradient coil to constrain individual harmonics of the field produced by the gradient coil and eddy currents in a specialty 3T head only magnet [74, 75].

Head gradient coils are usually designed to be asymmetric for the accommodation of the human head and shoulders, with the ROU being located close to one edge of the gradient coil instead of the centre[116]. However, the performance of the local gradient coils is frequently hampered by the asymmetric geometry. In addition, the head gradient coil needs to be designed with a diameter larger than 30 cm, taking into account the size of the human head and RF assembly. The length-to-diameter ratio of the coil needs be larger than 1.5 to obtain a target gradient uniformity [114]. Thus, the space available for the coil is limited and conventional designs offer compromises in field linearity, inductance and resistance and other parameters. In this paper, we provide a new design in an effort to resolve some of these engineering challenges.

In compact gradient coil designs, it is advantageous to make a connection between the primary and shielding layers near the coil ends. Improved performance has been shown for ultra-short whole-body gradient coils, where coils are connected at both the patient and service ends. Benefiting from this connected structural design, the gradient sensitivity could be improved by 10–15% [58], and save up to 50% of space compared to a conventional coil design. This reduces the localized regions of Joule heating in the coil and allows the design of coils easier to manufacture. The stored magnetic energy also could be significantly reduced, because the current directly flows off the primary to the secondary coil [59]. However, apart from the excellent electromagnetic performance, this coil design also introduces difficult engineering constraints. In a practical gradient coil layout, a certain space between the primary and secondary coils is maintained for passive shimming components and cooling pipes. A free and unhindered access to the shims and pipes is necessary. With the both-ends-connected coils, however, inserting shims is difficult owing to the wires on

the flange. Poole et al. [117] proposed designing coils with bunches of equally-spaced windings without taking up all the surfaces on the flange. This method may increase the complexity of the mechanical structure and bring challenges in the arrangement of the inlet/outlets of the coil cooling system and power cable wiring.

In this work, we proposed a novel design for an asymmetric gradient coil for head imaging [118]. Considering the above-mentioned structural constraints, the new design connected the primary and secondary coils at only the patient end, with the service end being left open. Connecting the patient end of the coil made a significant contribution to the field generation owing to the non-centred ROU and the extra current flow on the flange. This improved the performance of the asymmetric coil and sparsely-spaced wires compared to the conventional (un-connected) head coil. In this paper, the asymmetric patient end connected coils were studied and compared with the conventional designs.

4.2 Method

4.2.1 Coil design method

The gradient coil design process is to find the optimal current distribution to achieve the expected magnetic field in the ROU, at the same time improving the coil performance, such as reducing the stored energy, the power loss in the coil and the eddy currents in the surrounding. [55, 66, 119]. Here, the optimization problem can be expressed as follows:

$$\begin{aligned} &Minimize: \alpha W + \beta P \\ &Subject\ to: |B_z - B_z^t| \le \varepsilon B_z^t, |B_z^s| < \lambda |B_z^t| \end{aligned} \tag{4.1}$$

where W is the stored energy and P is the average power loss in the coil structure, respectively. α and β are the optimization weighting factors for stored energy and power loss. B_z^t is the z-component of the target magnetic field at the point within an ROU and B_z is the designed field at the corresponding target points. The error weighting factor, ε, predicts the accuracy of the designed field. The B_z^s is the secondary magnetic field generated in the ROU by the eddy currents in the secondary cold shield of the cryostat (the outmost layer in Figure 4.1), which should be smaller than the $\eta |B_z^t|$.

The stored energy W and the power loss P in Eq.1 can be calculated from the stream function ψ as in Eq.(4.2) and Eq.(4.3), where L is the inductance matrix and R is the resistance matrix.

$$W = \psi^T L \psi \tag{4.2}$$

$$P = \psi^T R \psi \tag{4.3}$$

The inductance L, resistance R, designed field B_z and the secondary field B_z^s are parameterized by the stream function values ψ. The stream function values can be obtained by solving Eq.(4.1) using the Quadratic Programming Approach [99, 120].

4.2.2 Coil models

Figure 4.1 shows a cross-sectional drawing of the head MRI scanner to study different head models. The ROU was an oblate spheroid featured with a 24×24×22 cm ROU. The gradient coils were asymmetric coils (the ROU was close to the patient end of the head gradient coils) shown in the shaded boxes in Figure 4.1. The primary and secondary *x*-coils were designed with diameters of 33.6 cm and 55.8 cm, respectively, while the *z*-coils were designed with diameters of 35.6 cm and 53.8 cm, respectively. The details of the transverse *x*-coil and longitude *z*-coil are shown in Table 4.1.

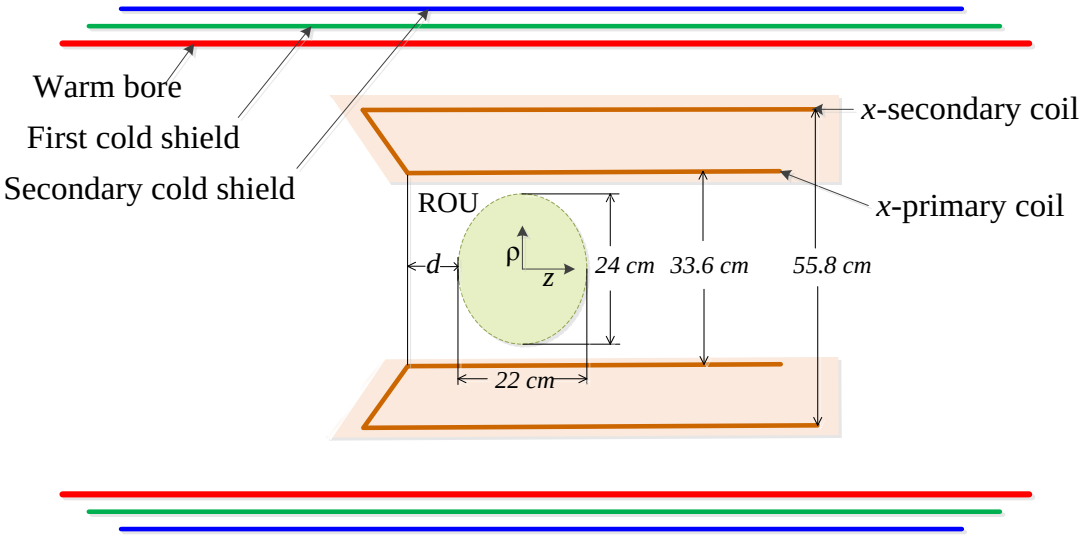

Figure 4.1 Cross-sectional scale drawing of the cryostat and gradient structures

To study the performance of the connected coil, four variants of the coils were designed and compared in this study.

(1) Separated short shield coil: the primary and shield coils were separated, $L_p = L_s$, where *Lp* and *Ls* were the length of the primary and secondary coil, respectively (Figure 4.2a).

(2) Separated long shield coil: the primary and shield coils were separated, $L_p < L_s$ (Figure 4.2b).

(3) Connected short shield coil: the primary and shield coils were connected by a radial connected flange at the end close to the ROU, $L_p = L_s$ (Figure 4.2c).

(4) Connected long shield coil: the primary and shield coils were connected, $L_p < L_s$ (Figure 4.2d).

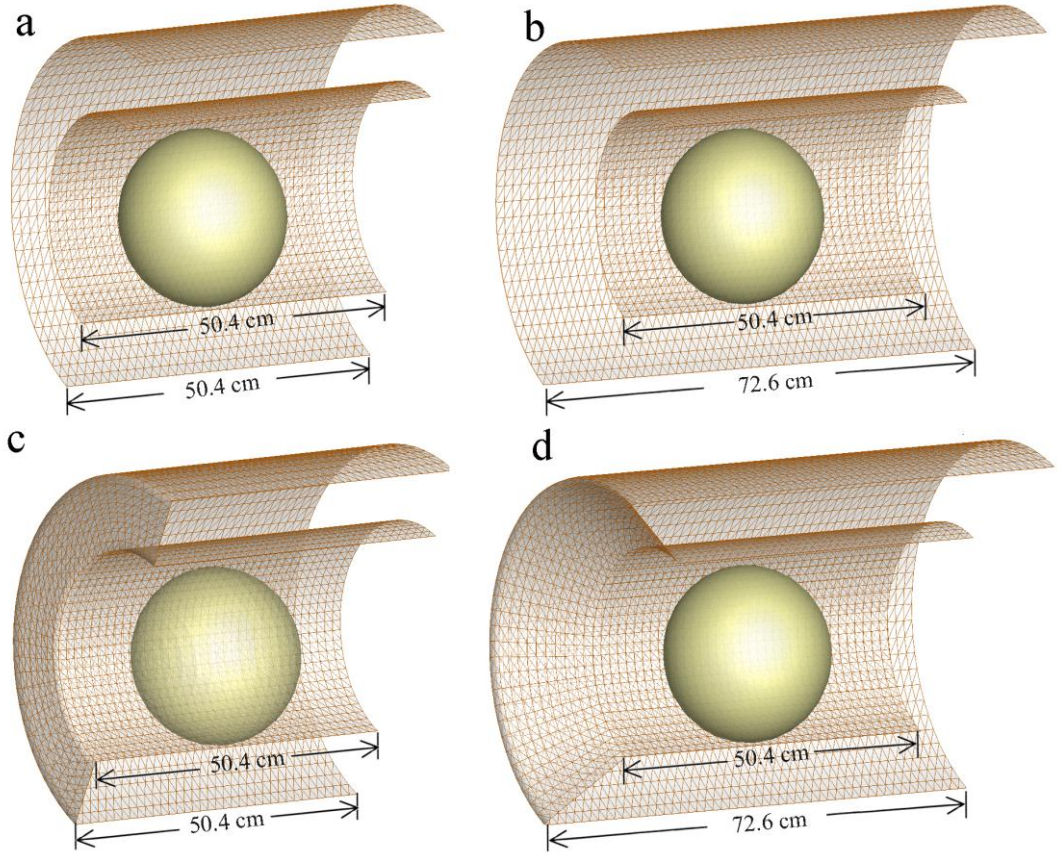

Figure 4.2. Schematic geometry of the asymmetric head coils, (a) separated short shield coil, (b) separated long shield coil, (c) connected short shield coil and, (d) connected long shield coil

To compare the four coil models and study the impacts of the distance between the ROU centre and the edge of the coil, the distance *d* (shown in Figure 4.1) between the coil edge and ROU edge varies from 0 to 10 cm. All the separated and connected head coils were designed to produce a target gradient strength of 60 mT/m. The value of ε was set to 5% and weighting factors α and β were both set as 1 for all the coils, η was set as 0.2% for the transverse coils and 1% for the longitudinal coils in the paper. The minimum gap between the

wires was constrained to be 1 mm and the track width was 3 mm for both the transverse and longitudinal coils designed with four variants of head coil structures.

The geometry of the connected shield coil was discretised with 7400 nodes and 14256 triangles. The gradient coil optimization was undertaken using Matlab 2015a, and the design can be completed in 10 minutes on a computer equipped with Intel Core i7-3770CPU and 16 G RAM.

Table 4.1 Properties of coils

	x-coil (short shield)	*x*-coil (long shield)	*z*-coil (short shield)	*z*-coil (long shield)
Lp (cm)	50.4	50.4	50.4	50.4
Ls(cm)	72.6	72.6	72.6	72.6
Diameters (cm)	33.6	33.6	35.6	35.6
Rout(cm)	55.8	55.8	53.8	53.8

4.3 Results and discussion

4.3.1 Transverse coil

Figure 4.3 shows the example coils wires of the corresponding geometry structures in Figure 4.2. It can be seen that in the connected model, the wires are wound on the connected surface.

Figure 4.4 presents the coil performance as a function of distance *d*. All the coils were designed using the same stream function contours of 30 turns. In this paper, when evaluating the coil performance and eddy currents in each coil, the conductive elements including the coil and layered cryostat shown in Figure 4.1 were all considered [108]. We compared the coil performance current, coil efficiency, figure-of-merit (FoM) and η^2/R as shown in Figure 4.4. Coil efficiency refers to the magnetic field gradient at the image centre produced by a unit current of the coil [1]. FoM is defined as η^2/L and reflects the power requirements of the driving amplifier, where η is the coil efficiency and L the inductance. η^2/R, where η is coil efficiency and R is resistance, reflects the power dissipation in the coil structure. *FoM* and η^2/R are independent of the turns of the coils.

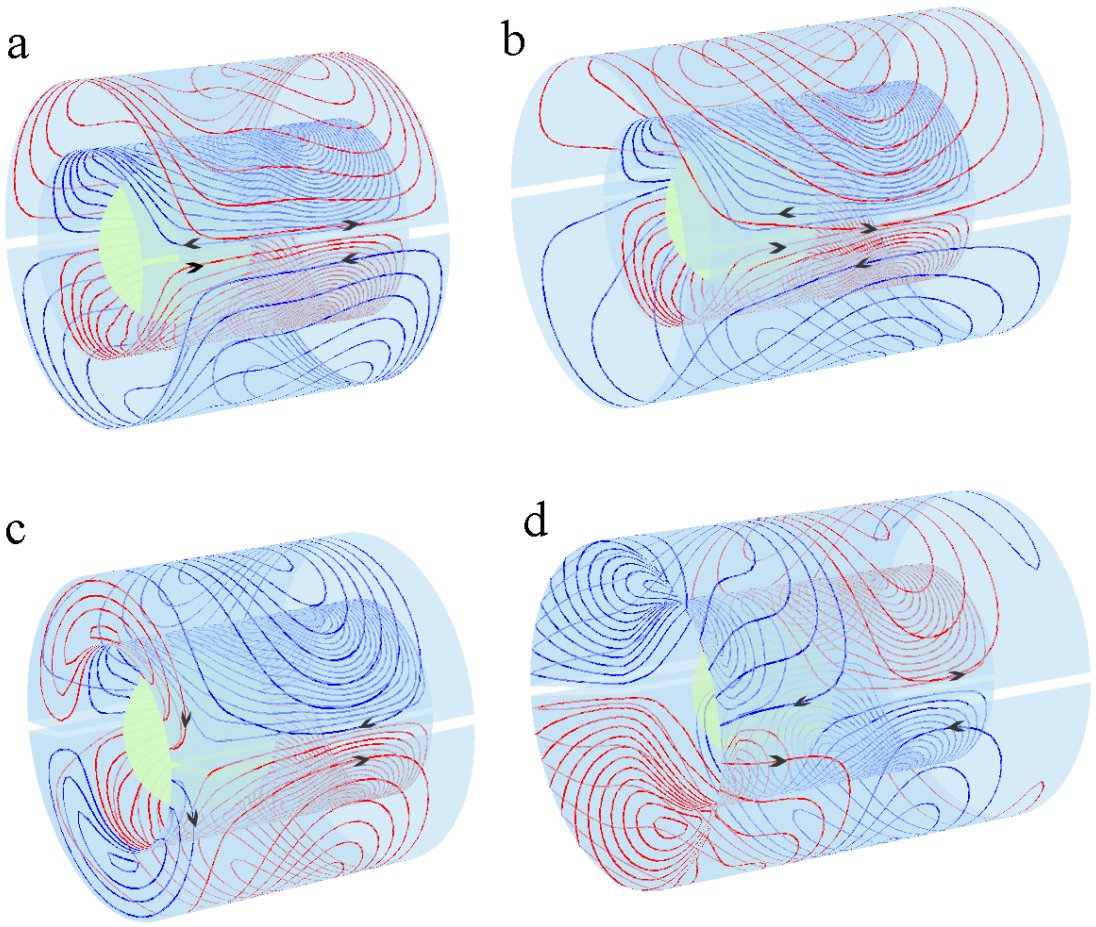

Figure 4.3. Examples of the asymmetric transverse *x*-coil designed with different coil structures, the arrows show the current direction, (a) separated short shield coil, (b) separated long shield coil, (c) connected short shield coil and, (d) connected long shield coil.

It can be seen in Figure 4.4 that the connected coils have a better performance than the separated coils. The performance of the connected coil with the long shield is the best, and the separated coil with short shield is the worst. Figure 4.4a presents the details of the driving currents; the connected coils need a lower operating current to produce the target gradient strength 60 mT/m. This is because of the additional current flow on the flanged surface in the connected structure. The connected coil with the long shield needs the lowest operating current at d = 6 cm, while the other three coils need the lowest driving current at d = 10 cm. The connected coil with the long shield is also the most efficient configuration and has the highest FoM and η^2/R; this indicates that this coil dissipates less power and needs less power supply. This is because of the extra contribution from the wires on the connected surface between the primary and secondary coils. Also, at d =

6 cm, the efficiency, FoM and η^2/R reach the peak value for the connected coil with the long shield, but the values decrease when d > 6 cm, because of the greater distance between the connected coil edges and the ROU. The performance of the connected coil with the short shield increases from d = 6 cm, while the performance of the separated coils is flat with d. To ensure a proper accommodation for the size of human head and shoulder and keeping the coil performance [5, 114], a d = 4 to 6 cm is recommended in the design of the connected coil with the long shield.

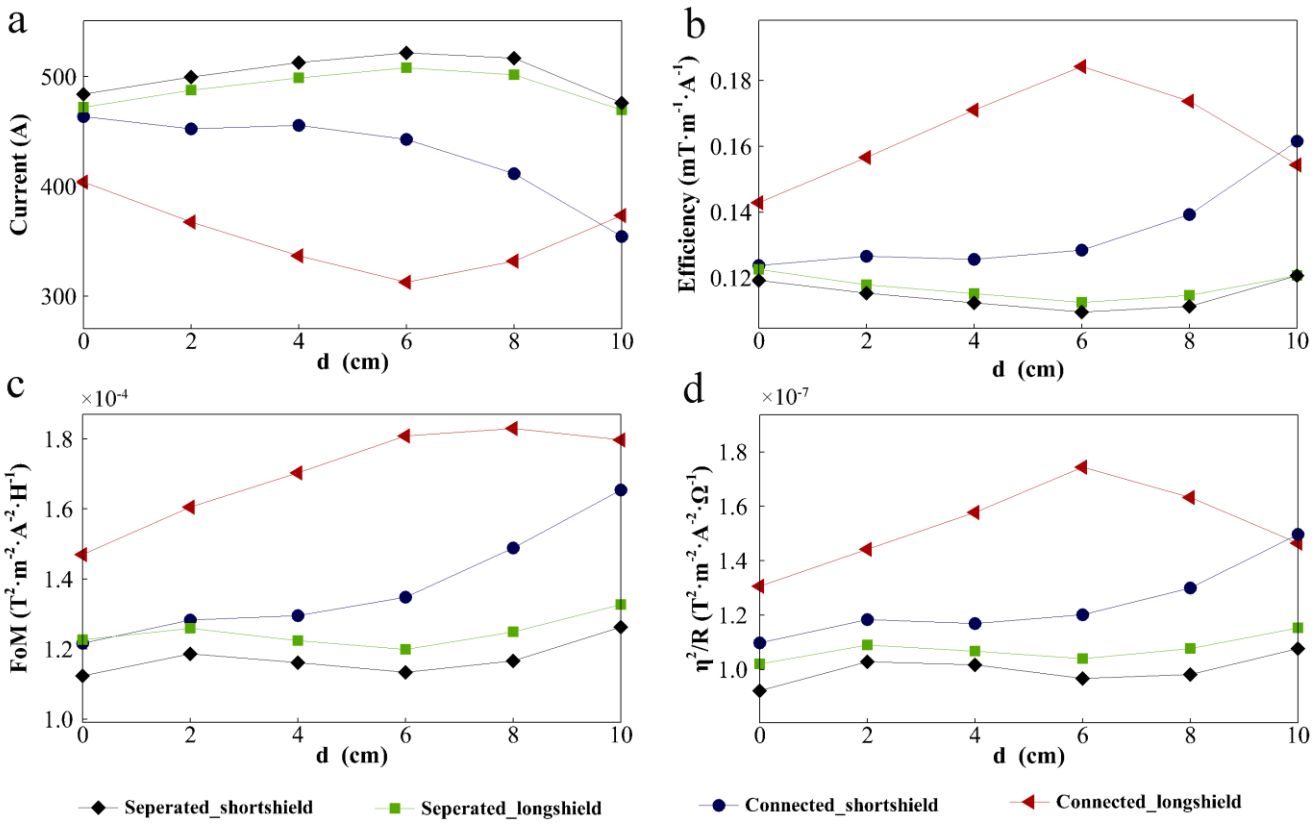

Figure 4.4. Coil performance of *x*-coil in the case of varying *d*, which is the distance between the coil edge and ROU edge, (a) current, (b) efficiency, (c) resistance, (d) η^2/R, (e) inductance, (f) FoM

Figure 4.5 presents the power dissipated on the cryostat. The cryostat is composed of a warm bore, first cold shield and secondary cold shield (shown in Figure 4.1). The warm bore is made of stainless steel and the cold shields are made of aluminium. The properties of the cryostat are shown in Table 4.2 [108, 121].

Table 4.2 Properties of the cryostat

	Length (m)	Radius (cm)	Thickness (mm)	Material	Conductivity (MSm-1)
Warm bore	1.41	43.1	6	steel	1.1
First cold shield	1.39	44.3	3	aluminium	38
Secondary cold shield	1.37	45.3	3	aluminium	1200

The coil designed with the long secondary coil dissipates less power on the warm bore, first cold shield and secondary cold shield (Figure 4.5). This demonstrates that the long secondary coils are effective in shielding the field leaked by the primary gradient coils and reducing eddy currents on the cryostat, thus protecting the desired magnetic field produced by the coil in the ROU. The connected coil with the short shields shows the highest power loss on the cryostat; thus, this design may produce the most eddy currents and have the worst shielding effect, while the separated coil with the long shield has the best shielding effect.

Generally, the connected coils have a better performance than the separated coils, and the coils designed with the long shield have a better performance than the short shield coils and dissipate less power in the cryostat. Therefore, the connected coil with the long shield has the best performance of the four designs. Furthermore, the coil designed with d = 6 cm has the best performance, considering the sizes of the human head and neck. A *d* of 4 to 6 cm is recommended in the design of the head coil.

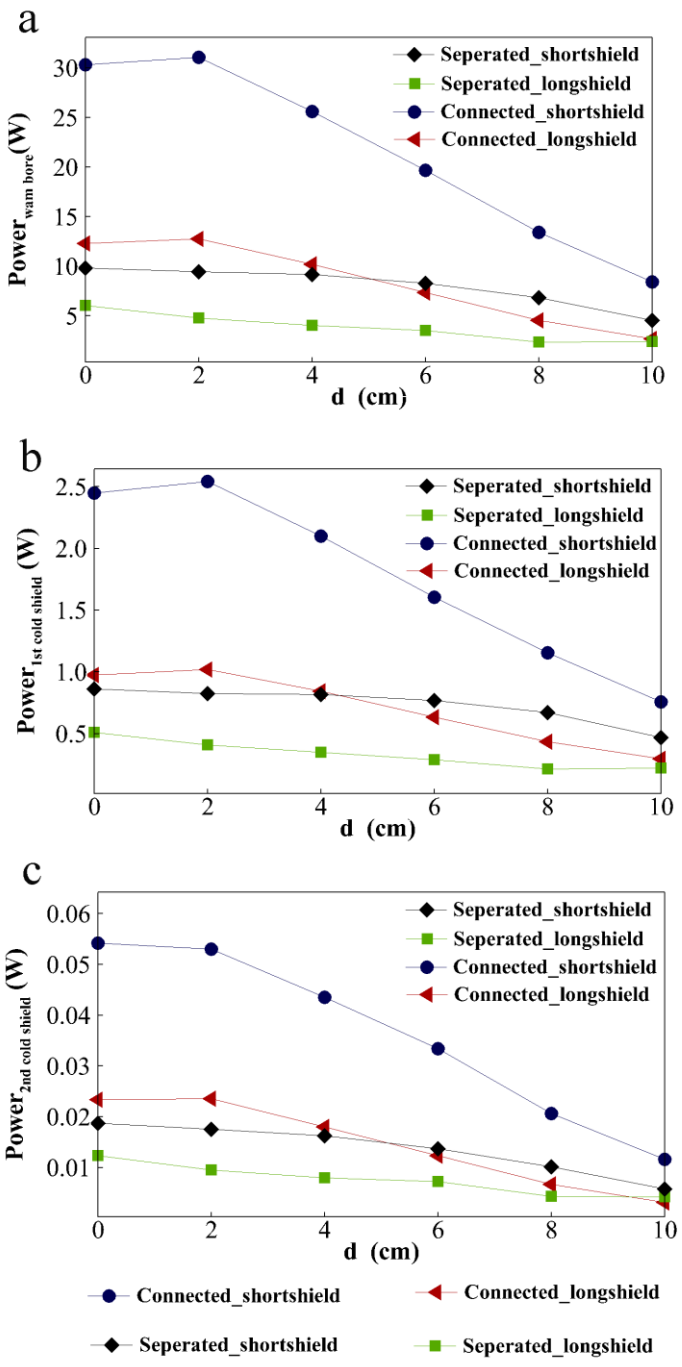

Figure 4.5. Power dissipation in the cryostat in the case of varying distance d, (a) warm bore, (b) first cold shield and, (c) secondary cold shield

For the clarity and ease of comparison of the different gradient coil structures, we designed the four coil structures with similar driving currents to produce the target gradient strength at d = 4 cm. As reported in

Table 4.3, the efficiency of the four coils is similar because of the same driving currents and the same target gradient strength. It can be seen that the connected coils have a lower inductance, higher FoM and slightly higher η^2/R than the separated coil. The inductance of the connected coil with the long shield is about 16.6% lower than that of separated coil with the long shield, and the FoM is about 24.1% higher than the corresponding separated coil.

Table 4.3 *x*-coil performance

	Separated short shield	Separated long shield	Connected short shield	Connected long shield
Current (A)	334.3	340.0	341.8	336.7
Efficiency (mT/m/A)	0.172	0.169	0.168	0.171
Inductance (μH)	237.7	217.4	205.9	171.8
Resistance (mΩ)	190.7	183.1	180.9	185.4
FoM (T^2 m^{-2} A^{-2} H^{-1})	1.25×10^{-4}	1.32×10^{-4}	1.37×10^{-4}	1.70×10^{-4}
η^2/R (T^2 m^{-2} A^{-2} Ω^{-1})	1.56×10^{-7}	1.57×10^{-7}	1.56×10^{-7}	1.58×10^{-7}
Minimum Spacing (mm)	5.4	5.4	7.7	7.7
Power dissipated in three-layer-cryostat (W)	9.9	4.3	27.3	11.1

Figure 4.6 presents one-half of the winding patterns of the four coil structures in Figure 4.3. The wire positions are unwrapped from the cylinder surface. The connected coils have one more wire group at the connected surface, which allows the current to flow from the primary to the secondary coil and improves the coil performance. Each loop must be connected to its neighbouring contours to ensure current flow throughout the coil during construction, which slightly increases the coil resistance and reduces the value of η^2/R, but the differences between connection and disconnection are well below 3%. Additionally, the connected coil with the long shield in Figure 4.6d has more-evenly spaced wires, with a minimum wire spacing of 7.7 mm, while the separated coil can only achieve 5.4 mm. So, the connected coil spreads the wires better and should be easier to manufacture. Additionally, this may reduce the intra-coil eddy currents between wire turns [16, 122] and disperse the localized Joule heating in the coil.

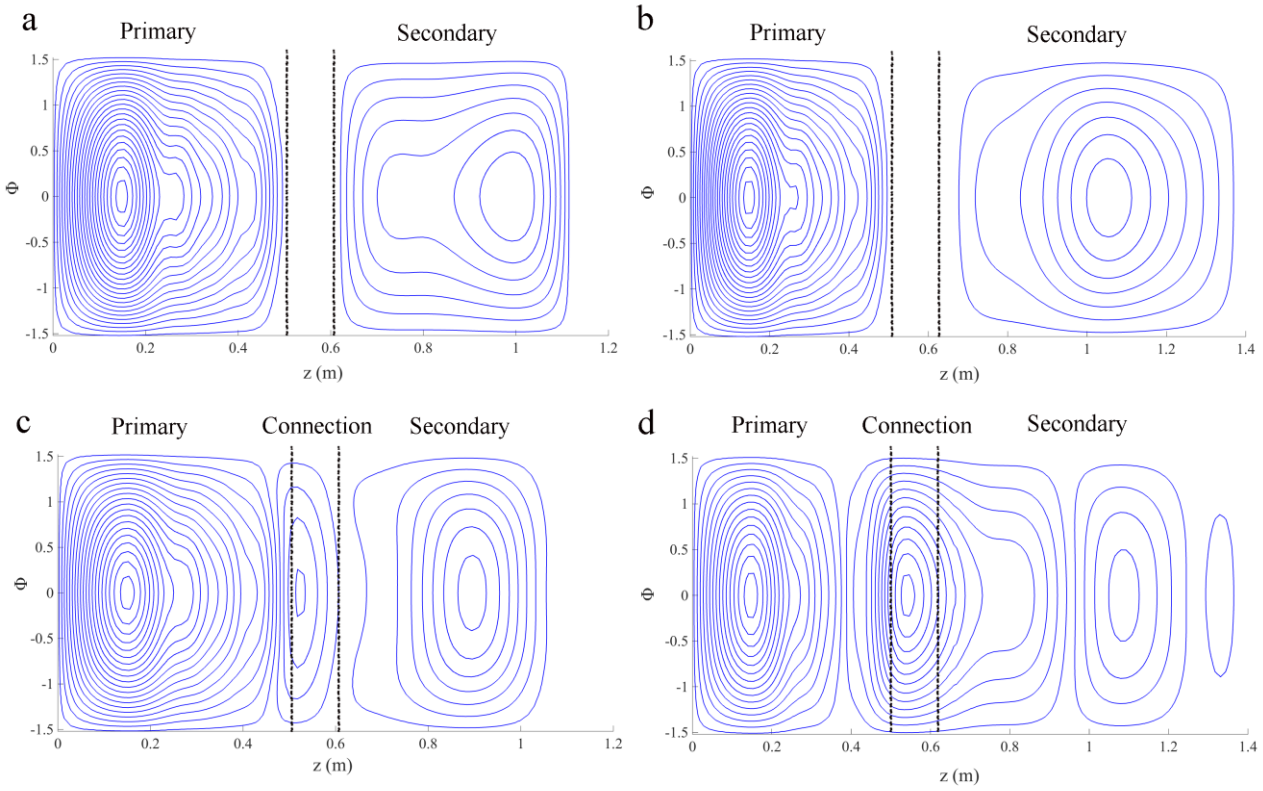

Figure 4.6. Winding patterns of the *x*-coil designed with different structure models, (a) separated coil with short shield, (b) separated coil with long shield, (c) connected coil with short shield and, (d) connected coil with long shield.

Figure 4.7 presents the magnetic field map of the four different prototype coils. The magnetic field is calculated in the *x*-*z* plane for $y = 0$ (green lines). The red line indicates the field error between the target field B_z^t and the field produced by the coil B_z and the ROU is marked as the oval yellow-green shade. The approximately straight superimposed lines within the ROU indicates that the magnetic field are uniform in the ROU. In addition, there is no appreciable difference between the magnetic fields in the ROU. However, to maintain the 5% field error, the minimum spacing between the wires is reduced for the separated coils, which introduces difficulties in the manufacturing process.

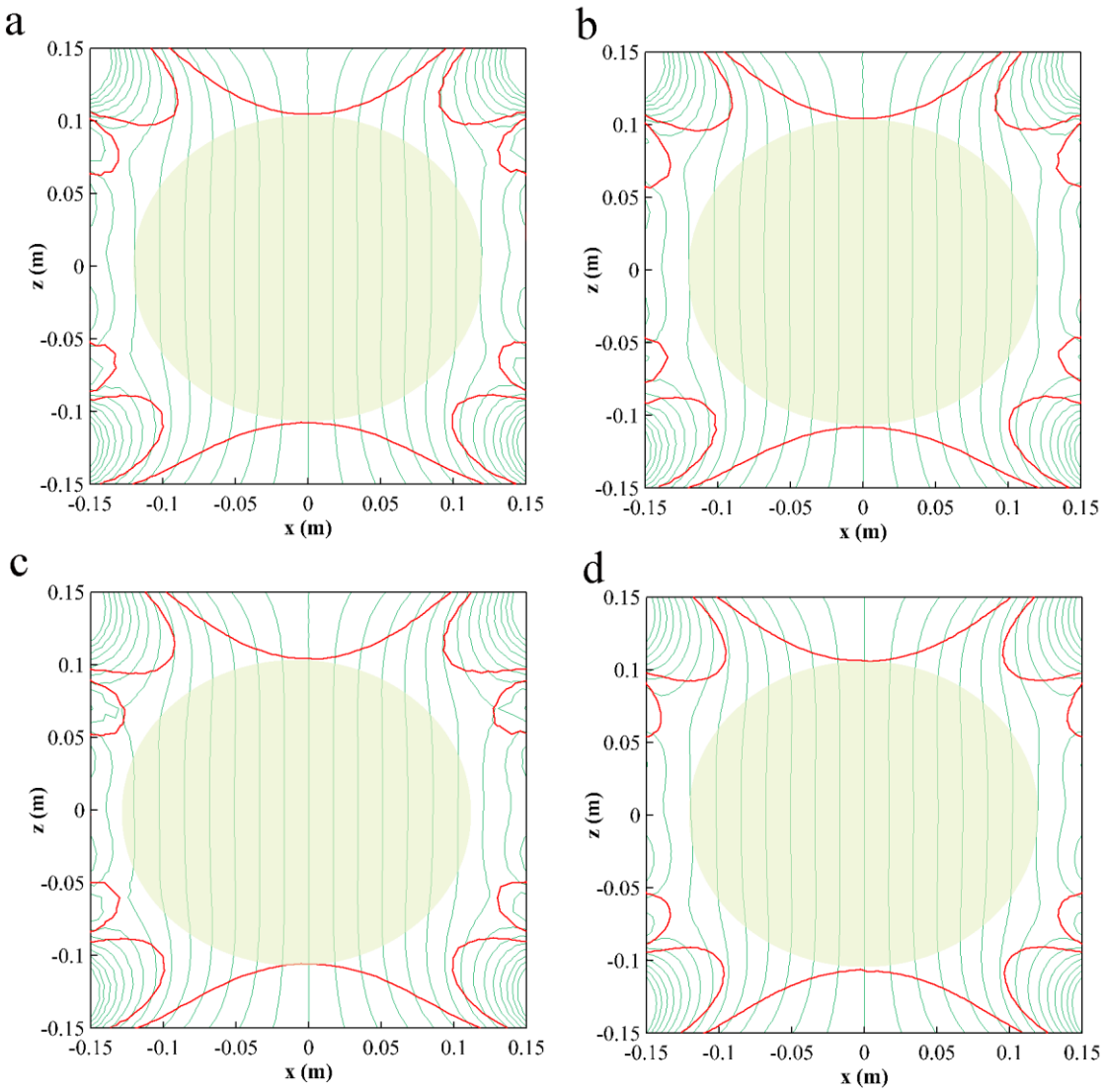

Figure 4.7. Magnetic field map of different coil structures; the green lines are 10 μT contour lines, the red lines are 5% field error contours, the oval yellow-green shade is the ROU, (a) separated coil with short shield, (b) separated coil with long shield, (c) connected coil with short shield and, (d) connected coil with long shield.

The eddy currents induced in the whole three-layer-cryostat including warm bore, first cold shield and secondary cold shield (shown as Figure 4.1) were calculated. [108]. Figure 4.8 presents the secondary magnetic field generated by the eddy currents of the three-layer-cryostat in the *x*-*z* plane at $y = 0$. The connected coil with the short shield (Figure 4.8c) produces the largest secondary magnetic field in the *x*-*z* plane; thus, it is the worst shielding effect coil. Figure 8a, b and d do not have any significant differences. In

a detailed observation, however, the field at the edges along *x*-axis of the plane in Figure 4.8b and d are more linear than the secondary field in Figure 4.8a. This indicates that using a pre-emphasis technique to compensate the secondary field for the coils with long shield [123, 124] has the potential to be more effective for the long connected shield design.

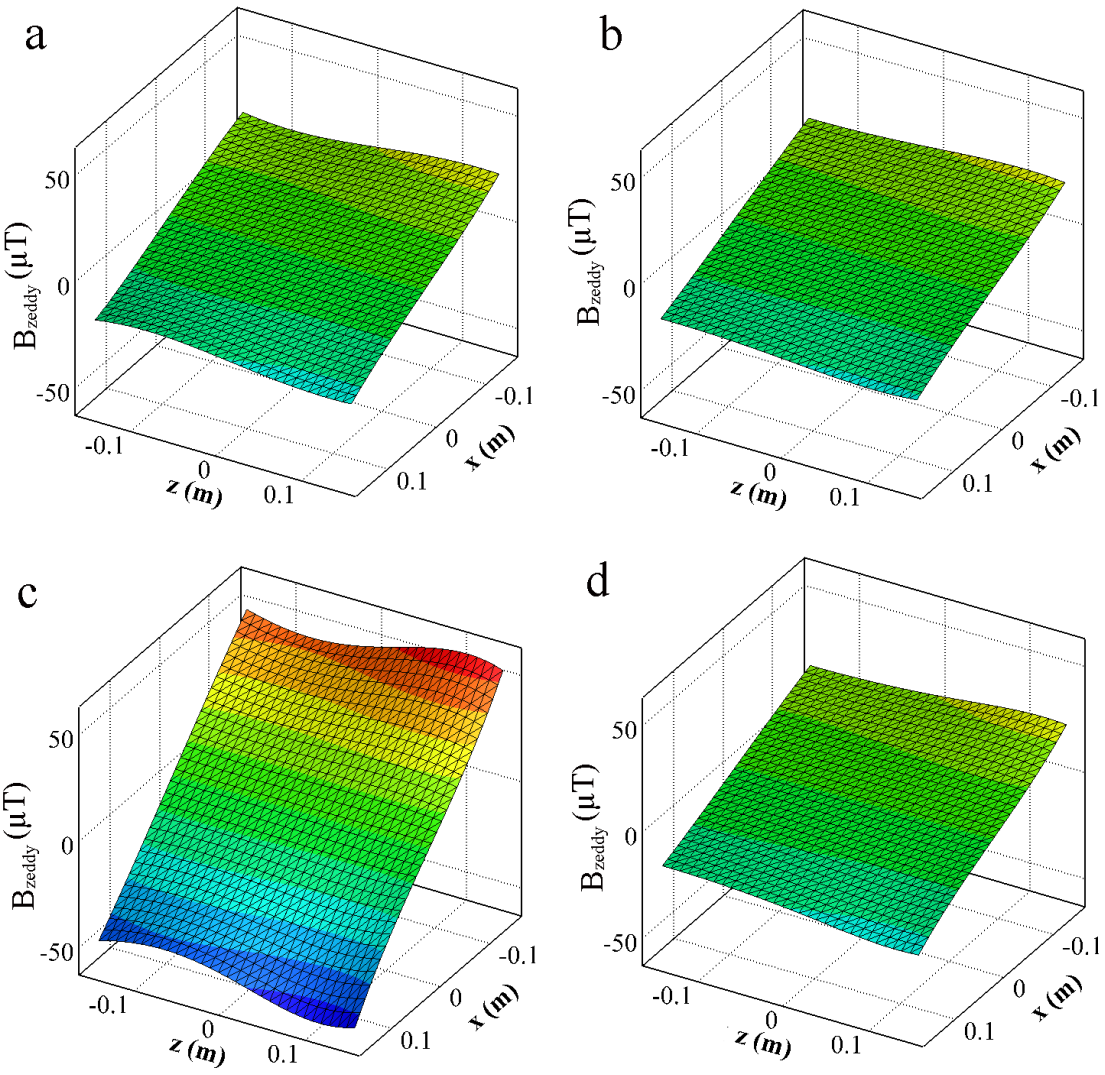

Figure 4.8. Magnetic field produced by the eddy currents on the three-layer-cryostat induced by the *x*-coil, (a) separated coil with short shield, (b) separated coil with long shield, (c) connected coil with short shield and, (d) connected coil with long shield.

4.3.2 Longitudinal coil

The example wire patterns of the *z*-coil are shown in Figure 4.9. To keep the 0.2% shielding ratio and the field error to less than 5%, the wires of the separated coils (Figure 4.9a and b) accumulate close to the patient end, thus leading to manufacturing difficulties. The connected coil with the long shield has less wire turns than the other three structures and has a larger minimum spacing between the wires.

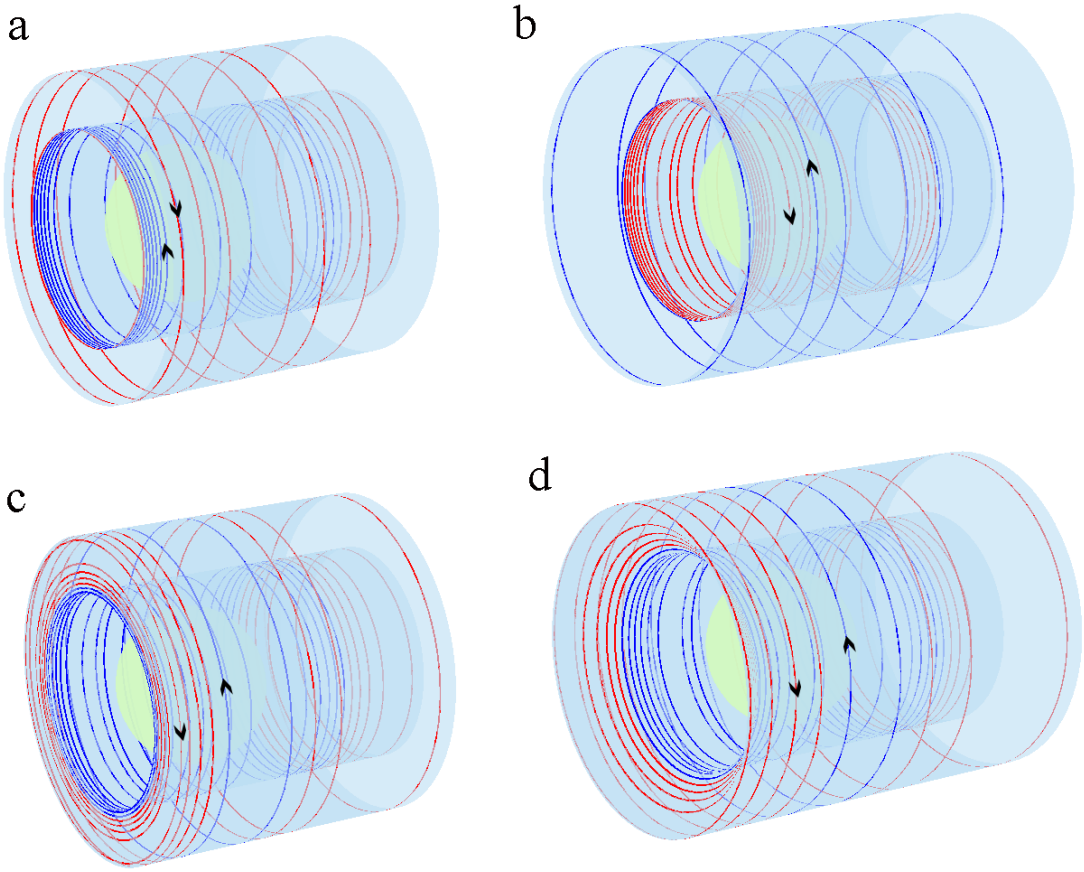

Figure 4.9. Winding patterns of the *z*-coil designed with different structures, (a) separated coil with short shield, (b) separated coil with long shield, (c) connected coil with short shield and, (d) connected coil with long shield.

Figure 4.10 presents the performance of the *z*-coil by changing the distance *d*. Because of the structure of the *z*-coils and the large ROU, the gradient field error cannot reach 5% at $d = 0$ cm; therefore, here, *d* starts from 2 cm. The current required to drive the separated coils and the connected coil with the short shield is higher than 1000 A at $d = 2$ cm, which can cause hot spots in the gradient coils. In addition, the coils designed with

d = 2 cm have the worst performance, such as low efficiency, low FoM and η^2/R. Therefore, a small d is not recommended for use when designing the asymmetric coils. The connected coils with long shield is the best structure, because of the low operating current, high efficiency, FoM and η^2/R. The performance is relatively stable for the connected long shield coil when d > 6 cm; therefore, d = 6 cm is the best option for designing the connected long shield coil. However, considering average sizes of the adult human head, 4 cm <d < 6 cm is recommended when designing the z-coil, and this distance is in accordance with the x-coil optimum.

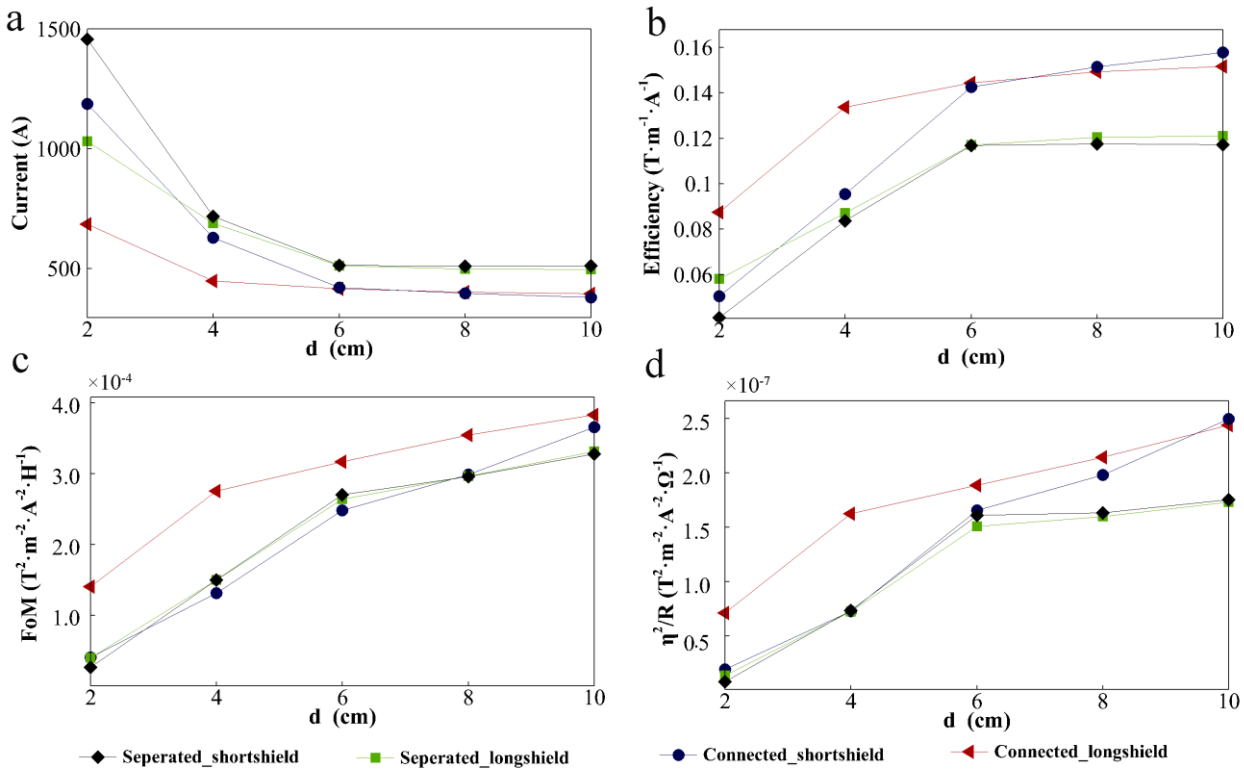

Figure 4.10. Coil performance of the z-coil in the case of a varying d, which is the distance between the coil edge and the ROU position, (a) current, (b) efficiency, (c) resistance, (d) η^2/R, (e) inductance and, (f) FoM

Table 4.4 shows the performance of the z-coil designed with different models at d = 6 cm; the coils were designed with similar currents to make the coils comparable. The separated coils and the connected coils with the short shield have a similar performance, while the connected z-coil with the long shield is better than other models. The inductance and resistance of the connected coil with the long shield is 14.5% and 9.8% smaller than the corresponding separated coil; the FoM and η^2/R are 13.2% and 20.2% higher than the separated coil with the long shield. Moreover, the z-coil with the long shield dissipates less power on the cryostat. To keep the field linearity and control the leakage field close to the cryostat, the wires of the

separated coils close to the patient end are crowded, having a minimum wire spacing of about 5 mm. By comparison, the minimum spacing of the connected long shield *z*-coil is 14.3 mm, because of the contribution of the turns on the flange between the primary and secondary coils.

Table 4.4 *z*-coil performance

	Separated short shield	Separated long shield	Connected short shield	Connected long shield
Current (A)	513.7	512.3	530.8	506.4
Efficiency (mT/m/A)	0.117	0.117	0.113	0.118
Inductance (μH)	50.4	52.0	53.7	44.47
Resistance (mΩ)	84.7	91.0	94.2	82.0
FoM (T^2 m^{-2} A^{-2} H^{-1})	2.70×10^{-4}	2.63×10^{-4}	2.40×10^{-4}	3.16×10^{-4}
η^2/R (T^2 m^{-2} A^{-2} Ω^{-1})	1.61×10^{-7}	1.51×10^{-7}	1.36×10^{-8}	1.71×10^{-8}
Minimum Spacing (mm)	5.3	5.1	8.3	14.3
Power of three-layer-cryostat (W)	1.74	0.29	2.7	0.91

4.4 Conclusion

This work shows a new approach to the design of asymmetric head gradient coils. In our design, the patient end of the coil was connected between the primary and secondary coils, thus providing extra space for the wiring. The service end is open for the accommodation of the passive shimming sets and cooling pipes.

The simulation results showed that, for the transverse *x*-coil, the connected coils had a better performance than the separated coils, especially the connected coils with the long shield. The performance of the coils designed with similar currents to generate the same expected target gradient strength shows that: the FoM, inductance and minimum wire spacing of the connected coil with the long shield is improved around 24.1%, 16.6%, 42.6%, respectively, more than the corresponding separated coil. From the coils designed with the same stream contours, it was found that the optimal distance is d = 6 cm between the ROU edges and patient end for the connected coil with the long shield. Eddy currents induced in the cryostat by the four variants of coils were analysed; the results showed that the coils designed with the long shield dissipated less power in

the surrounding cryostat. Additionally, the connected coil with the long shield produced more power than the corresponding separated coil, but less than the other designs.

The longitudinal coil also benefited from the connected structure, because of the turns on the flange. From the coil designed with a similar current, the performance, such as the inductance, resistance FoM and η^2/R of the connected coil with long shield, were improved compared to the corresponding separated coil. Moreover, the connected coils with the long shield have a larger minimum spacing than other models, which makes it easier to manufacture and reduces potential hot spots in the coils. The coils with the long shield dissipated less power loss in the cryostat than the coils with the short shield. The distance d = 6 cm is also the optimal distance for the z-coil. Consequently, the connected long shield structure is recommended when designing the transverse and longitude asymmetric coils. Considering the performance and the dimensions of the human head and neck, d = 4 to 6 cm is recommended when designing the head coils.

5. Skin and proximity effects in the gradient coils

As discussed in Chapter 3, eddy currents induced in the surrounding conducting structures depend on the geometry of the conductor and the excitation waveform. One of these kinds of eddy currents is skin and proximity effects in the gradient coils, which is associated with coil track width and the applied frequency of the input waveform. In this chapter, the impact of the conductor width and the excited frequency on the parameters that characterise the performance of the conventional and split transversal gradient coils are studied.

Section 5.1 and 5.3 in this chapter are largely based on the journal article "Skin and proximity effects in the conductors of split gradient coils for a hybrid LINAC-MRI scanner" published in the *Journal of Magnetic Resonance* in February, 2014. The research untaken in these sections focuses on the study of inductive coupling between tracks of split gradient coils. Editing has been mainly carried out in the introduction for the best coherence with other chapters.

Publication details

Fangfang Tang, Hector Sanchez Lopez, Fabio Freschi, Elliot Smith, Yu Li, Miguel Fuentes, Feng Liu, Maurizio Repetto, Stuart Crozier, Skin and proximity effects in the conductors of split gradient coils for a hybrid Linac-MRI scanner, *Journal of Magnetic Resonance,* vol. 242, pp. 86-94, 2014.

Manuscript revision history

Submitted to *Journal of Magnetic Resonance*	9 October 2013
Interim Decision (major revision)	1 February 2014
Available online	12 February 2014

Author contributions

Fangfang Tang	Numerical modelling, code implementation,

	analysis and interpretation, manuscript preparation, experiment implementation
Hector Sanchez Lopez	Numerical modelling, code implementation, analysis and interpretation, manuscript reviews, Experiment implementation
Fabio Freschi	Numerical modelling, code implementation, analysis and interpretation, manuscript reviews
Elliot Smith	Experiment implementation, manuscript reviews
Yu Li	Experiment implementation
Miguel Fuentes	Experiment implementation
Feng Liu	Analysis and interpretation, manuscript reviews
Maurizio Repetto	Analysis and interpretation, manuscript reviews
Stuart Crozier	Analysis and interpretation, manuscript reviews

5.1 Introduction

As described in Section 2.2 and 2.4, the gradient coils are designed to produce a linear variation of the axial component of the magnetic field in the DSV [82]. To guarantee uniform gradient for high quality images, a range of parameters have been defined in Section 2.4.4 in the gradient coil design process [82]. A variety of different design methods have been developed to effectively constrain these parameters [82, 125, 126]. Some researchers have introduced "free-surface" coil design methods [127-129] based on a pioneering work of Pissanetzky [78]. These methods are able to produce gradient coils on arbitrary surfaces and, at the same time, control coil parameters with linear and quadratic dependence on the unknown current density. The current density is expressed as a function of a set of basis functions which represents the value of the stream function in the coil domain [130]. Equally spaced contours of the stream function define the position of the

current paths [130]. Commonly, the Biot-Savart law is used to evaluate the magnetic field produced by the coil assuming discrete and infinitely thin wire segments or tracks of finite dimensions. Usually coil tracks with a uniform current density are used to evaluate the magnetic field and other parameters from the designed coil.

Due to the skin and proximity effects, the current density tends to be non-uniform across the width of the conductor [12] and it is known that these effects increase with the frequency [12], especially in the modern MRI scanner, the gradient coils are usually etched or machined using wide copper sheet for power dissipation purpose [82]. Not taking into account the skin and proximity effects may lead to inaccurate modelling of the magnetic field profile expected from the gradient coil design. Moreover, it is known that power loss tends to increase with the frequency but the implications of the skin and proximity effect have not been investigated in detail for MRI gradient coils. The use of litz wire is one of the possible solutions used to lessen the severity of the skin effect and consequently lower the effective resistance and resistive losses. However, gradient coils manufactured using litz wires can be an expensive process as grooves typically need to be machined in fibre glass tubes to position the wires and this can be particularly difficult for some transverse coil designs [131].

To study edge-effects, a mathematical model that explains coupling between tracks was developed by Kroot [12, 89, 132]. However, in his work, only the current distribution in strips and islands were studied, but the effects caused by a non-uniform current density distribution along the track width on the coil parameters and field harmonics were not considered. In this section, we study the impact of the coil track width and frequency on the coil performance taking into account the skin and proximity effects for transverse split gradient coils [76]. We use the EMC method to design shielded whole body *x*-gradient coils for conventional MRI scanner and split gradient coils for MRI-LINAC system[129, 133]. The MIM is extended to analyse the designed coils and predict the influence of the track width and frequency on gradient coil performance [77].

5.2 Conventional coils

5.2.1 Methodology

In order to study the influence of the coil tracks on the coil performance, 16 conventional whole-body *x*-gradient coils were designed [99]. The maximum track widths varied from 2 to 30 mm with a step of 2 mm. We investigated *x*-coils here because they have a more complex geometry compared to *z*-coils. The surrounding *y* and *z* coils were not taken into account to simplify the simulation model, thus reducing the

computational burden. All the *x*-gradient coils were designed to produce a target gradient strength G_0 = 30 mT/m within a 50×50×40 cm ROI. The maximum field error was constrained to 5%. All the coils were designed with a minimum wire gap of 1 mm. The coil tracks were made of copper sheet of 2 mm thickness. Figure 5.1b shows an example of the *x*-gradient coil and Table 5.1 presents the coil properties.

The designed coils with different track widths were driven by a current with a frequency sweep in a range of 100 to 10 kHz using the MIM [108]. A three-layer-cryostat was taken into account to analyse the induced eddy currents caused by the switching of the gradient coils, with different track widths and frequencies. The structure and properties of the cryostat are shown in Figure 5.1a and Table 5.1. In addition, the non-uniform current density distribution in the coil tracks and the impact on coil performance of the imposed frequency and the track widths were investigated.

Table 5.1 Properties of the gradient coils and cold shield

	x-coil	Warm bore	1st cold shield	2nd cold shield
Material	copper	steel	aluminium	aluminium
Conductivity (MS/m)	59.5	1.1	38	1200
Thickness (mm)	2	6	3	3
Inner radius (cm)	33.95	43.1	44.3	45.3
Outer radius (cm)	41.47	N.A	N.A	N.A
Overall length (cm)	126	141	139	137

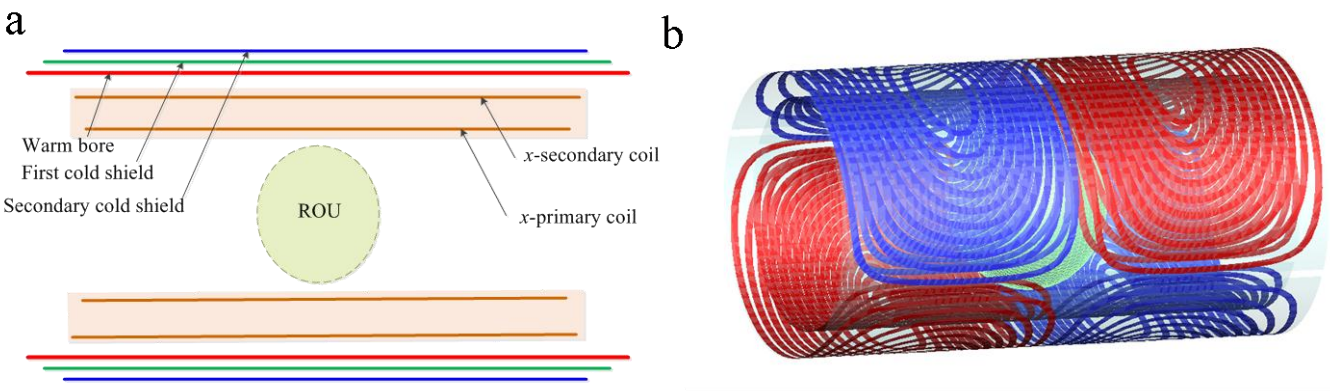

Figure 5.1 (a) three layers of cryostat and gradient coil geometry support, (b) example of *x*-coil.

5.2.2 Results and discussion

Figure 5.2 presents the current density distribution in 1/8 of the *x*-coil with a maximum track width of 30 mm and a frequency of 1 kHz. It can be seen that the current density tends to be higher at the track edges than in the internal part of the track and the current density distribution is asymmetric across the coil track width. And this is more evident in the tracks close to the coil eyes, where the tracks have a smaller curvature. This is also demonstrated by the current density profile in Figure 5.1b.

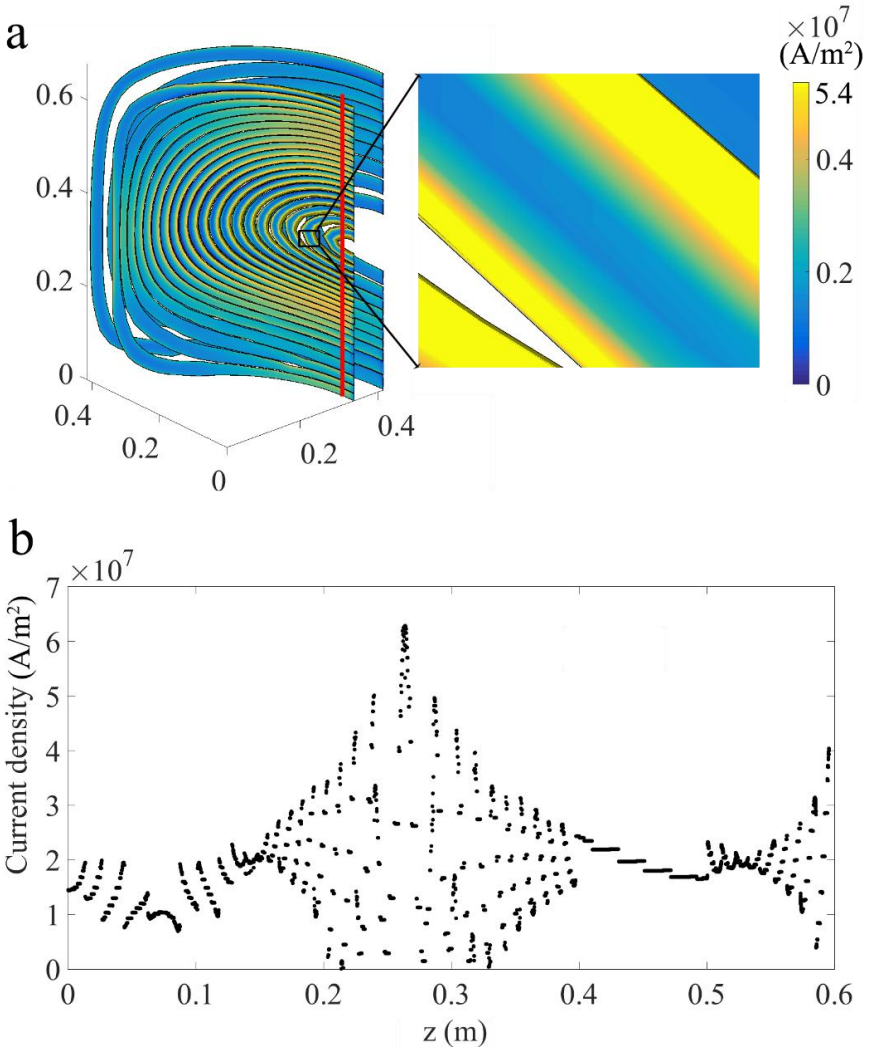

Figure 5.2 (a) current density distribution in the conventional *x*-gradient coil with a track width of 30 mm (1/8 of the *x*-coil), At the right appears a detailed current density profile; (b) spatial current density profile along the red line indicated in Figure 5.2a.

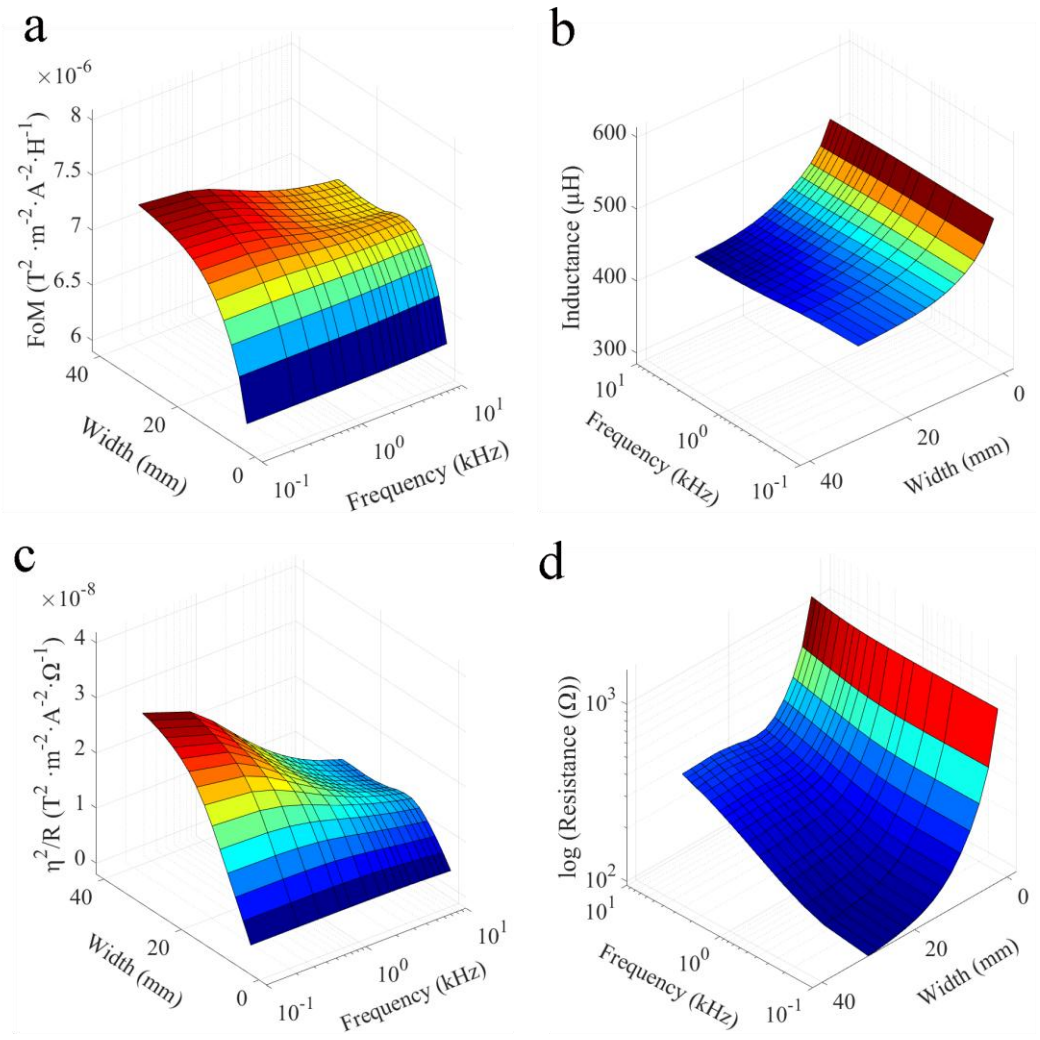

Figure 5.3 The performance of the conventional *x*-gradient coils by function of frequency and track width, (a) FoM, (b) inductance, (c) η^2/R, (d) log(Resistance).

The FoM shown in Figure 5.3a increases with the track width, especially at low frequencies. The FoM keeps relatively stable for track widths from 15 mm to 30 mm at frequencies higher than 1 kHz. However, the inductance has a tendency for a similar decrease with the track width at different frequencies. At low frequency, the current density tends to be evenly distributed across the track width, and thus the efficiency is slightly higher than in the case of high frequency and wide track width. Therefore, the FoM is higher for coils with wide tracks at low frequency. The factor η^2/R increases with the track width because of the decrease in the resistance, especially at low frequency. At high frequency, the coils with tracks of widths 15 to 30 mm have relatively low η^2/R, because the increment of the resistance with track width is more accentuated for

wide tracks than for narrow tracks. The wide tracks improve the FoM and η^2/R, but because of the skin and proximity effects, the current density is more non-uniform in the wide tracks than in the narrow tracks.

Figure 5.4 presents the real part of the harmonics produced by the coil with different track widths and frequencies. G_x, represents the linear terms of the *z*-component of the gradient field along the *x*-axis, which decreases with the increment of track width and frequency. Therefore, a narrow track width produces larger linear terms G_x due to the uniform current density distribution in the coil tracks. In contrast, Z2X and X3 increase with the track width and frequency. However, because Z2X and X3 are non-linear terms of the field, this affects the field linearity and distort image quality and should be mitigated. Therefore, narrow tracks can reduce the non-linear term of homogeneity and improve the linear term G_x.

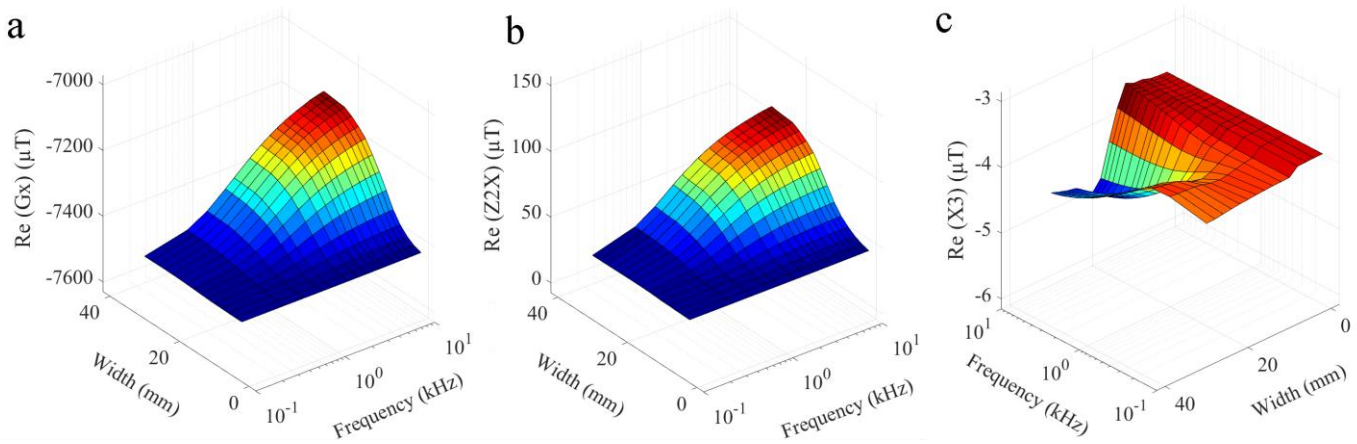

Figure 5.4 Real part of the field harmonics amplitude produced by the conventional *x*-gradient coils in the DSV, (a) G_x, (b) Z2X, (c) X3.

The harmonics G_x produced by the eddy currents in the three-layer cryostat tend to be smaller for wide tracks and low frequency (Figure 5.5a). However, Z2X increases with the track width and frequency. The zonal harmonics tend to disappear for both G_x and Z2X. In spite of lower G_x produced by the eddy currents induced by coils with wide tracks, larger Z2X is generated.

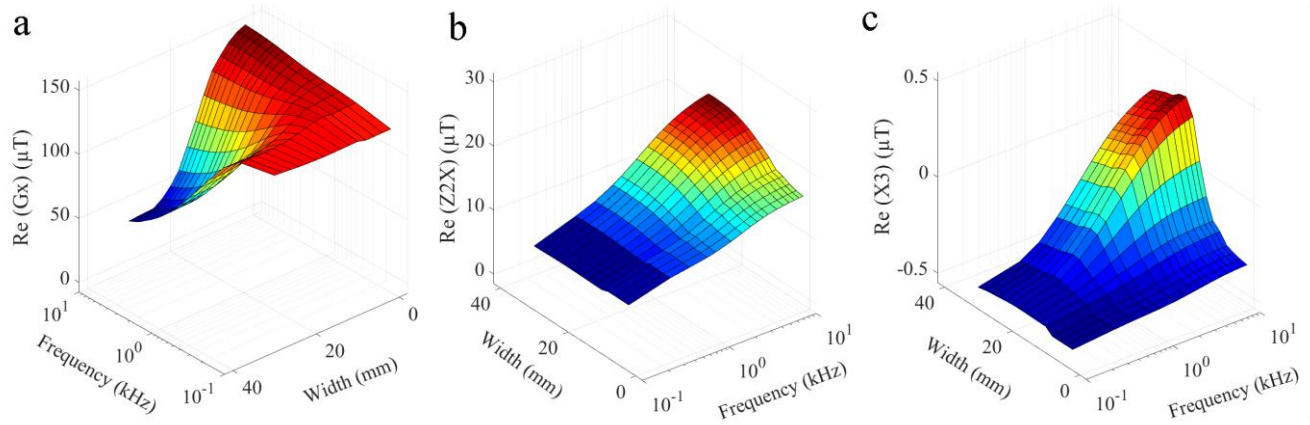

Figure 5.5 Real part of the field Spherical harmonics amplitude produced in the DSV by eddy currents and power loss induced in the cryostat, (a) G_x, (b) Z2X, (c) Z3.

5.2.3 Conclusion

In this section, we studied the impact of the track width and frequency on the coil performance because of the skin and proximity effects for conventional coils. It was found that the current density distribution is more non-uniform in the rapidly changing track paths, therefore, the rapidly changing tracks should be avoided in the coil design process. The parameters such as FoM and η^2/R increase with track width due to the lower inductance and resistance for wide tracks. This increment is more accentuated at low frequency. However, wide tracks produce lower G_x and higher Z2X at high frequency.

5.3 Split coils

5.3.1 Methodology

5.3.1.1 Coil Design

In order to study the influence of the track width and frequency variation over the coil parameters we designed 30 whole-body *x*-split gradient coils using equivalent magnetisation current [129]. The track width was changed linearly from 1 mm to 30 mm, the target gradient strength G_0 was kept at a constant value of 10 mT/m for all designs, the field linearity was fixed to 5% in a DSV of 460 mm and the target FoM was kept constant for all the designs.

We focused our study on the *x*-folded gradient coil due to its geometrical complexity compared to that of the *z*-gradient coil. In this work, we neglected the inductive coupling between the *x*-coil and the surrounding coils. This assumption simplifies the model and significantly reduces the computational burden and the number of variables that may influence the skin and proximity effect due to the coil self-inductive coupling. However, this represents a simplification of the scenario that is present in conventional MRI scanners. Depending on the spatial distribution of current and track width of the surrounding coils, it is possible for inductive coupling to occur between the *x*-coils and the rest of the gradient and shim coils. This complex interaction will be considered in a detailed analysis in future work. Figure 5.6 shows the split coil support, DSV and a simplified shield cryostat used to design the split gradient coils.

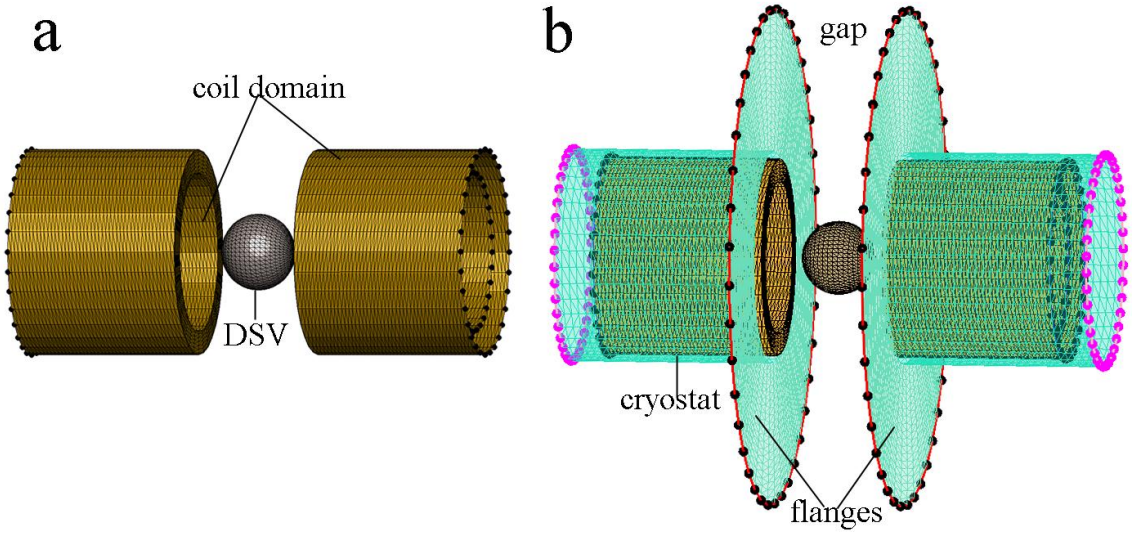

Figure 5.6 (a) split gradient coil geometry support and (b) simplified split cold shield cryostat.

The track width was changed from 1 mm to 30 mm with equal steps of 1 mm to produce a total of 30 *x*-gradient coils. The minimum gap between wires was constrained to 2.8 mm. Each of the modelled coils were simplified to 24 turns (4 turns per quadrant), as both the computing time and memory requirements increases with a factor O (N^2), where N is the number of nodes. A current of 1065 A was used to generate the target field of G_0. High current was required due to the small number of turns used to model the coil. The conductor thickness was uniform for each of the designed coils. We assumed that the coil domain is made of 2 mm thick copper sheet for the 30 coils. Two conductive cryostat cylinders, warm bore and cold shield were used as a simplified cryostat to analyse the eddy currents. The split cryostat structure is shown in Figure 5.6b. All the properties of the split transverse coils are listed in Table 5.2.

Table 5.2 Properties of split transverse coils.

	x-coil	Warm Bore	Cold Shield	Warm Bore Flange	Cold shield flange
Material	copper	Steel	aluminium	steel	aluminium
Conductivity (*MS/m*)	59.5	1.42	208	1.42	208
Thickness (mm)	2	3	4	12	6
Inner Radius (mm)	313	411	435	411	435
Length (mm)	1900	2378	2378	N.A	N.A
Flange Radial Length (mm)	9.06	645	582	645	582
Gap Size (mm)	500	512	552.8	512	552.8

5.3.1.2 Eddy current simulation using an extended MIM method

The multi-layer integral method (MIM) was used for eddy current simulations. The MIM divides thin volumes into multiple layers where each layer has a thickness smaller than the skin depth [77]. The MIM is applicable to arbitrary shape thin volumes where one of the linear dimensions is much smaller than the other two dimensions. In this work the MIM was extended to study the skin and proximity effects of gradient coil conductors and their interaction with surrounding conductors. We assume thin layered conductors so that the current density can be considered uniform along the conductor thickness [77]. The coil track is divided into a number of segments across its width in order to account for the skin effect. The divisions along the track width follow an exponential decay in order to cope with the skin and proximity effects. The number of divisions along the width is set to 10 according to a preliminary analysis of the coil with largest track width (30 mm) as this was considered to be a good compromise between accuracy and complexity. In this work the MIM is used to solve the diffusion equation of the time-harmonic current density [77].

The MIM method was descibed in section 3.3, However in this work the coils are discretised to tracks with finite width, hence in Eq.(3.33), $\mathbf{a}_s$ vanishes in this case. $\boldsymbol{\psi}$ is the complex vector of unknown values of the stream function in the domain Ω. With a suitable reordering of the unknowns, it is possible to partition the solution vector $\boldsymbol{\psi}$ into two sets:

$$\boldsymbol{\psi} = \begin{bmatrix} \boldsymbol{\psi}_i \\ \boldsymbol{\psi}_0 \end{bmatrix} \tag{5.1}$$

where $\boldsymbol{\psi}_i$ contains the unknowns values of the stream function at the internal nodes of the domains Ω. Internal nodes are those that do not belong to the boundaries of the conductive domains. $\boldsymbol{\psi}_0$ is a vector that contains the values of the nodes belonging to the domain boundaries. When considering the tracks, depending on the desired current direction the nodes of one side (boundary) of the coil track are set to zero ("grounded side") and nodes along the other side are set to $I_0(\omega)$. $\boldsymbol{\psi}_0$ may also contain grounded and "floating" values of the stream function in the boundaries of passive conductors. "Floating nodes" are those located at the boundary of these conductors, whose values are unknown but due to the physical constraints of the problem must remain the same for all the nodes belonging to the same boundary [134].

Eq.(5.1) can be written as:

$$\mathbf{Z}\boldsymbol{\psi} = 0 \tag{5.2}$$

where $\mathbf{Z} = \mathbf{R} + i\omega\mathbf{M}$ is the impedance matrix. Assuming that $\mathbf{Z}_{00}$ is the impedance matrix for those nodes belonging to the domain boundaries with known stream function values, $\mathbf{Z}_{i0}$ is the interaction of the boundary nodes with the internal nodes and $\mathbf{Z}_{ii}$ is the interaction between the internal nodes, then (5.2) is written:

$$\begin{bmatrix} \mathbf{Z}_{ii} & \mathbf{Z}_{i0} \\ \mathbf{Z}_{i0}^T & \mathbf{Z}_{00} \end{bmatrix} \begin{bmatrix} \boldsymbol{\psi}_i \\ \boldsymbol{\psi}_0 \end{bmatrix} = \begin{bmatrix} 0 \\ 0 \end{bmatrix} \tag{5.3}$$

hence

$$\boldsymbol{\psi}_i = -\boldsymbol{Z}_{ii}^{-1}\mathbf{Z}_{i0}\boldsymbol{\psi}_0 \tag{5.4}$$

The MIM extension to simulate the proximity effect between coil tracks was architected in Matlab (The MathWorks. Natick, USA) and the matrix $\mathbf{M}$ was calculated using Fortran90 in order to speed up the calculations. The singularity presented in the inductance calculation was solved by a combination of analytically [104] and numerical integration [105]. The current densities $\boldsymbol{J}(\boldsymbol{r}, \omega)$ are evaluated once $\boldsymbol{\psi}$ is

calculated [77], thus average power loss, torque, force and magnetic field produced in the domain Ω are evaluated.

We analysed 30 *x*-split gradient coils using the described method. The excited frequencies were swept from 100 Hz to 10 kHz to study the changes in the current distribution with frequency. This range was selected as it covers part of the commonly used current pulse series applied in MRI experiments.

5.3.1.3 Validation of the extended MIM

A testing coil was designed using GMSH [135] and simulated with MIM using two frequencies 100 Hz and 10 kHz in order to demonstrate that MIM is able to accurately reproduce the skin and proximity effects. As well as this, the experiment would demonstrate that there is a change in the spatial profile of the current distribution in coil tracks with the frequency. Figure 5.7a shows the testing coil made of 0.75 mm copper sheet. The track width was set to 50 mm and the smaller gaps were set to 10 mm. The central gap dividing the two branches was set to 50 mm. The amplitude of the stream function was set to 2 A (complex value, frequency domain) at the nodes belonging to one side of the coil edge while the nodes belonging to the opposite edge were grounded to zero. This was done to simulate a current of 2 A flowing through the coil.

The coil's overall width along the *x*-axis was 270 mm and the height was 360 mm along the *z*-axis. The vertical sections of the coil (along *z*-axis) were designed to be long enough to avoid possible effects coming from the returning path. Figure 5.7a also shows the points on which the magnetic field produced by the coil was measured.

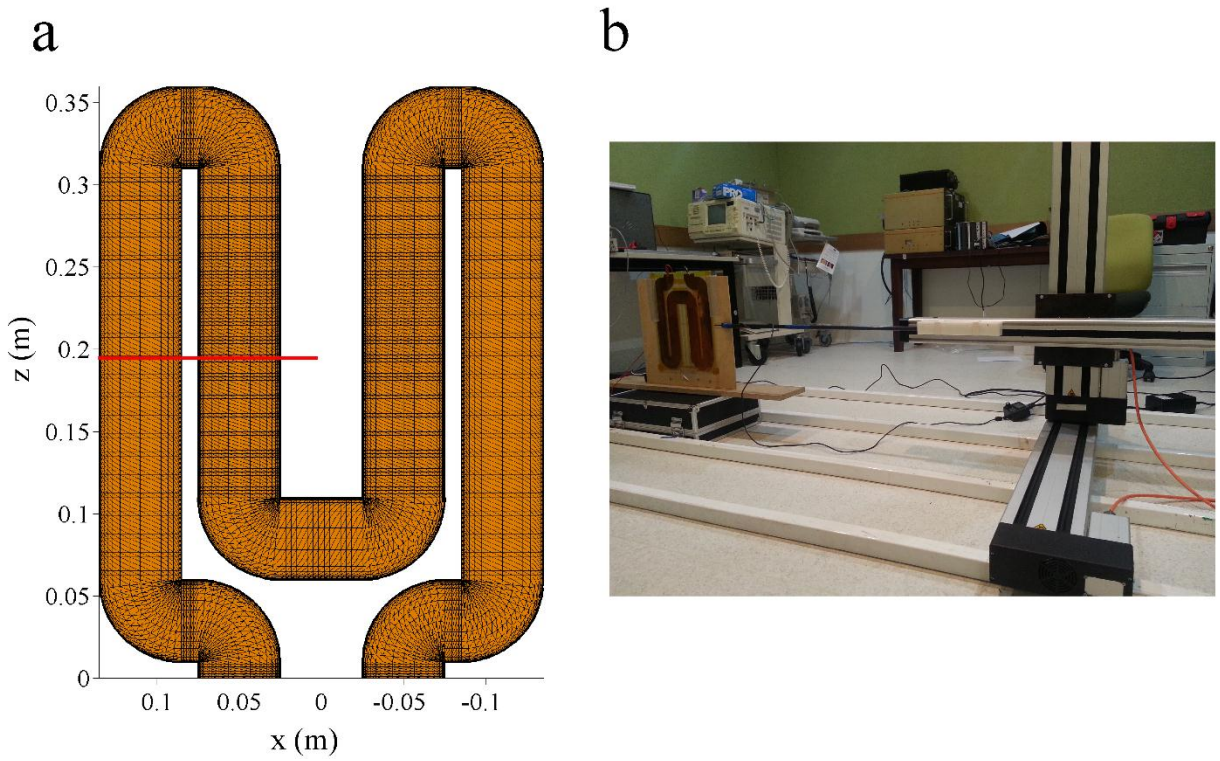

Figure 5.7 (a) testing coil-a coil structure for validation. The field component $B_x(x)$ was measured along the red line, (b) the experiment setup shows the coil, the 3-axis CNC machine and the TMR sensor at the tip of a carbon fibre rod. (For interpretation of the references to colour in this figure legend, the reader is referred to the web version of this article.)

Figure 5.7b describes the experiment setup. The picture shows the computer numerical controlled (CNC) 3-axis machine used to move the sensor along the red line represented in Figure 5.7a. A DC coupled wide band amplifier was used to produce a current of 2 A to drive the coil at the testing frequencies. A low-noise single-axis magnetic field sensor TMR STJ-220 with AL-05 signal conditioning board (Micro Magnetics) was placed at y = 5 mm above of the testing coil. The computer numerically controlled axis was used to move the sensor from x = -150 mm to x = 0 at z = 185 mm with an increment value of 1 mm along the line shown in Figure 5.7a. The field component $B_x(x)$ was measured in the experiment for frequencies of 100 Hz and 10 kHz to compare with the values predicted by the extended MIM.

5.3.2 Results

5.3.2.1 Validation and convergence

A comparison of the magnetic field predicted by the extended MIM and that measured at the frequencies 100 Hz and 10 kHz is shown in Figure 5.8 as is the current density distribution profile at 10 kHz. The testing coil was discretised using 24798 planar triangles and the simulation using the extended MIM was completed in 7 mins using an Intel® Core(TM) i7 CPU with 16 GB of RAM. The result shows strong agreement between the measured values and results predicted by the extended MIM. The results also illustrate a change in the magnetic field profile for the frequencies 100 Hz and 10 kHz. The skin depth penetrations at these frequencies are 6.5 mm and 0.65 mm, respectively. This effect is due to the change of the current density profile with the frequency. The current density tends to increase at the edges of the coil track therefore the field profile shows "a double-hump" shape. The double-hump is asymmetric due to the proximity effect of the two inner sides of the coil track. A colour map of the current density magnitude at 10 kHz gives appreciation of the heterogeneity of current flow (Figure 5.8b).

A typical current density profile of the parallel conductor along the red line indicated in Figure 5.8b shows that current density at the inner edge is higher than external edge (see Figure 5.8c). This is the main cause of the asymmetric double-hump shape of the B_x field component along the measured points. For 100 Hz the field profile is symmetric along the coil track width which corresponds to a uniform distributed current density profile along the track width. This experiment indicates that assuming the coil as filamentary could lead to inaccuracies in the evaluation of critical parameters such as power loss in the coil and cryostat and magnetic field generated in the DSV. Accurate evaluation of the gradient coils considering skin and proximity effects will provide opportunities of insight into the mitigation of eddy current effects in modern scanners.

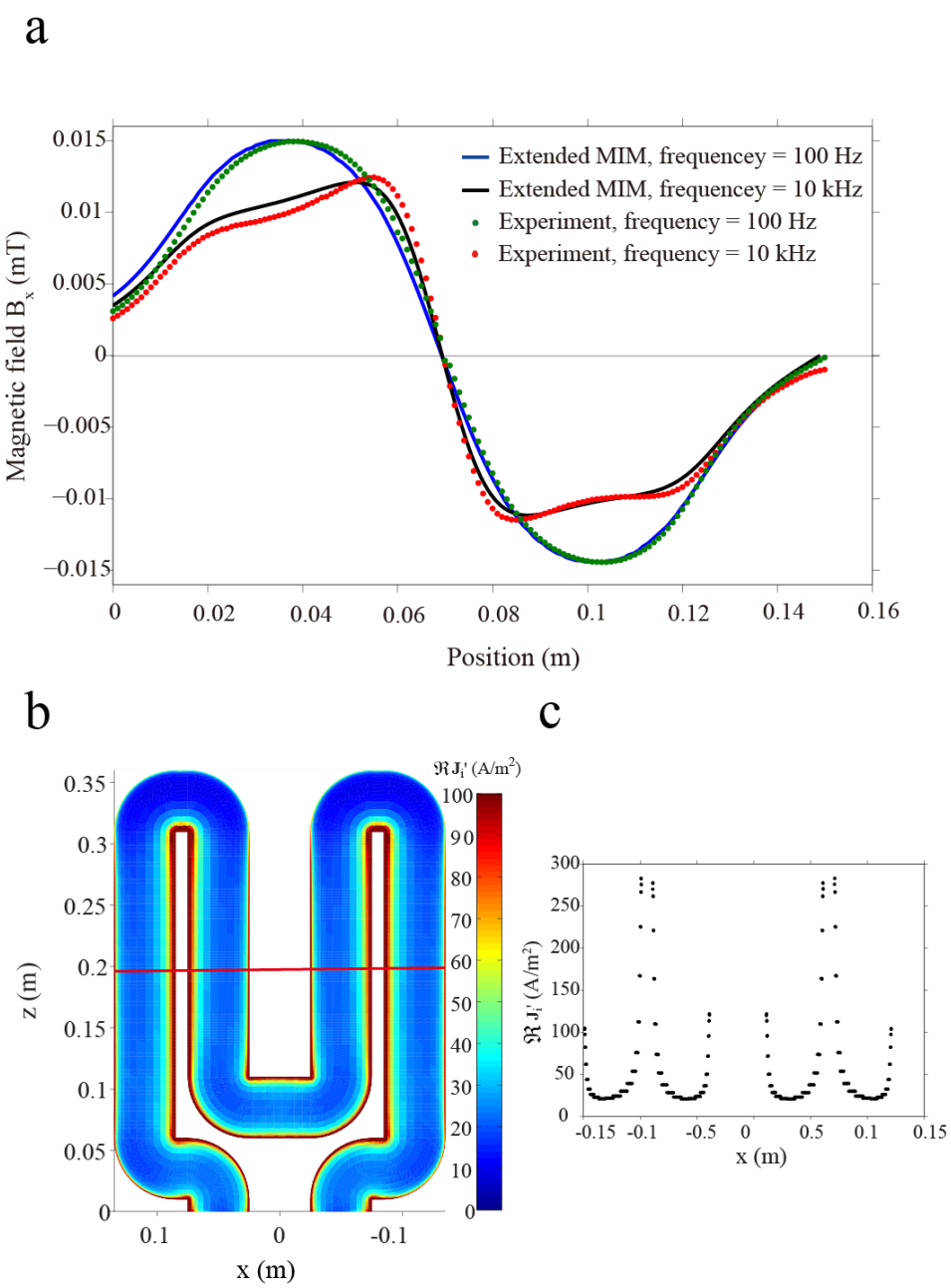

Figure 5.8 (a) the comparison of the magnetic field predicted by extended MIM and measured in experiment, (b) the current density distribution in testing coil (f = 10 kHz); (c) spatial current density profile along the red indicated Figure 5.8b.

5.3.2.2 Simulation Results

Figure 5.9 shows the colour map of the current density distribution and the current density profile along the red line in Figure 5.9a of a split *x*-gradient coil with the 30 mm track width. The extended MIM was used to calculate the current density when the gradient coil is driven by a sinusoidal current at the frequency of 10 kHz. The number of nodes was 30349 and the simulation was completed in 22 mins using an Intel® Core(TM) i7 CPU with 20 GB of RAM. This illustrates asymmetric current density distributions along the track width. This effect is more accentuated on those coil tracks with sharp turns, such as the turns located between the primary cylinder and the front flange. Asymmetries are more evident for tracks with a small radius of curvature and in presence of uneven spacing between adjacent tracks.

The tracks close to the coil "eye" produce a higher current density and hence power loss than those tracks that exhibit smooth spatial variations. A possible solution to mitigate this issue could be the use of the minimax current density [136, 137] or to seek a design in which the current path is smooth for all coil tracks by avoiding rapid changes of the current density direction[138].

The dependence of FoM, η^2/R, resistance and coil inductance with respect to frequency and track width for the 30 split *x*-gradient coils including the interaction with the cryostat is shown in Figure 5.10. The dotted-line illustrates the variation of the corresponding parameters produced by the coil with filamentary approximation.

The FoM increases when the track width increases, this tendency is mainly due to the tendency of the inductance that decreases with the track width (see Figure 5.10b). The inductance tends to slightly decrease with the frequency, but we observe that the change in the inductance with the frequency is nearly imperceptible and it has little impact on the FoM. The factor η^2/R increases with the track width as the resistance decreases with the increment of the track width (see Figure 5.10d). However, the η^2/R tends to decrease with the increment of the frequency and this effect is more accentuated in wider tracks. At low frequency the current density is evenly distributed along the track width therefore the coil efficiency is larger than that produced at high frequencies where the current density occupies a small section of the track surface. We conclude for this part of the study that wider tracks produce gradient coils with high η^2/R. But for wider tracks at high frequencies the FoM tends to increase slightly. However, Figure 5.10d illustrates that the

increment of the resistance with the frequency is more accentuated for wider tracks than that values produced by narrow tracks. This deleterious effect is imperceptible in the factor η^2/R.

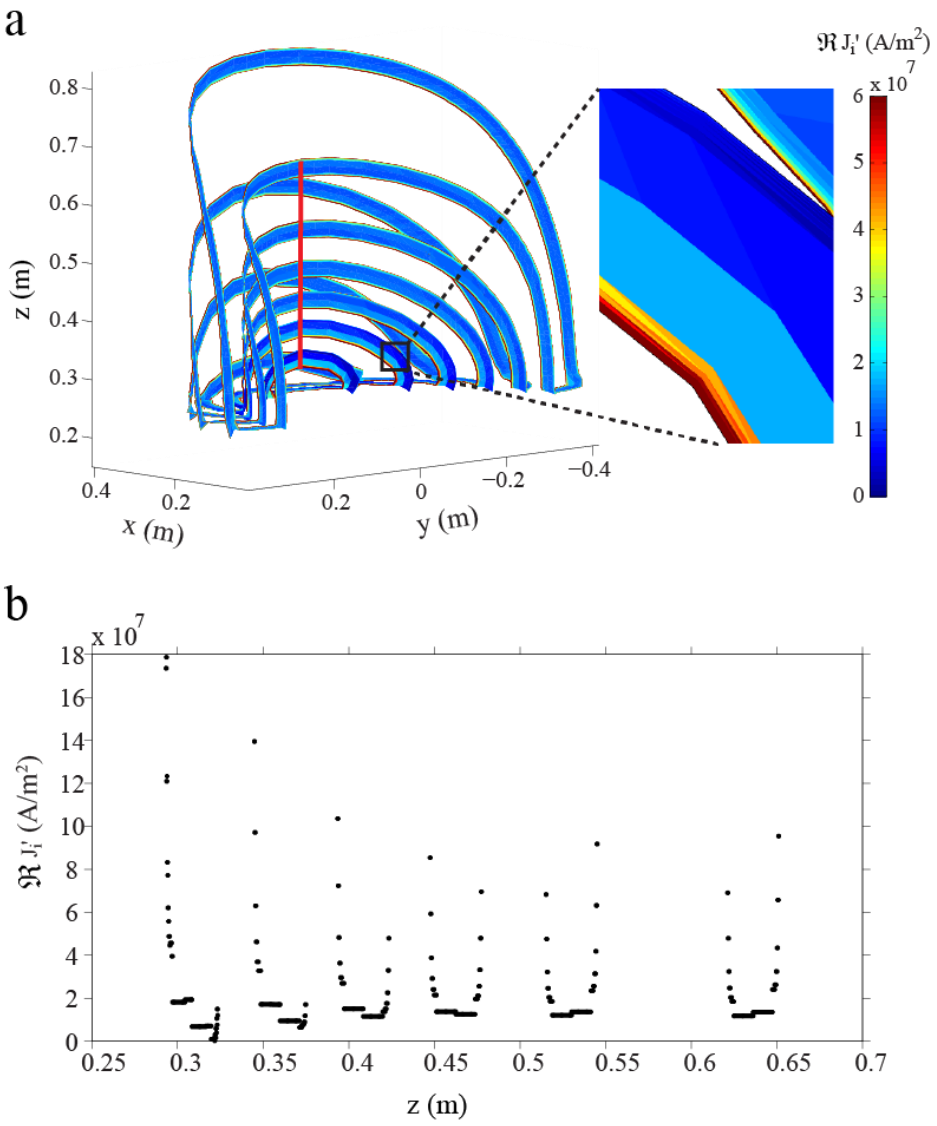

Figure 5.9 (a) current density distribution for the split *x*-gradient coil with tack width 30 mm, the picture reproduces only 1/4 of the complete structure which is fully modelled. At the right appears a detailed current density profile. (b) spatial current density profile along the red line indicated in Figure 5.9a.

It is known that due to the skin effect the resistance tends to increase with the frequency however the results show that this effect is more critical for coils with larger tracks widths. The use of smaller tracks width mitigates this deleterious consequence caused by the skin effect; however larger tracks width produces less

Joule power than that generated by thinner tracks. In order to achieve an optimal trade-off between track width and power loss a temperature analysis is demanded, as it is not obvious that wider track produces less power loss than narrow conductor tracks. It seems that wider track produces a large FoM and η^2/R but the deleterious effect of the skin effect is emphasized more in wider tracks than narrow tracks.

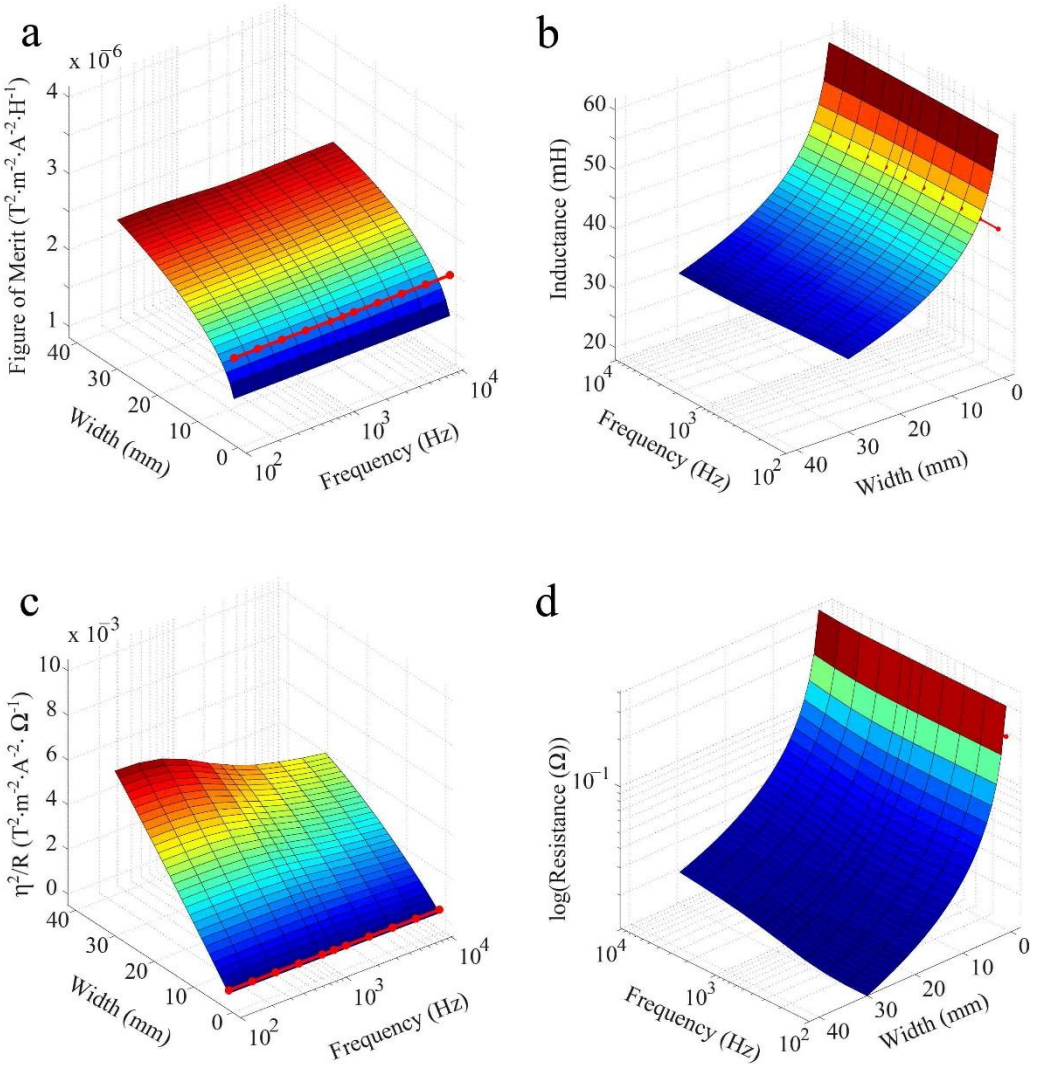

Figure 5.10 the performance of the *x*-gradient coils on function of frequency and track width, (a) FoM, (b) inductance, (c) η^2/R, (d) log(Resistance). The dotted-line is corresponding parameters produced by filamentary coils. For Figure 5.10b and Figure 5.10d, the dotted-lines are behind the curved surface.

The amplitude of spherical harmonics produced by the coil at different frequencies and track widths are shown in Figure 5.11; the dotted-line shows spherical harmonics produced by the filamentary coils due to different frequencies. The harmonics Z1, G_x, Z2X, X3 were calculated at the DSV. The Z1 harmonic tends

to increase for large track width and low frequency; the simulation shows that the Z1 harmonic for this particular coil design problem tends to disappear at high frequency. There is a tendency to reduce the coil efficiency η for coils of larger track width when they are driven at high frequencies due to the skin and proximity effects. This effect is reflected on the FoM (see Figure 5.10a).

The real part of the harmonics Z2X and X3 decrease with the frequency and the track width in this particular coil design problem. Narrow track widths produce stable harmonic amplitudes in frequency and predictable field harmonics in the DSV.

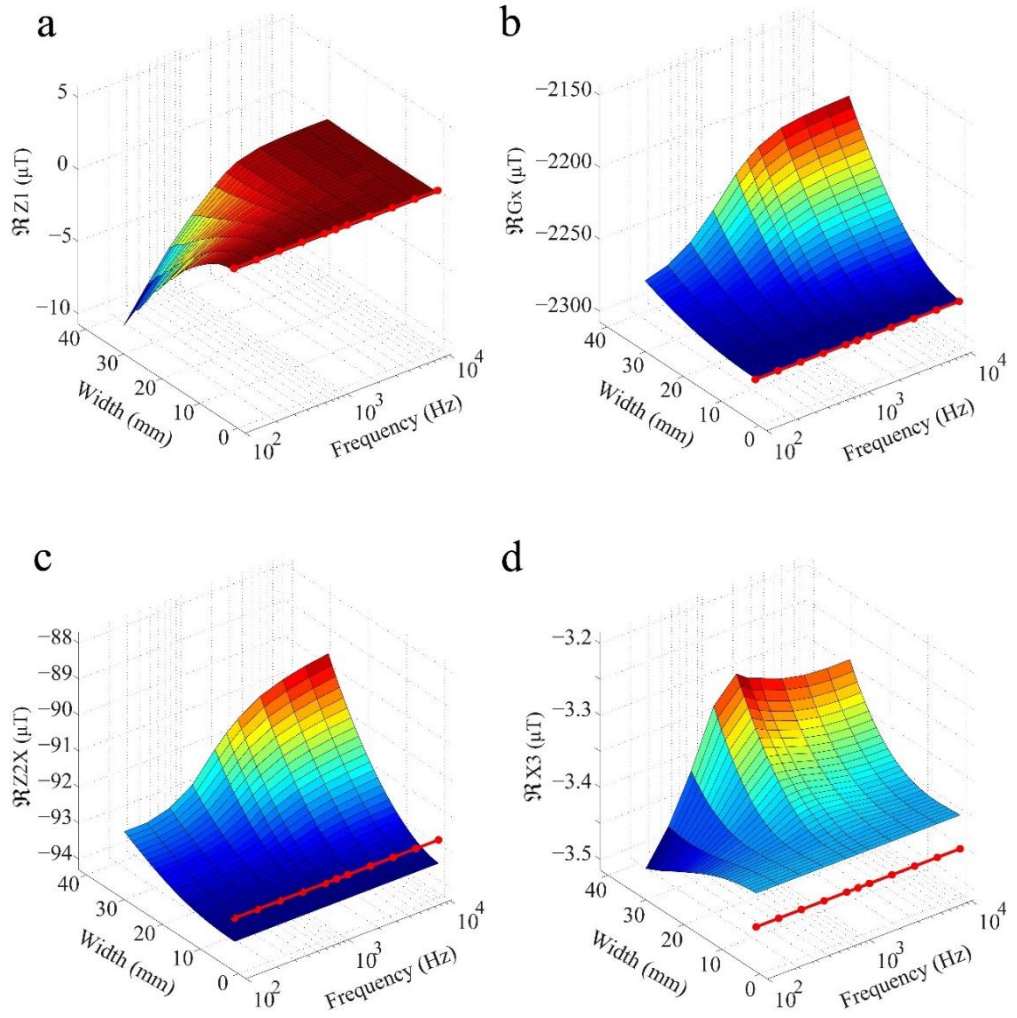

Figure 5.11 Real part of the field harmonics amplitude produced by the split *x*-gradient coils on the DSV, (a) Z1, (b) G_x, (c) Z2X, (d) X3. The dotted-lines are corresponding field harmonics amplitude produced by filamentary coil.

The change of the shielding ratio with the variation of the frequency and track width was next investigated (see Figure 5.12). Interestingly, the shielding ratio reaches a minimum value around 1 kHz. This is due to the fact that the coil was designed to control the shielding ratio at the target frequency of 1 kHz. A similar effect is shown in Figure 5.12b as the coil was designed in such a manner that the field produced by the induced eddy current is similar in shape to that field produced by the coil. An optimal pre-emphasis technique is clearly more difficult to achieve at high frequencies as the spatial shape of the secondary and primary field tends to deviate from each other.

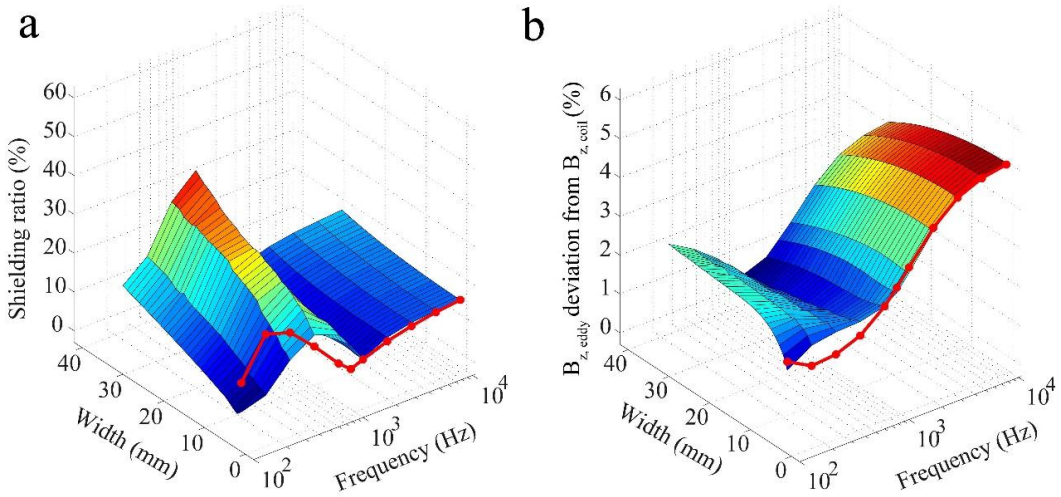

Figure 5.12 (a) shielding ratio and the (b) secondary field deviation respect to that produced by the gradient coils measured on function of the frequency and coil track width. The dotted-lines are the shielding ratio and magnetic field deviation produced by filamentary coils.

Next we investigated the tendency of magnetic field spherical harmonics amplitude produced by the eddy currents induced in the cryostat when the coil track width increases from 1 mm to 30 mm and frequency changes from 100 Hz to 10 kHz. Figure 5.13e-f describes the behaviour of the average power dissipation on warm bore and the cold shield of the cryostat. The real part of the amplitude of the field harmonic G_x produced by the split cryostat clearly has a minimum value around 1 kHz. This corroborates that the coils were designed to produce a minimal strength secondary magnetic field with the same spatial variation to that produced by the coil at the target frequency of 1 kHz. We also note that field asymmetries along the *z*-axis tend to disappear at higher frequencies regardless the track width. The field harmonic Z2X produces a minimal value around 1 kHz as the coil was designed to produce a small and controlled secondary field with the same linear behaviour as that of the of the primary field.

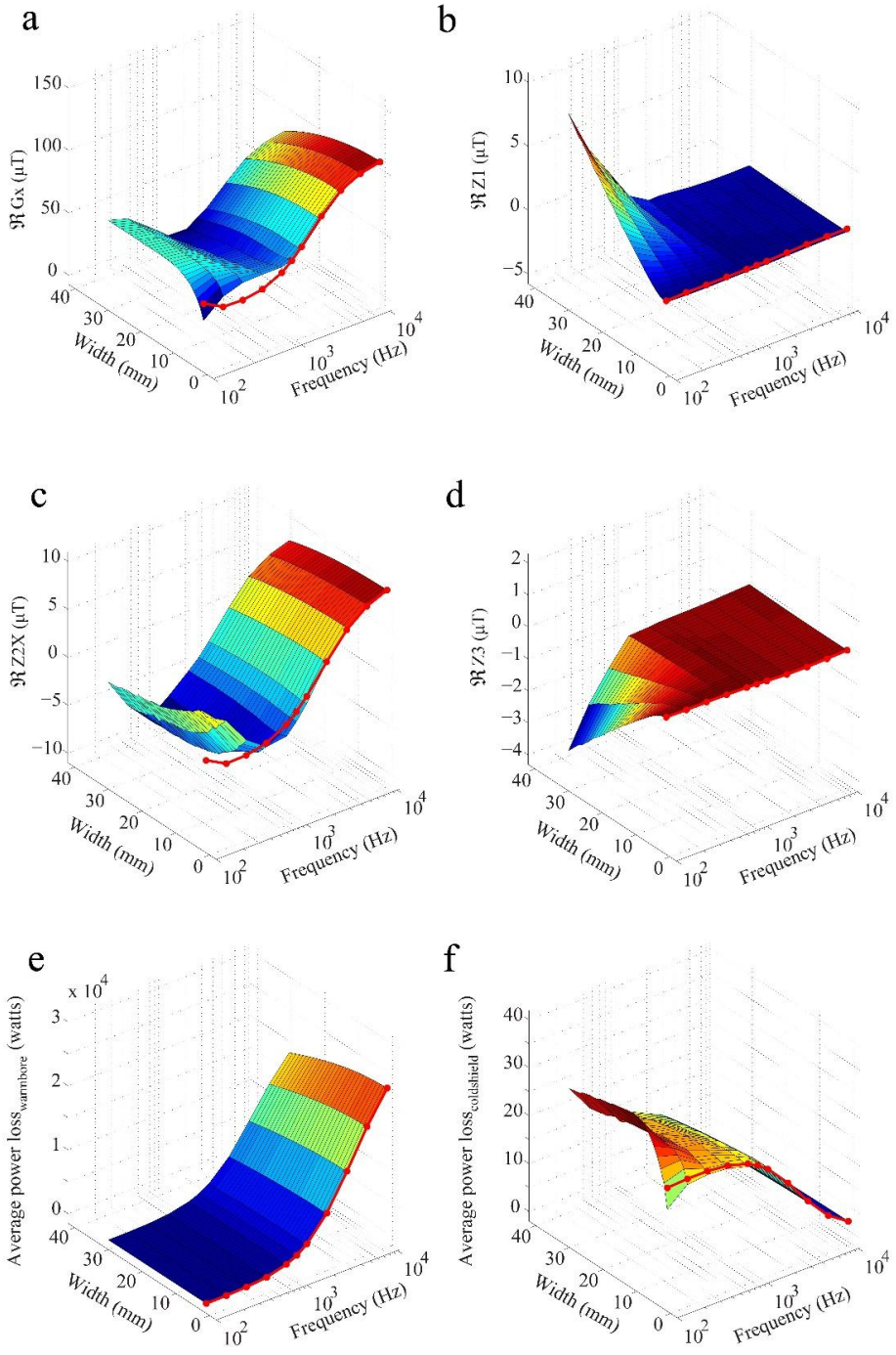

Figure 5.13 Real part of the field Spherical harmonics amplitude produced in the DSV by eddy currents and power loss induced in the cryostat, (a) G_x, (b) Z1, (c) Z2X, (d) Z3, (e) average power loss generated in the warm bore and (f) cold shield of the split cryostat. The dotted-line represents the field spherical harmonics amplitude and power loss when the coil is approximated to filamentary wires.

Wider tracks slightly contribute to reduce the power loss at high frequencies as the coil itself (particularly the shielding coil) may act as a passive shield and as the frequency increases less field leaks outside the warm bore therefore less power is induced in the cold shield (see Figure 5.13e-f)

The results illustrated in Figure 5.10-7 were performed with and without the cryostat in order to study the influence of the surrounding structure over the coil parameters such as FoM, η^2/R, resistance, inductance and field harmonics. We deduce that there is no significant influence of the cryostat on the aforementioned parameters for this set of coils.

The coil performance and generated spherical harmonics produced by the *x*-gradient coils agree very well with the parameters obtained with the filamentary coils for narrow coil track widths. Shielding ratio, secondary field deviation, spherical harmonics induced in the cryostat due to the coupling with the filamentary coils tend to agree with those parameters calculated when the coil is simulated with narrow tracks. However, the result diverges as the coil track width is increased.

The results produced by the *x*-gradient coil in this investigation are similar to that registered by the split *z*-gradient coil but at different scales.

5.3.3 Conclusion

In this section, the MIM was extended to study the influence of the track width and the frequency over parameters such as FoM, η^2/R, resistance, inductance, field harmonics produced by the coil and cryostat; shielding ratio, secondary field deviation from primary field and power loss induced in the cryostat. These parameters were studied in a set of 30 split *x*-gradient coils. The extended MIM was experimentally validated; the suitability and accuracy of the presented method to investigate the skin and proximity effect in a model coil for frequencies up to 10 kHz was demonstrated.

It was found that the parameters calculated using filamentary coils tend to agree to those parameters evaluated using narrow tracks, however the results diverge when the track width increases. The study presented in this section demonstrate that to produce coils with high FoM, it is advisable to use wider coil tracks as the inductance tends to decrease when the coil track is increased. However, it is important to note that the efficiency η is slightly affected at high frequencies. The parameter η^2/R increases for wider track width; nevertheless the increment of the resistance with the frequency is more accentuated for wider tracks than for narrow tracks. We conclude that rapidly changing current paths shall be avoided, where possible, as an

asymmetric profile of the current density along the track may be produced; this effect is more accentuated for tracks located in high current density areas. Some of the zonal harmonics produced by the coil and the cryostat disappears at high frequencies but in order to mitigate their presence, it is recommended to use narrow tracks rather than wide tracks.

Parameters related to the shielding and eddy currents induced in the cryostat strongly depend on the target frequency for which the coil was designed. The decision about the optimal coil track has to be carefully considered. In future work, to evaluate the thermal property of the designed gradient coils, we will include a temperature analysis which considers the skin and proximity effects of the coil tracks.

6. Cross-talk between gradient coils

As described in previous chapters, it was found that the coil performance is related to the coil track width and imposed frequency because of the skin and proximity effects. Previous study focused on the eddy currents between the coil tracks of an individual gradient coil; however, an MRI scanner usually comprises three sets of gradient coils. When one or more coils are switched on and off rapidly, eddy currents are induced in the surrounding gradient coils. In this chapter, the intra-coil interactions between gradient coils will be studied and the impact of the intra-coil coupling on the gradient coil performance will be investigated.

Section 6.2 in this chapter is largely based on the abstract "Crosstalk between gradient coils" in: Proceedings of the *International Society for Magnetic Resonance in Medicine (ISMRM)*, 24, Singapore, 2016. This section is to investigate cross-talk between conventional gradient coils. Section 6.1 and 6.3 are largely based on the journal article "Intra-coil interactions in split gradient coils in a hybrid MRI–LINAC system" published in the *Journal of Magnetic Resonance* in January, 2016. The research presented in these sections aim to study cross-talk between split gradient coils. Editing has been mainly carried out in the introduction for the best coherence with other chapters.

Publication details

Fangfang Tang, Fabio Freschi, Maurizio Repetto, Feng Liu, Stuart Crozier, Crosstalk between gradient coils, in: *Proceedings of the International Society for Magnetic Resonance in Medicine*, 24, Singapore, 2016.

Manuscript revision history

Submitted to *ISMRM*	11 November 2015
Accept	2 February 2016

Author contributions

Fangfang Tang	Numerical modelling, code implementation, analysis and interpretation, manuscript preparation, experiment implementation

Fabio Freschi	Numerical modelling, code implementation , analysis and interpretation , manuscript reviews , experiment implementation
Maurizio Repetto	Analysis and interpretation, manuscript reviews, experiment implementation
Yaohui Wang	Manuscript reviews
Feng Liu	Analysis and interpretation, manuscript reviews
Stuart Crozier	Analysis and interpretation, manuscript reviews

Publication details

Fangfang Tang, Fabio Freschi, Hector Sanchez Lopez, Maurizio Repetto, Feng Liu, Stuart Crozier, Intra-coil interactions in split gradient coils in a hybrid MRI-LINAC system, *Journal of Magnetic Resonance*, vol. 269, pp. 203-212, 2016.

Manuscript revision history

Submitted to *Journal of Magnetic Resonance*	5 November 2015
Interim Decision (minor revision)	15 January 2016
Available online	28 January 2016

Author contributions

Fangfang Tang	Numerical modelling, code implementation, analysis and interpretation, manuscript preparation
Fabio Freschi	Numerical modelling, code implementation, analysis and interpretation, manuscript reviews
Hector Sanchez Lopez	Numerical modelling, analysis and interpretation, manuscript reviews

Maurizio Repetto	Analysis and interpretation, manuscript reviews
Feng Liu	Analysis and interpretation, manuscript reviews
Stuart Crozier	Analysis and interpretation, manuscript reviews

6.1 Introduction

During the gradient coil design process, each coil is usually designed without consideration of the inductive interactions between coils. To reduce the heating problems, wide conductors are often used. However, the wide windings and coil tracks lead to intra-coil eddy currents which may lead to artefacts during MR imaging [139]. To reduce eddy currents, it is essential to consider all the possible sources in an MRI system. There are a large number of conducting structures around the gradient coils [140]. The deleterious effects of eddy currents on the cryostat of an MRI system have been investigated and several methods have been developed to mitigate them as described in Section 2.4.5 [98, 141]. Unfortunately, the cryostat is not the only conductor surrounding the gradient coils. To further overcome the eddy current effects, it is important to consider the intra-coil interactions — eddy currents created by the energized coil in its surrounding coils [139].

To study the electromagnetic coupling between coil windings, a dedicated mathematical model was developed [16], but in Kroot et. al.'s work, only the current distribution in strips and islands were studied, but the impact of intra-coil eddy currents in the transverse and longitudinal coils were not fully investigated. In early patents, engineers attempted to devise engineering solutions to reduce intra-coil eddy currents [139, 142]. For example, to minimize intra-coil coupling and heating, Morich et. al. proposed to vary the width of cut lines and to segment or remove the islands between cut lines [142]. Richard et. al. described an approach to laminate the coil conductor along the thickness and track width direction to reduce intra-coil interactions [139] and Kinanen et. al used narrow, radially oriented slots in ferromagnetic layers before laminations, which could reduce the conduction of the magnetic flux in a vertical, permanent MR imager with two opposite iron core pole pieces [143]. Ham and Konijn proposed to provide a conductive element close to at least one of the gradient coils to compensate intra-coil eddy currents [144]. In these patents, however, the engineering proposals were devised without detailed analysis of intra-coil eddy currents. As demonstrated in this study, it is necessary to conduct a comprehensive investigation towards further reduction of eddy current cross-talk in MRI.

It is expected that the intra-coil eddy currents problem will be more accentuated in fast sequences, such as EPI or TurboSE used in an MRI scanner [145]. This creates additional sources of undesired eddy currents on top of those generated in the cryostat due to practically imperfect shielding [16]. In this work, we conduct a detailed analysis of inductive coupling between gradient coils, and in particular, seek to provide a comprehensive description of the intra-coil interactions in a conventional MRI scanner and an MRI-LINAC system. Moreover, we investigate the relationship between the coil track width and intra-coil eddy currents. Our aim is to explore the impact that inductive coupling between split gradient coils has on power dissipation, coil performance and gradient field linearity.

6.2 Conventional coils

6.2.1 Methodology

A series of gradient coils with different track widths was designed [99]. The maximum track widths of transverse coils varied from 10 to 40 mm with a step of 2 mm and the *z*-coil had a fixed track width of 6 mm. All the coils were designed with a cold shield made of aluminium to produce a maximum gradient strength G_0 = 30 mT/m in a 50×50×40 cm ROI. The maximum field error was ±5% for all the coils. Between tracks was a minimum gap of 1 mm.

Table 6.1 lists the properties of the coils and cryostat, and Figure 6.1a presents the configuration of the gradient coils. The electromagnetic analysis was based on a multilayer integral method [108]. A set of simulations was defined by changing the track width of the transverse coils (Figure 6.2b shows the mesh of a passive *y*-coil). In this work, the *x*-coil was driven by a current at a frequency 1 kHz, and the *y* and *z* coils were un-energised (passive coils). Performance figures were compared between the active coil (energised coil) with surrounding coils and the isolated coil. It was assumed that an isolated coil was not surrounded by neighbouring coils. This allows us to study the impacts the surrounding coils have on the active coil's performance.

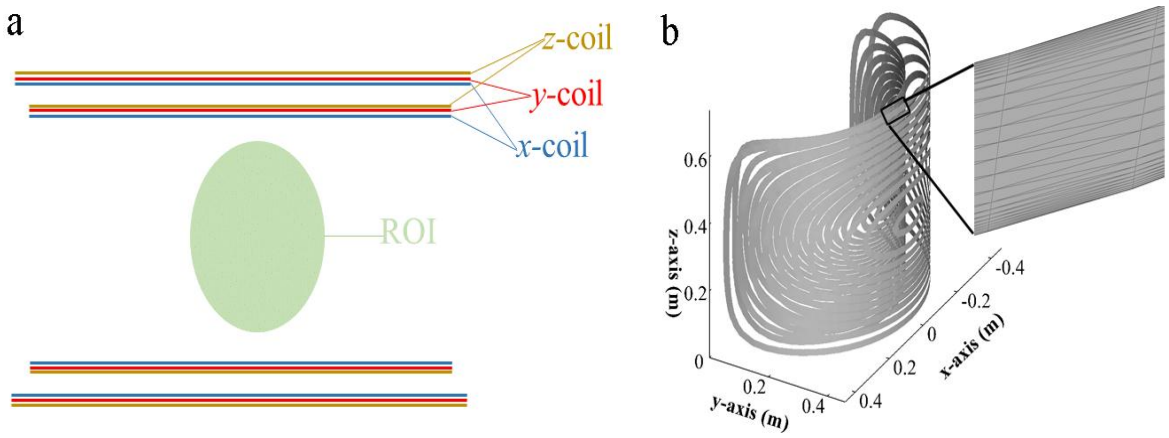

Figure 6.1 (a) the configuration of the conventional gradient coils, (b) 1/4 of the *y*-gradient coil.

Table 6.1 Properties of the gradient coils and cold shield

	x-coil	*y*-coil	*z*-coil	Cold shield
Material	copper	copper	copper	aluminium
Conductivity (MS/m)	59.5	59.5	59.5	208
Thickness (mm)	2	2	2	4
Inner radius (cm)	33.95	34.49	35.21	45.3
Outer radius (cm)	41.47	41.79	40.24	N.A
Overall length (cm)	126	126	126	137

6.2.2 Results and discussion

Figure 6.2a and b describe the induced current density distribution in the passive *y*-coil and cold shield. The transverse coils have a maximum track width of 40 mm. The current density distribution in the passive *y*-coil is much higher than that in the cold shield, and the current density mainly accumulates in the right middle section of the passive *y*-coil. Figure 6.2c compares the real part of the magnetic field along the *x*-axis across the ROI induced by the eddy currents in the passive coils and the cold shield. We can see that the field produced by the passive coils is stronger and more nonlinear than that of cold shield.

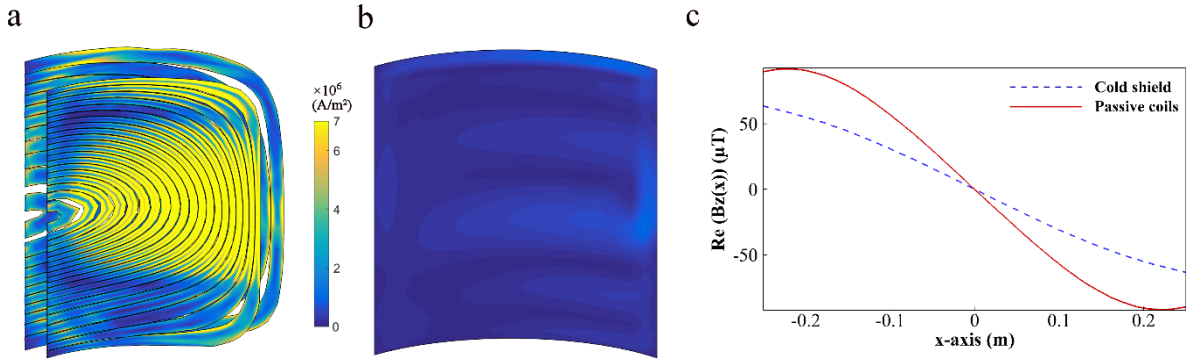

Figure 6.2 Eddy current density, (a) in the passive *y*-coil when the *x*-coil is energised (1/8 of the *y*-coil), (b) in the cryostat when the *x*-coil is active, (c) real part of magnetic field generated by eddy currents induced by the cryostat and the passive *y*, *z* coils (whole coil).

Figure 6.3 presents a significant difference in coil performance between the isolated *x*-coil and the active *x*-coil with surrounding *y* and *z*-coils. The difference increases rapidly with the track width ranging from 10 to 20 mm and keeps relatively stable for track widths from 20 to 40 mm. The total power loss dissipated by *x*, *y* and *z* coils reaches a local minimum value of 20.9 kW at track widths of 14 and 16 mm. The resistance reaches a minimum at a track width of 14 mm. The inductance and coil efficiency decrease with the track width. The FoM and η^2/R have peak values at a track width of 14 mm. The η^2/R of the coil with a track width of 14 mm is 10.1% larger than for a track width of 10 mm and 4% larger than for a track width of 20 mm.

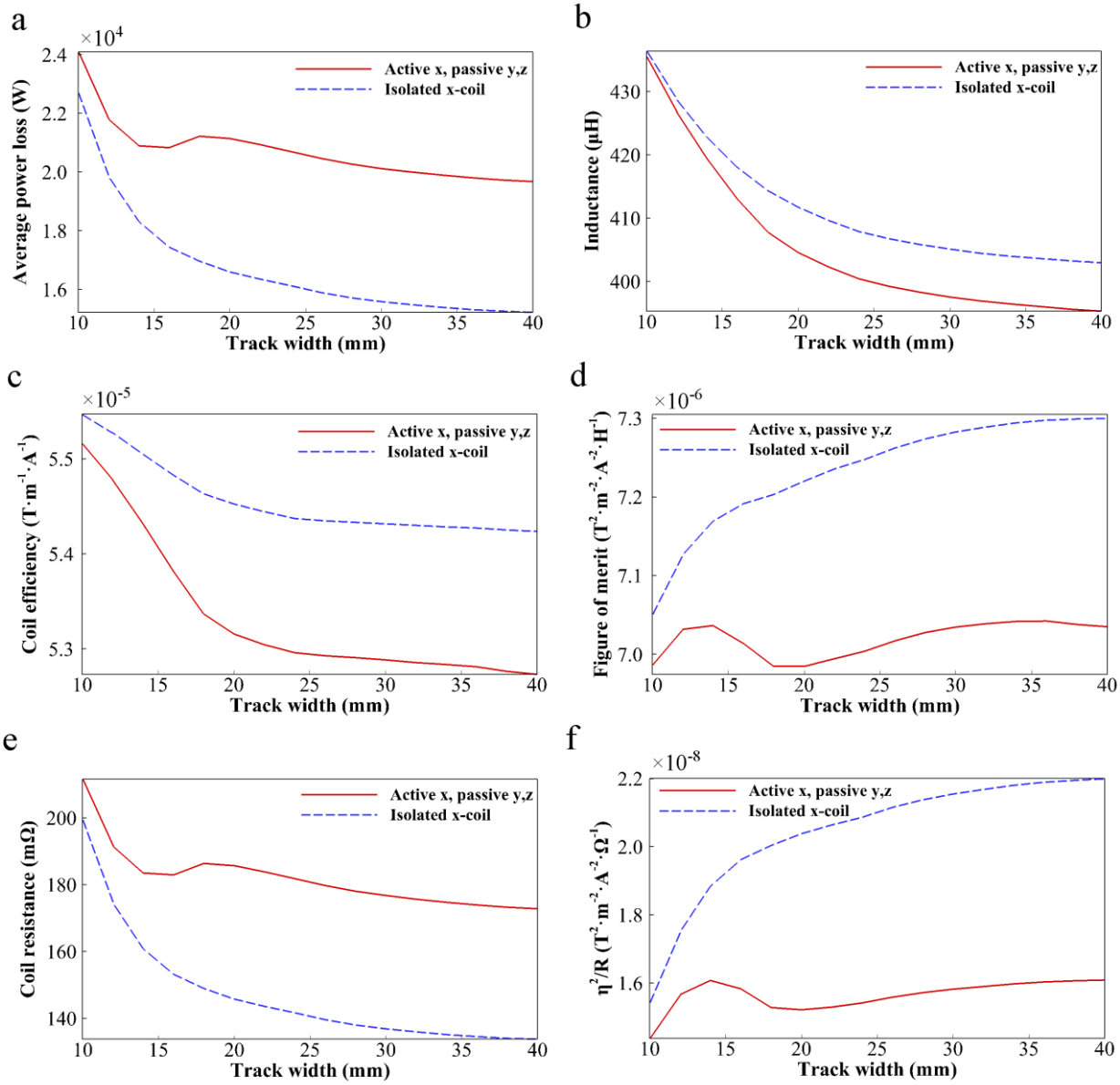

Figure 6.3 Coil performance comparison between active *x*-coil considering passive *y*, *z* coils and isolated *x*-coil, (a) average power loss, (b) inductance, (c) coil efficiency, (d) figure of merit, (e) resistance. (f) η^2/R.

6.2.3 Conclusion

The surrounding passive coils dissipate more eddy currents than the cold wall does. The eddy currents mainly concentrate in the part overlapping with the "eye" of the active *x*-coil because of the higher local current density in this region [16]. Despite the fact inductance has been slightly reduced, the eddy currents in the passive coils lead to more power loss, lower efficiency, lower FoM and η^2/R as well as a larger

secondary field, all of which are effects which should be mitigated as much as possible. From this study, we found that the total power loss, coil resistance, FoM and η^2/R were of minimum values at a track width of 14 mm, and that a coil with a track width of 14 mm has a relative high efficiency. Therefore, track widths around 14 mm are recommended to use in the design of a conventional transverse coil. It is hoped that this intra-gradient coil interaction study will be useful for future gradient coil design and analysis.

6.3 Split gradient coils

6.3.1 Methodology

6.3.1.1 Gradient coils models

In order to study the inductive coupling between split gradient coils in an MRI- LINAC system, we designed a series of split, whole-body coils including *x*, *y* and *z* coils. All coils were designed using the equivalent magnetisation current method [99]. In our numerical model, the coils were driven with a sinusoidal current at 1 kHz to produce a maximum gradient strength $G_0 = 10$ mT/m within a 300 mm DSV. All coils were constrained to produce a 5% maximal deviation from the linear target field specified in the DSV. The gap width between conductors was set to 1 mm and a copper sheet thickness of 2 mm was chosen for the primary and shield coils, respectively. The parameters for designing the coils are shown in Table 6.2, and Figure 6.1a shows a transverse gradient coil used in this study.

Table 6.2 Properties of the designed gradient coils

	x-coil	*y*-coil	*z*-coil
Material	copper	copper	copper
Conductivity (MS/m)	59.5	59.5	59.5
Thickness (mm)	2	2	2
Inner radius (cm)	31.2	31.7	32.4
Outer radius (cm)	40.5	40.1	39.4
Half length (cm)	69.78	69.08	68.05
Gap size (cm)	50.45	51.85	53.9

The coils were designed with a split cold shield made of aluminium and the stored magnetic energy of the coil-cryostat system was minimized in the design process [128]. Table 6.3 shows the cryostat

parameters. The resulting shielding ratio was 4% for all coils. We considered a realistic main magnetic field profile B_0 (1 T) to balance the force and torque of each half coil.

Table 6.3 Properties of the cryostat

Material	Conductivity (MS/m)	Thickness (mm)	Radius (cm)	Length (cm)	Flange Radial Length (cm)	Gap Size (cm)
Aluminum	208	4	43.5	221.5	58.2	55.3

A series of gradient coils, that included 16 split whole-body *x* and *y* gradient coils with different track widths, were designed to study the intra-coil eddy currents due to different track widths. The maximum track width of the *x* and *y* coils varied from 10 mm to 40 mm with an increment of 2 mm. The *x* and *y* coil always had the same track width in simulations. The *z*-coil was designed to a fixed width of 6 mm, since the *z*-coil is usually designed with narrow wires industrially. Figure 6.4b presents the assembly of the *x*, *y* and *z* gradient coils and Table 6.4 summarizes the main characteristics of the coils, where the coil track width is 40 mm for both *x* and *y* coils.

Table 6.4 Main characteristics of the gradient coils

	x-coil	*y*-coil	*z*-coil
Inductance (μH)	89.14	74.37	106.67
Resistance (mΩ)	37.38	21.62	134.20
Cryostat Power Loss (W)	3.76	4.15	2.62
Driven Current (A)	528.27	601.32	401.94

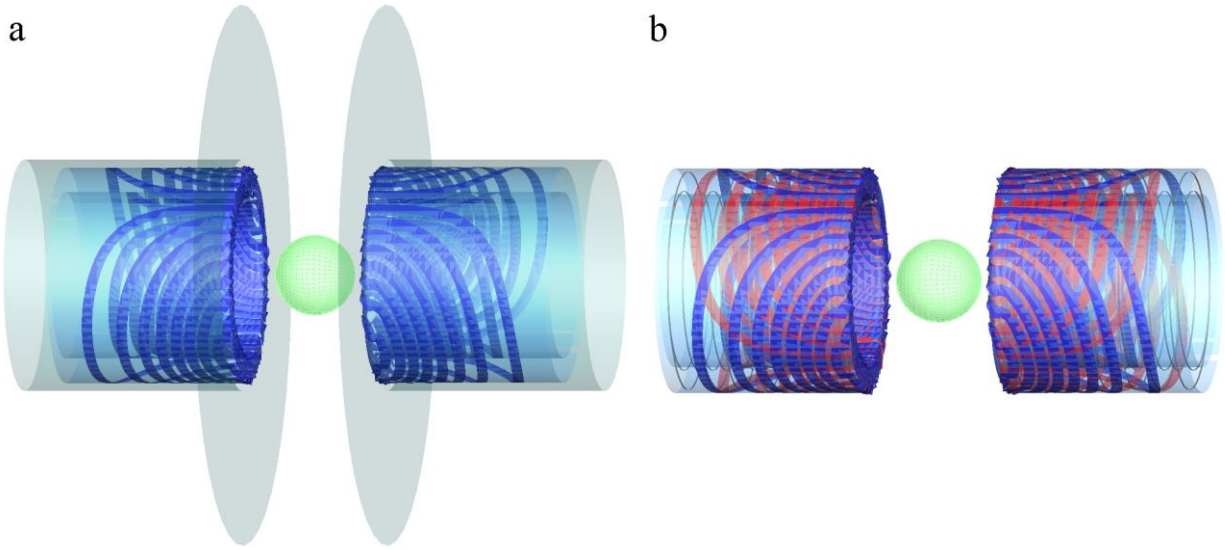

Figure 6.4 (a) example of *x*-gradient coil, (b) *x*, *y* and *z*-gradient coils assembly.

6.3.1.2 Eddy currents simulation

The extended multi-layer integral method (MIM) was applied to study the eddy currents in the surrounding passive coils due to the active *x*-coil [16]. The MIM is effective to study the skin and proximity effects of gradient coil conductors and the inductive interactions between the gradient coils and the surrounding conductors [16]. This method is based on the definition of a stream function [134] which is discretised on a triangular surface mesh. The stream function is interpolated using nodal basis functions.

In order to obtain an accurate solution by considering the skin and proximity effects, the coil tracks need to be finely meshed along the conductor width [16]. However, in our study we did not mesh the conductor through the thickness (normal direction). Meshing the coil tracks introduces a considerable computing burden. With the consideration of the skin effect and non-uniform current distribution across the track width, the calculation of the effective resistance in (3) is modified as [146]:

$$\mathbf{R} = k\mathbf{R}_{\mathbf{DC}} \tag{6.1}$$

Where $\mathbf{R}_{\mathbf{DC}}$ is the DC resistance, and k is the correction factor associated with skin factor, which can be calculated as [146]:

$$k = \frac{t}{2\delta}\frac{\sinh\left(\frac{t}{\delta}\right)+\sin\left(\frac{t}{\delta}\right)}{\cosh\left(\frac{t}{\delta}\right)-cos\left(\frac{t}{\delta}\right)} \tag{6.2}$$

Where δ is skin depth.

To further improve the computing efficiency and reduce memory consumption, in this work, we took advantage of the *x*, *y* and *z* symmetries of the gradient coil pattern, thus only 1/8 of the tracks were simulated. The *x*-coil was driven by a current, *y* and *z* coils were un-energized to investigate intra-coil eddy currents. Eddy currents in the passive coils were calculated for coils with different track widths at different frequencies. The parameters such as average power loss and harmonics generated by the coils were investigated to compare the eddy current effects generated by coils with different track widths.

6.3.2 Results

6.3.2.1 Eddy currents in passive coils

One eighth of the coil assembly (*x y* and *z* gradient coils) was discretised to 40,000 nodes and 12 GB memory was required to model the coils. The transverse coils had a maximum track width of 40 mm and the *z*-coil had a fixed track width of 6 mm. The typical operating frequency of 1 kHz was considered. The computational time was 38 minutes for the matrix assembly and 28 minutes for finding the eddy current solution, using a workstation equipped with two Intel Xeon six-core X5650 at 2.66 GHz and 128 GB of RAM.

Figure 6.5a describes the current density profiles in 1/8 in the passive *y*-gradient coil when the *x*-coil is active. This shows that high current density is induced near the central gap (see bottom of Figure 6.5a) and in the tracks overlapping with the active *x*-coil (the region with yellow edges). The current density in the passive *y*-coil is much higher than the cold shield (Figure 6.5b).

The magnetic fields generated by the eddy currents over the cold shield and adjacent passive *y* and *z* coils were calculated. Figure 6.5(c) shows the real part of B_z field profile in the DSV along the *x*-axis. From this figure, it can be seen that the eddy-current-induced magnetic field in the passive coils is much larger than that produced by the cold shield, which is around 5 times. Thus, to ensure the gradient field linearity, eddy currents in the passive coils need to be investigated in both the system design and imaging phases.

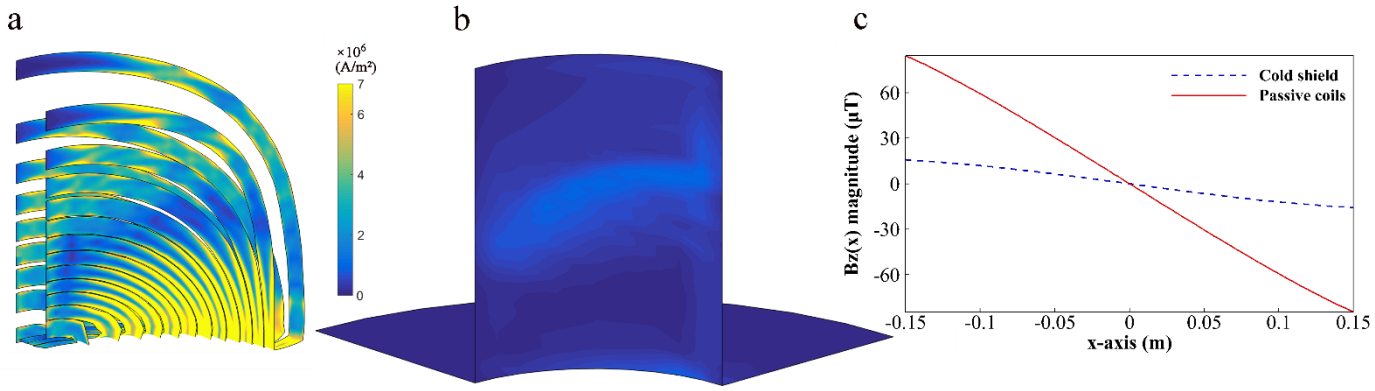

Figure 6.5 (a) eddy current density in the passive *y*-coil when the *x*-coil is active, (1/8 of the *y*-gradient coil is displayed.) (b) eddy current density in the cold shield when the *x*-coil is active, (1/8 of the cold shield is displayed.) (c) real part of magnetic field generated by eddy currents induced by the cold shield and the passive *y*, *z* coils (whole coil).

6.3.2.2 Intra-coil inductive interactions with changes of track width

Figure 6.6 shows the relationship between the power loss and coil track width in the context of intra-coil interactions. Figure 6.6a shows that, when *x*-coil is active, the power loss in the passive *y*-coil increases with track width, even though coils with wider tracks have smaller resistance. This indicates that higher eddy currents are induced in wider tracks, which is especially noticeable for track widths larger than 26 mm. Even at a frequency smaller than 1 kHz, the effect is already significant. Figure 6.6a demonstrates that the power loss dissipated by the passive *z*-coil is negligible when compared to the passive *y*-coil. The total average power loss produced in the *x*, *y*, *z* coils due to the active *x*-coil is shown in Figure 6.6c. It is interesting to see that, at frequencies higher than 1 kHz, the total power loss decreases to a minimal value around a track width of 24 mm. The total power in the coils with narrow tracks (around 10 mm) has a rapid increase with frequency, although the power loss in the passive coils rises steadily. Because more power loss is produced in the active coil with narrow tracks at high frequencies [16]. The total power loss increases with the frequency for wide track widths (30 mm to 40 mm) as well, but the reason here is that wider tracks produce more power in the active coil due to skin and proximity effects, meanwhile passive coils with wider tracks, generate more eddy currents and hence more total power loss is dissipated [16].

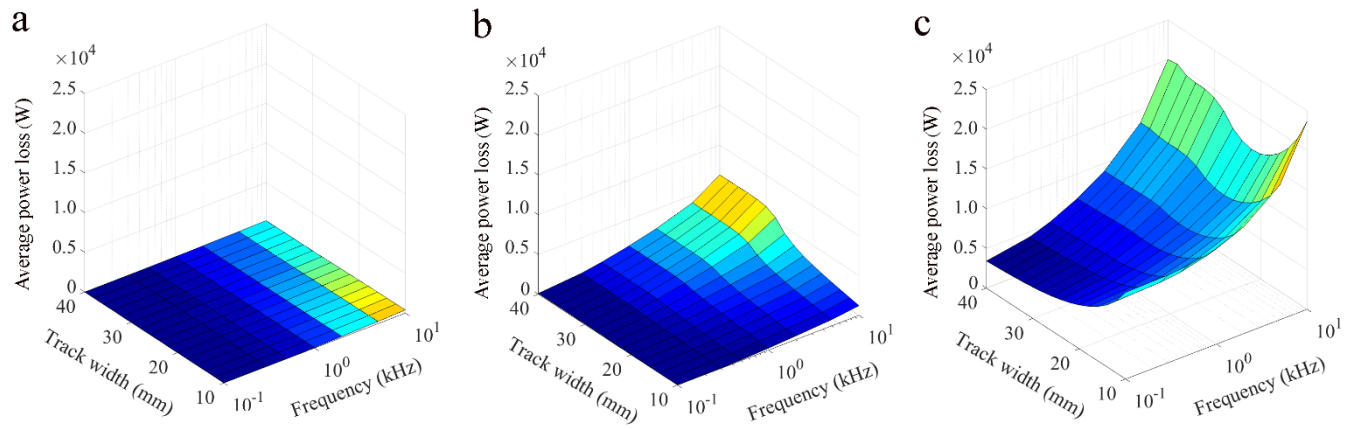

Figure 6.6 Average power loss when *x*-coil is active and *y*, *z* coils are passive, (a) passive *z*-coil, (b) passive *y*-coil, (c) total power loss in *x*, *y*, *z* coils.

Conventionally, coils are designed to dissipate power by using wider track widths without the consideration of the surrounding passive coils. Owing to strong inductive coupling effects shown here, the influence of the neighbouring gradient coils has to be taken into account in the design process and in the analysis of gradient coil performance. This is because wider tracks produce more power in both active coils, due to skin and proximity effects, and passive coils due to intra-coil eddy currents. In order to reduce the power loss dissipation, a track width of 24 mm is recommended to design a split gradient coil.

The intra-coil interactions impact the gradient coil performance, as shown in Figure 6.7. Here we studied the performance of the isolated *x*-coil, as well as the active *x*-coil surrounded by the passive *y*, *z* coils. We assumed that an isolated gradient coil was not surrounded by any magnetic field source (no other gradient coils were wrapped around the *x*-coil). The difference of the active *x*-coil (operating at a frequency of 1 kHz) with surrounded passive coils and the isolated *x*-coil is compared to study the intra-coil eddy current effects.

When the track width is 24 mm, the total power loss reduces to a minimum value of 7.115 kW (Figure 6.7a). In presence of the passive coils, the inductance is smaller than the isolated coil, and the difference increases with the track width (Figure 6.7b). The efficiency of the active *x*-coil with the neighbouring passive coils reduces faster than the isolated *x*-coil for wider tracks (Figure 6.7c). The efficiency of the active *x*-coil with the passive *y*, *z* coils reduces by around 2.2% for a track width of 20 mm and 3.6% for a track width of 24 mm when comparing the case of an isolated *x*-coil. The figure of merit (FoM, defined as η^2/L, where η is efficiency and L is inductance) reaches the peak value at a track width of 20 mm, and then reduces to a minimum at 30 mm, because of the decreased efficiency and inductance with track width. Another parameter, η^2/R (the coil efficiency η normalized by resistance R) is also useful for the evaluation

of coil performance. In general, higher η^2/R values indicates better coil performance. Accordingly, as shown in Figure 6.7f, the coil performance at a track width of 22 mm is the best in terms of the η^2/R value.

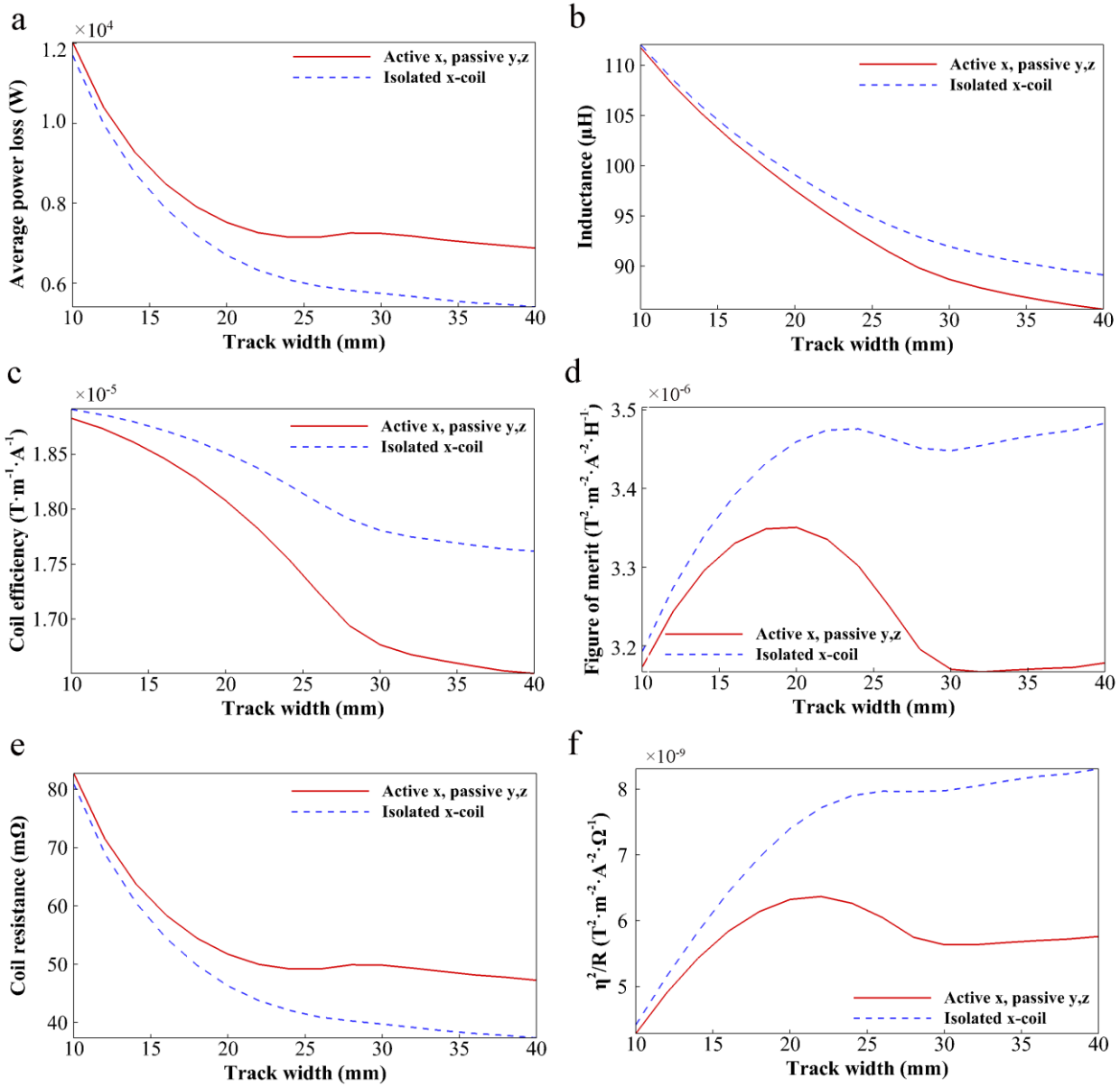

Figure 6.7 Coil performance comparison between active *x*-coil considering passive *y*, *z* coils and isolated *x*-coil, (a) average power loss, (b) inductance, (c) coil efficiency, (d) figure of merit, (e) coil resistance, (f) η^2/R.

The inductance is reduced by using coils with wider tracks, but this deteriorates the average power loss, coil efficiency, FoM, η^2/R because of the increased eddy currents. The difference of the parameters with and without passive coils also increases with track width. The power loss reduces to a minimum at a track width of 24 mm, but is comparatively stable for values in the range of 20 mm to 40 mm. The efficiency

decreases with the track width and the FoM has the maximum value at a track width of 20 mm, while η^2/R reaches the maximum at a track width of 24 mm. Synthetically, taking the power, efficiency, η^2/R and FoM into account, track widths in the range between 20 mm to 24 mm are recommended to use for the design of split transverse coils. This is because narrow tracks smaller than 24 mm dissipate more power have lower FoM and η^2/R, and coils with tracks wider than 24 mm have lower efficiency, FoM and η^2/R. We also note that the evaluation of the gradient performance needs to consider the intra-coil interactions, otherwise it is inaccurate to calculate coil efficiency and FoM.

In this study, we also evaluate the deleterious effects of eddy currents on the magnetic field in the DSV. The designed *x*-coil produces two main magnetic field harmonics: G_x, $B_z \approx r\sin\theta\cos\phi$, and Z2X, $B_z \approx r^3\sin\theta\cos\phi\left(5\cos 2\theta - 1\right)$, where $\left(r, \theta, \phi\right)$ is the position of the target point [147]. Gx is the amplitude of the *z*-component of the magnetic field along the *x*-direction and Z2X is the amplitude of the first non-linear term after Gx [147]. The field harmonics induced by the isolated coil were compared with that generated by the active and passive coils.

As shown in Figure 6.8, the harmonics Gx,Z2X and the ratio of Z2X/Gx produced by the active *x*-coil and passive coils are higher than that of an isolated *x*-coil, and the difference increases for wider tracks. This indicates that the harmonics Gx and Z2X produced by the eddy currents in passive coils increase with the track width and the polarity is opposite to that produced by the active *x*-coil. Since Z2X produced by the *x*-coil and surrounding coils are smaller than the isolated *x*-coil, the non-linear terms of field inhomogeneity produced by the active *x*-gradient coil were reduced by the eddy currents in the passive coils. Z2X is reduced by 3.32%, 6.96% and 9.91% for track widths of 20 mm, 26 mm and 30 mm, respectively. However, at the same time, eddy currents in the passive coils are detrimental to the desired harmonics Gx. Gx is decreased by 2.2%, 4.4% and 5.6% for track widths of 20 mm, 26 mm and 30 mm, respectively. The ratio of Z2X/Gx is improved by the eddy currents in the surrounding coils, because of the faster decreased Z2X. Passive coils with wide tracks seem to shield the DSV from spatial field harmonics. However, the small improvement in the non-linear component of harmonic does not justify the decrease of desired harmonics, additional losses and the reduction of efficiency. In spite of slightly reducing undesired harmonics, this effect is unsustainable and uncontrollable. Our conclusion is therefore that eddy currents should be mitigated as much as possible.

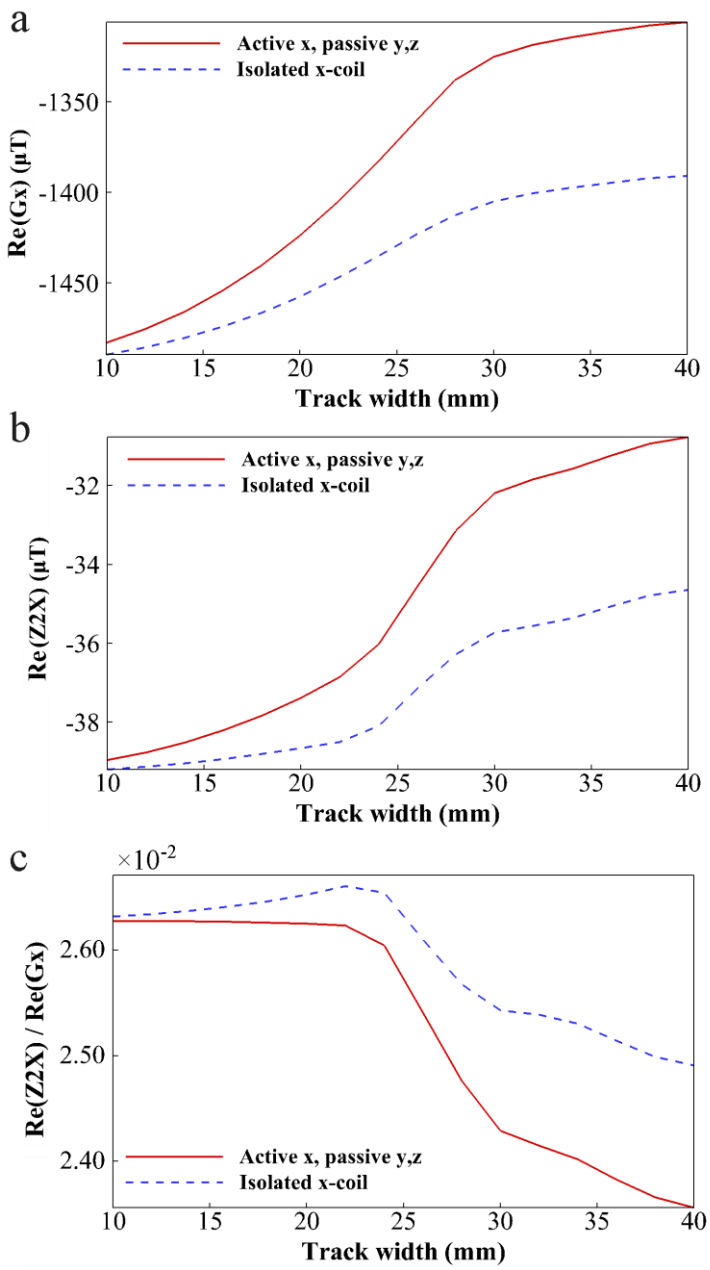

Figure 6.8 The real component of field harmonics amplitude produced by isolated *x*-coil and by active *x*-coil and passive *y, z* coils, (a) Gx, (b) Z2X, (c) Z2X/Gx.

In this investigation, we merely studied the model active *x*-coil and passive *y*, *z* coils. During imaging however, two or more coils may be active in a complex temporal manner so larger intra-coil eddy currents will exist and the gradient coil performance may be more strongly affected.

6.3.3 Conclusion

In this work, we analysed the inductive interactions between *x* ,*y* and z gradient coils in a split MRI-LINAC system. Different driving frequencies and track widths were investigated in terms of the average power loss, coil performance and the amplitude of the field harmonics in the DSV. The study found that: the electromagnetic interaction induced magnetic field at the neighbouring coils is several times larger than that produced by the cold shield and the average power loss in the surrounding passive coils increases with the coil track width. The total power loss reduces to a minimum value at a track width of 24 mm and has a rapid increase with frequency for both wide tracks (30 mm to 40 mm) and narrow tracks around 10 mm. Coil performance, with regard to efficiency FoM and η^2/R, is degraded by the eddy currents in the surrounding coils, especially for coils with wider tracks. The harmonics produced by the passive gradient coils with wider tracks, around 40 mm, are larger than narrower tracks. Based on these findings, we suggest that for the split whole-body gradient coil set described herein, the coil track width should be between 20 mm to 24 mm and that intra-coil eddy currents should, in general, be considered in the gradient coil design process.

7. On the mitigation of cross-talk between gradient coils

In chapter 6, the cross-talk between the gradient coils in terms of frequencies and gradient coil track widths in a conventional and an MRI-LINAC system was studied in detail. It was found that the cross-talk between gradient coils lead to a non-linear gradient field, which should be mitigated as much as possible. For this purpose, lamination was proposed to be applied to the gradient coil track sheets to reduce intra-coil eddy currents. The proposed configuration will be assessed by evaluating the coil performance and comparing it with the performance of the original coil structure without slits.

Section 7.1 and 7.3 in this chapter are largely based on the journal article "Mitigation of Intra-coil Eddy Currents in Split Gradient Coils for a Hybrid MRI-LINAC System" accepted for publication by the *IEEE Transactions on Biomedical Engineering*, 2016. Theses sections aim to mitigate cross-talk between split gradient coils. Editing has been mainly carried out in the introduction for the best coherence with other chapters.

Publication details

Fangfang Tang, Fabio Freschi, Maurizio Repetto, Yu Li, Feng Liu, Stuart Crozier, Mitigation of Intra-coil Eddy Currents in Split Gradient Coils for a Hybrid MRI-LINAC System, *IEEE Transaction on Biomedical Engineering, 2016* (accepted).

Manuscript revision history

Submitted to *IEEE Transaction on Biomedical Engineering*	12 December 2015
Interim decision (major revision)	21 January 2016
Revision submission	03 March 2016
Interim decision (minor revision)	25 April 2016
Revision submission	11 May 2016
Accepted	21 May 2016

Author contributions

Fangfang Tang	Numerical modelling, code implementation, analysis and interpretation, manuscript preparation, experiment implementation
Fabio Freschi	Numerical modelling, code implementation, analysis and interpretation, manuscript reviews, experiment implementation
Maurizio Repetto	Analysis and interpretation, manuscript reviews, experiment implementation
Yu Li	Experiment implementation, manuscript reviews
Feng Liu	Analysis and interpretation, manuscript reviews
Stuart Crozier	Analysis and interpretation, manuscript reviews

7.1 Introduction

The intra-coil eddy currents lead to a non-linear gradient field and thus cause image blurring during MR imaging, which needs to be mitigated as much as possible [122]. To reduce intra-coil eddy currents, litz wires may be used, however they are difficult to configure in transverse split-gradient coils with complex geometries and prove costly to machine into fiberglass tubes [131]. Some other solutions have been previously proposed to reduce the intra-coil effects, for example, by either reducing the coil cross-section, which is effective but causes the Ohmic resistance increase or by varying the conductor cross section only where the eddy currents are stronger [68, 148]. Another solution involves electronic compensation of eddy current effects, which locates the conductive element in close proximity to the gradient coils to compensate for the intra-coil eddy currents in the gradient coil assembly [143]. Lamination is also used as solution and is

usually adopted in the iron core of electrical machines [149, 150]. Lamination is implemented by assembling the magnetic core using thin insulated sheets of electrical steel lying parallel to the magnetic flux density direction. As a consequence, eddy currents can only flow within the thin sheets with a higher resistance in the individual lamination layers, thus reducing Joule loss in the bulk iron core [149]. Following this line of reasoning, in [139], gradient coils are made by composite conductors, which are formed by insulating adjacent layers or strips of thin conductive material. This laminated configuration is capable of minimizing the current flow between each of the conductive layers. Different from the proposal in [139], in today's gradient coil engineering, the coils are usually designed with wide tracks at a thickness of about 2 mm to reduce coil resistance and save radial space. Wide tracks however, will lead to strong intra-coil eddy currents. In [143], Kinanen proposed to use electrically insulated layers and slots to further reduce inductive interactions between coils in open MRI scanners. In [151], Sementchenko used 1 mm width slits extending in the direction of current flow, for the purpose of reducing intra-coil eddy currents caused by the perpendicular flux component to the coil plane in an open MRI system. With an acknowledgement of the above efforts on eddy current reduction by means of coil reconfiguration, there is still a lack of comprehensive analyses of intra-coil interactions and the benefit of slitting the coil tracks in detail. In this research, we will fully investigate these issues through theoretical simulation and experimental validation.

In this work, we propose a novel technique for gradient coil manufacturing that applies the lamination technique on the coil track sheet to moderate the eddy currents caused by the intra-coil effects [18]. Specifically, the coil tracks are slit longitudinally along the direction of current flow. This implies that the cuts have little influence on the current flow when the coil is energized, but can block the return path of the local eddy currents. In this work, we provide a detailed theoretical analysis of the benefit of coil track slits.

7.2 Conventional coils

7.2.1 Methodology

Three gradient coils are involved in a full gradient set, but in this study, the gradient system was simplified to have only transverse *x* and *y* coils without the longitudinal *z*-coil for the purpose of reducing the computational burden. The *x* and *y* coils have the same properties as the coils in

Table 6.1. The maximum track width of the *x* and *y* coils is 30 mm and the other parameters are the same as described in section 6.1.2.

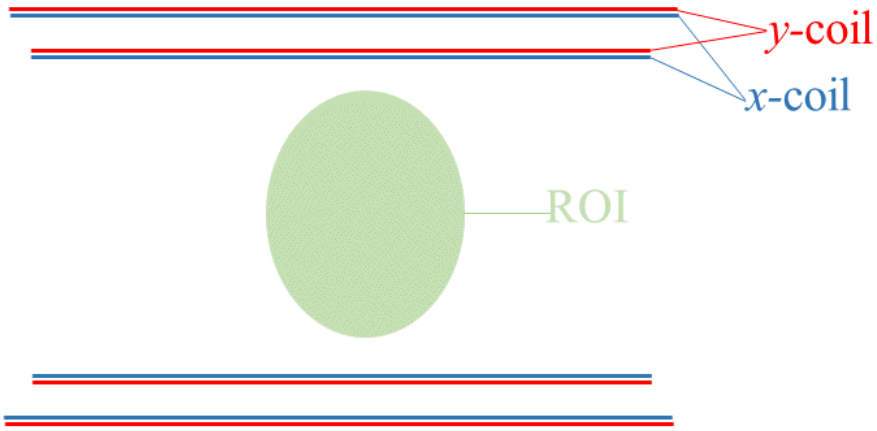

Figure 7.1 The structural configuration of split *x* and *y* coils.

In order to mitigate interactions between gradient coils and maintain coil performance, the coil tracks shown in Figure 7.2a were slit along the direction of the current flow as presented in Figure 7.2b. The sub-tracks (Figure 7.2b) have the same width. The magnetic flux through each sub-track is reduced because of the reduced area, thus mitigating the eddy currents in the surrounding coils. Then the coils were analysed using the MIM [108]. The performance of the coils without and with slits was compared and investigated.

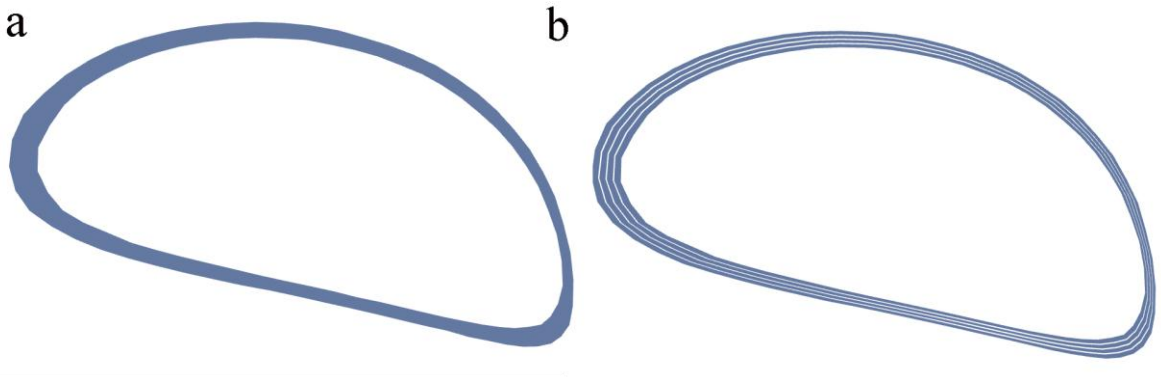

Figure 7.2 Examples of coil track with and without slits, (a) track without slits, (b) track with slits.

7.2.2 Results and discussion

Figure 7.3 compares the current density profile in the passive (un-energised) *y*-coil without slits and with three slits at 1 kHz and 10 kHz. The current density in the passive coil is significantly reduced by the slits (Figure 7.3b) at 1 kHz. Figure 7.3c compares the current density along the red line in Figure 7.3a and b,

where it can be seen that the current density in the passive slit coil is reduced by more than 85% in some areas, and the current density distributes more uniformly in the passive coil with slits. At 10 kHz, slits do not result in an obvious change to the current density in the passive coil except to reduce some peak values (Figure 7.3d–f).

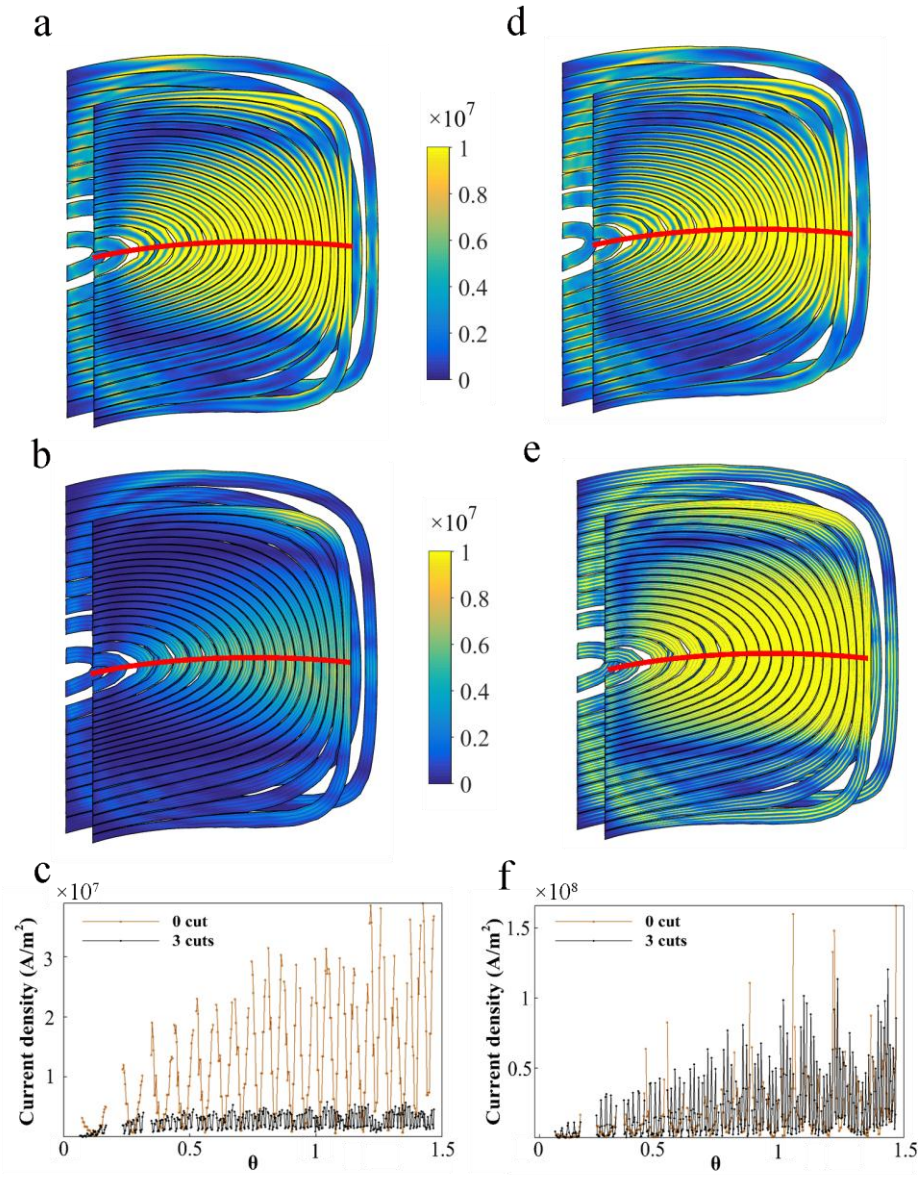

Figure 7.3 Current density in the conventional passive *y*-coil, (a) no cut (f = 1 kHz), (b) three cuts (f = 1 kHz), (c) spatial current density distribution along the red line indicated in Figure 7.3 5a–b, (d) no cut (f = 10 kHz), (e) three cuts (f = 10 kHz), (f) spatial current density distribution along the red line indicated in Figure 7.3 d–e (f = 10 kHz).

The power loss produced by the eddy currents in the passive coil with cuts is largely reduced at low frequency as shown in Figure 7.5. The power dissipated by the passive *y*-coil with one cut and four cuts was reduced by 50% and 90%, respectively, compared to that of the coil without cut.

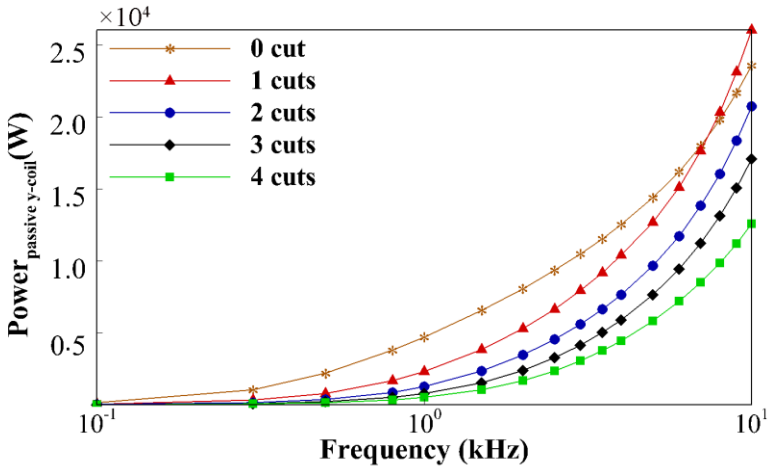

Figure 7.4 Average power loss dissipated by the passive *y*-coil for different numbers of cuts.

Figure 7.5 presents the secondary field produced by the eddy currents in the passive *y*-coil with different numbers of cuts along the *x*-axis (-0.25 to 0.25 m) at $y = z = 0$. The secondary field produced by the intra-coil eddy currents is reduced significantly by the slits, that is a reduction of 20%, 7%, 4%, and 2% for one to four cuts, respectively. This indicates that it is more efficient to use the pre-emphasis method to compensate the field generated by the eddy currents after slitting the coil tracks.

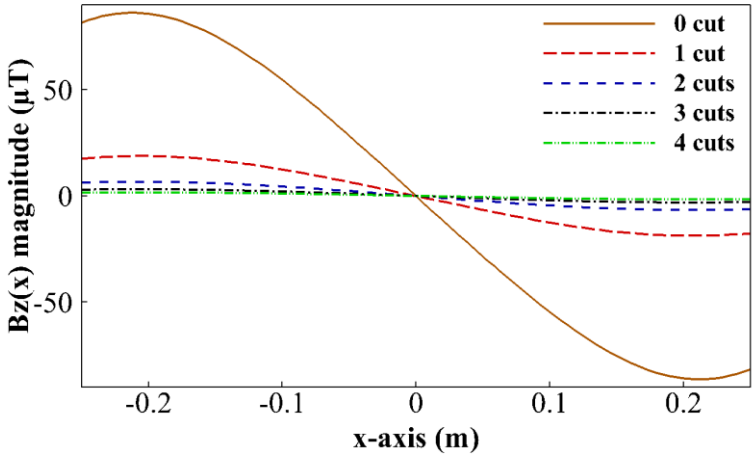

Figure 7.5 Real part of the magnetic field produced by the eddy currents in the passive coil with different numbers of cuts.

Slitting the coil tracks reduces the peak values of the current density in the active *x*-coil as shown in Figure 7.6e and f. However, the current density distribution in the coil tracks with three slits is slightly more uniform than the coils without cut at the parts that overlap with the passive *y*-coil. This is due to the fact that the eddy currents in the passive *y*-coil also generate eddy currents in the active *x*-coil.

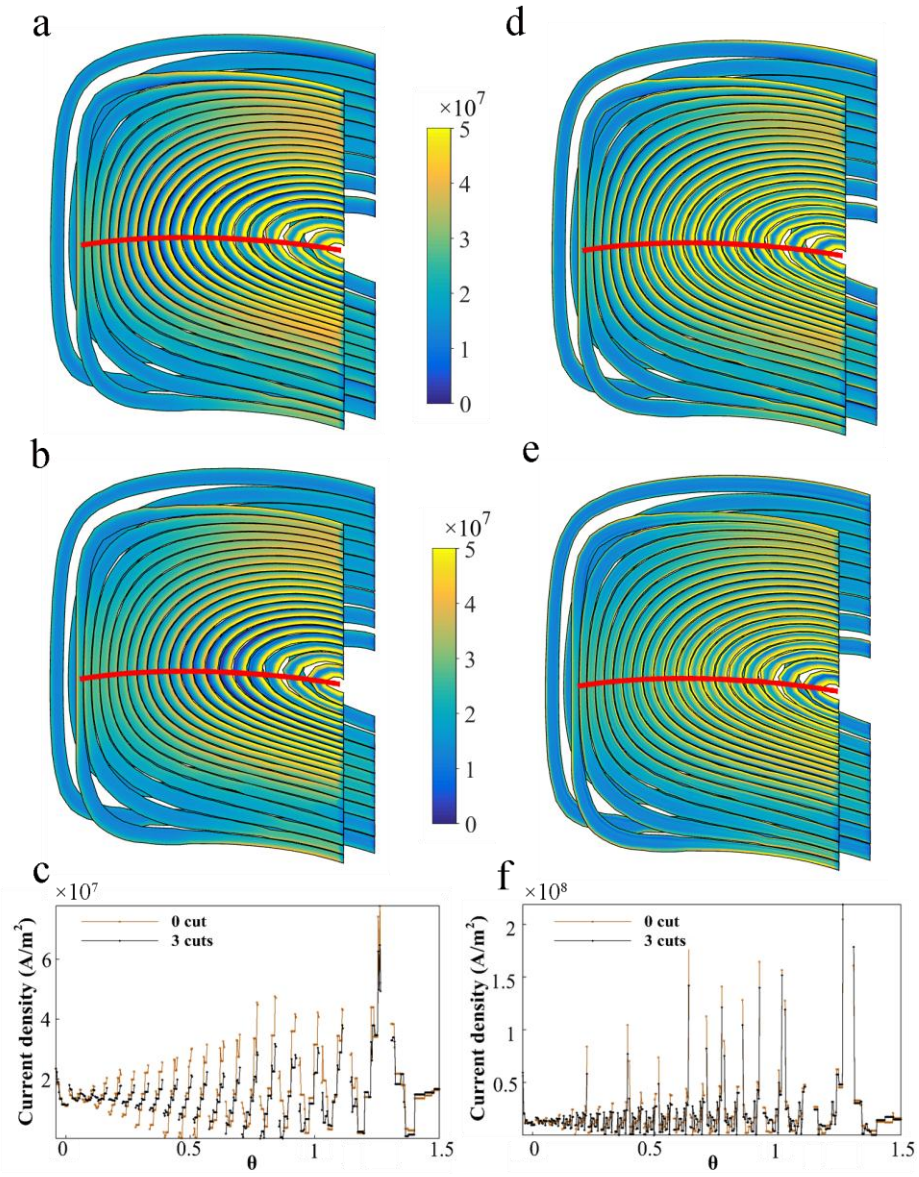

Figure 7.6 Current density in the conventional active *x*-coil, (a) no cut (f = 1 kHz), (b) three cuts (f = 1 kHz), (c) spatial current density distribution along the red line indicated in Figure 7.15 8a–b, (d) no cut (f = 10 kHz), (e) three cuts (f = 10 kHz), (f) spatial current density distribution along the red line indicated in Figure 7.15d–e (f = 10 kHz).

Figure 7.7 illustrates the coil performance of the conventional active *x*-coil taking into account the surrounding passive *y*-coil with different numbers of cuts. The inductance increases after slitting the tracks in the active *x*-coil and the passive *y*-coil. However, the FoM, resistance, η^2/R, power and efficiency are improved by slitting the tracks because of the consequent reduction of the eddy currents in the passive coils. Furthermore, the benefits obtained by slitting the tracks increase with the number of cuts.

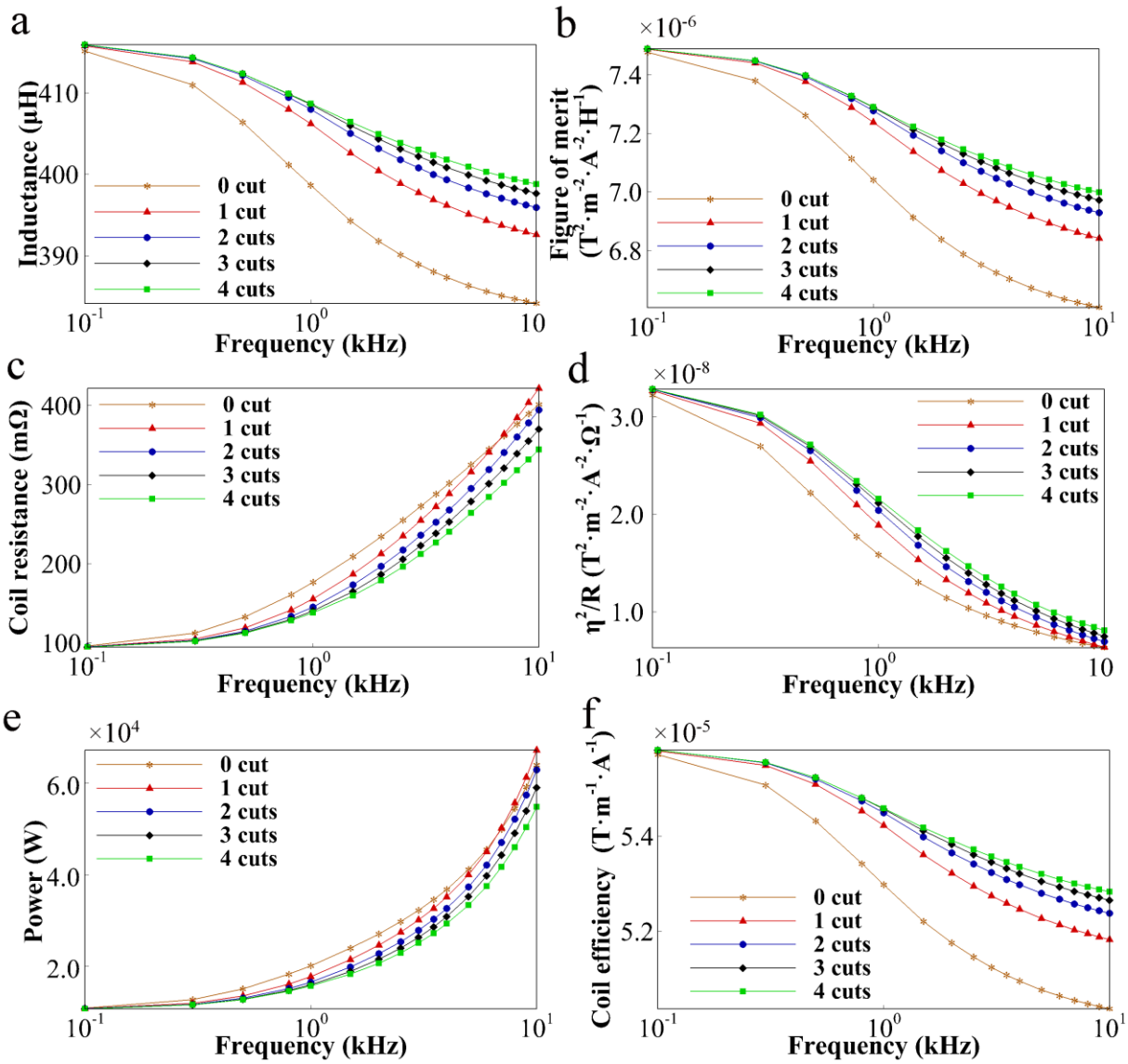

Figure 7.7 The performance of the conventional active *x*-coil considering the passive coil, (a) inductance, (b) resistance, (c) Figure of Merit, (d) η^2/R, (e) average power loss, (f) efficiency.

7.2.3 Conclusion

The eddy currents induced in the passive coil were effectively mitigated by slitting the coil tracks. The power loss dissipated by the passive *y*-coil was significantly reduced at frequencies lower than 7 kHz. The secondary field generated by the coil with four cuts in the coil track is only 2% of that produced by the coil without cut. The coil performance showed a significant improvement after slitting the coil tracks.

7.3 Split gradient coils

7.3.1 Methodology

7.3.1.1 Gradient coil model

A full set of gradient coils consists of *x*, *y* and *z* coils, but in this study, the longitudinal *z*-coil is not involved, because the intra-coil coupling effects are less than those of the transverse coils. The gradient coils were designed to generate a maximum gradient strength G_0 = 10 mT/m in a diameter spherical volume (DSV) with a radius of 30 cm. The coils had a maximum track width of 30 mm and the minimum gap size between the tracks was constrained to 1 mm. The design parameters are shown in Table 7.1 and the coil configurations are shown in Figure 7.8. For a more detailed description of the magnetic structure, please refer to [44].

Table 7.1 Properties of cryostat and gradient coils

	Cryostat	*x*-coil	*y*-coil
Material	Aluminium	Copper	Copper
Conductivity (MS/m)	208	59.5	59.5
Thickness (mm)	4	2	2
Inner radius (cm)	43.5	31.2	31.7
Outer radius (cm)	N.A	40.5	40.1
Flange radial length (cm)	43.5	9.3	8.4
Half length (cm)	83.1	69.78	69.08
Gap size (cm)	55.3	50.45	51.85

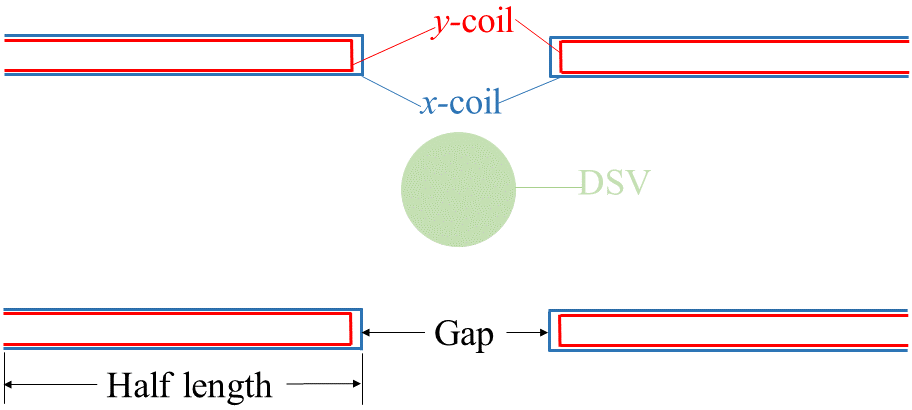

Figure 7.8 The structural configuration of split *x* and *y* coils.

The magnetic energy generated by the cold shield of the cryostat was minimized during the design process of the gradient coils [79]. The gradient field deviation was kept under ±5% and the shielding ratio was constrained to 4% for both *x* and *y* coils [16].

7.3.1.2 Slits and simulations

To minimize the intra-coil eddy currents and avoid a reduction in the active coil performance, the coil tracks were slit along the direction of current flow (Figure 7.9a and b). All the sub-tracks in Figure 7.9b have the same track width. Figure 7.9b outlines the slit copper track, the red arrow indicates the direction of the current flow when the coil is active, while the blue arrows show the eddy currents flow when the coil is passive. For the slit tracks, the area of the individual sub-track is reduced. According to Faraday's law, the magnetic flux through each sub-track is lessened, therefore, the eddy currents can be reduced by the slit structure [152]. Additionally, each individual sub-track exhibits a higher resistance to the induced electro-motive force and, consequently, lower eddy currents. These two effects are synergistic in the reduction of eddy currents in the slit conductors.

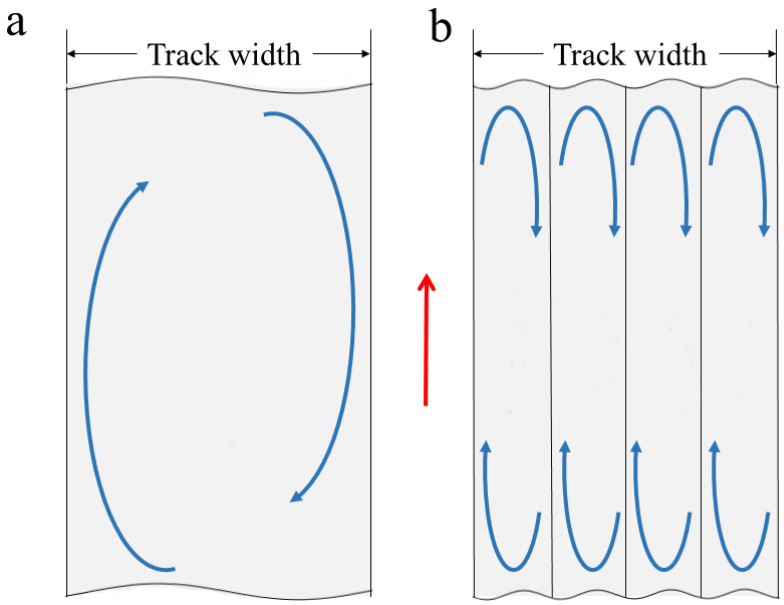

Figure 7.9 Current profile, the red arrow indicates the direction of current flow in the active coil track, the blue arrows show the direction of eddy currents in the passive tracks, (a) track without slits, (b) track with slits.

In this work, we assume that the total driven current is known for the active coil to generate the desired maximum gradient strength, but the detailed current distribution in the tracks is unknown. An extended Multi-layer Integral Method (MIM) was used to study the slit gradient coils [28, 30] and obtain the current distribution information. This method discretises thin conductors with a surface triangular mesh and formulates the current flow problem in terms of the current stream function [30, 31]. The current density in each triangle is obtained by interpolation of the nodal values of the stream function. Each sub-track of the passive coil was meshed following an exponential decay in accordance with the skin and proximity effects in the passive coil.

To determine the best slit strategies, we compared two different cutting schemes, complete cutting and adaptive cutting. In complete cutting, the tracks are cut along the entire track length. In adaptive cutting, only the hot spot regions on the coil tracks are slit. To realize this adaptive cutting, the current density in the un-slit case is first evaluated to find regions of high current density values, and then the track is slit only where the current density is higher than a specified threshold (in this work, the threshold value is set to 5.0 A/mm^2 at a 1 kHz frequency, which corresponds to 5.6% of the maximum current density).

We studied the effect of the numbers of slits (cuts) cross the coil track on eddy current reduction. The *x* and *y* coils were always characterized by the same number of slits (cuts). A driving current with a frequency sweep ranging from 100 Hz to 10 kHz was applied to study the eddy currents in the passive coil and the performance of the active coil considering the passive coil.

7.3.1.3 Experiment validation

An experiment was set up to validate the proposed scheme for its effect on eddy currents. It compared the difference between the slit and un-slit coil tracks. Two spiral coils were made on both sides of printed circuit board (PCB) (Figure 7.10a and b). Each spiral coil had a track width of 2.2 cm and 5 turns. The spiral coils were manufactured in copper with an inner radius of 2 cm, an outer radius of 13.75 cm and a thickness of 0.089 mm, with the distance between the two layers of spiral coils being 0.24 mm. The coils on two sides of the PCB were shifted 4.58 cm to simulate the transverse gradient coil configuration.

An LCR-819 meter (GW INSTEK) was applied to measure the inductance and resistance of the spiral coils. Figure 7.10c shows the experimental set up. The clips of the LCR meter were connected to the copper wires welded to the white circular surfaces. The white circular surfaces were used to connect the spiral coils with the LCR meter or external wires and were silver coated to maintain a good conductivity. The copper wires and the clips were orthogonal to the spiral coils to avoid the coupling effects from the clips and wires. A voltage of 1 V with frequencies in a range sweeping from 100 Hz to 10 kHz was applied to one spiral coil, while the coil on the other side of the PCB was left un-energized. The inductance and resistance of the two sets of spiral coils were measured and compared with the results predicted by the MIM method.

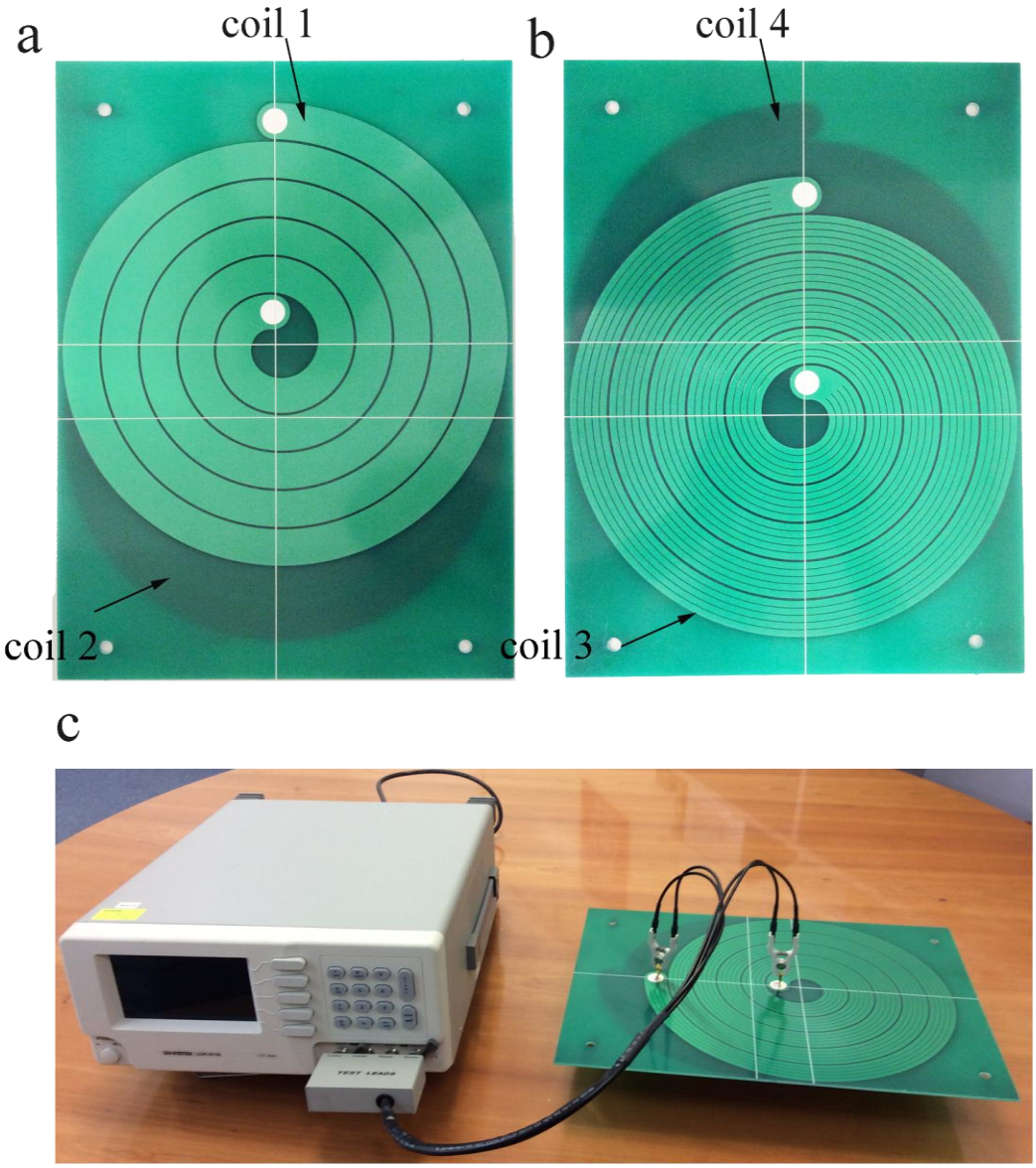

Figure 7.10 Experiment, (a) spiral coils without slits, (b) spiral coils with slits, (c) experimental set up.

7.3.2 Results

7.3.2.1 Experiment result

Figure 7.11 compares the inductance and resistance values obtained from the simulation and measurement in the range of frequencies 100 Hz to 10 kHz. In the simulation, the spiral coils with four cuts were discretised to 14,000 nodes and 27,064 triangles; it took eight minutes to finish the calculation for all frequencies when

using two Intel Xeon six-core X5650 (CPU, 2.66 GHz; RAM, 128 GB). For the case without cutting, the results at the low frequencies in Figure 7.11 show a strong agreement between the simulated and measured resistances. The difference of the resistance between the experiment and the simulation results increases with the frequency, which is about 10% at 10 kHz. The deviation between the measured and simulated inductances is about 3.4%. The resistance of the spiral coils with cuts is larger than the coils without cuts at low frequencies, but smaller at high frequencies. The inductance of the spiral coils increases with cutting. These comparative results demonstrate that the numerical simulation tool is accurate in modelling the intra-coil interactions.

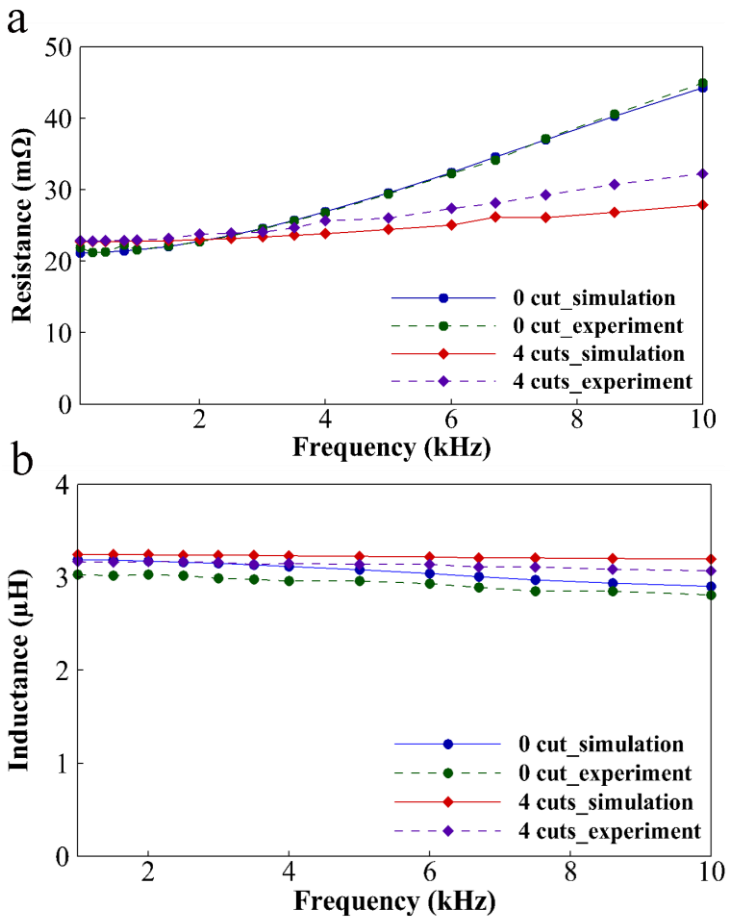

Figure 7.11 Comparison between experimental result and simulation result, (a) resistance, (b) inductance.

7.3.2.2 Complete cutting

A. Eddy currents in passive coils

The coils were meshed in accordance with the skin effect, so that the discretised nodes and triangles increase with the cut numbers and frequency. Based on a preliminary convergence study, one-eighth coils are discretised with 42,000 nodes and 78,530 triangles. The simulation was undertaken using Matlab 2014b and was finished in 90 mins.

Figure 7.12 compares the current density in the tracks of the passive coil with and without cuts at 1 kHz and 10 kHz. The eddy current density distribution in the passive *y*-coil at 1 kHz is reduced after cutting. Figure 7.12c presents the current density along the red line in Figure 7.12a–b (with $0 \leq \theta \leq \pi/2$, from the left to the right in the figures). The current density is reduced by nearly 70% and the eddy currents distribute more uniformly in the slit coil tracks.

The eddy current density induced in the surrounding coils with three cuts is higher at 10 kHz (Figure 7.12e) than at 1 kHz (Figure 7.12b). Figure 7.12f compares the current density profiles in those coils with and without cutting. After three cuts, the peak current density values have been reduced, however, in the rest of positions, the current density profiles are altered up and down, causing nonlinear power loss alternations with respect to frequency (see the crossing point in Figure 7.13).

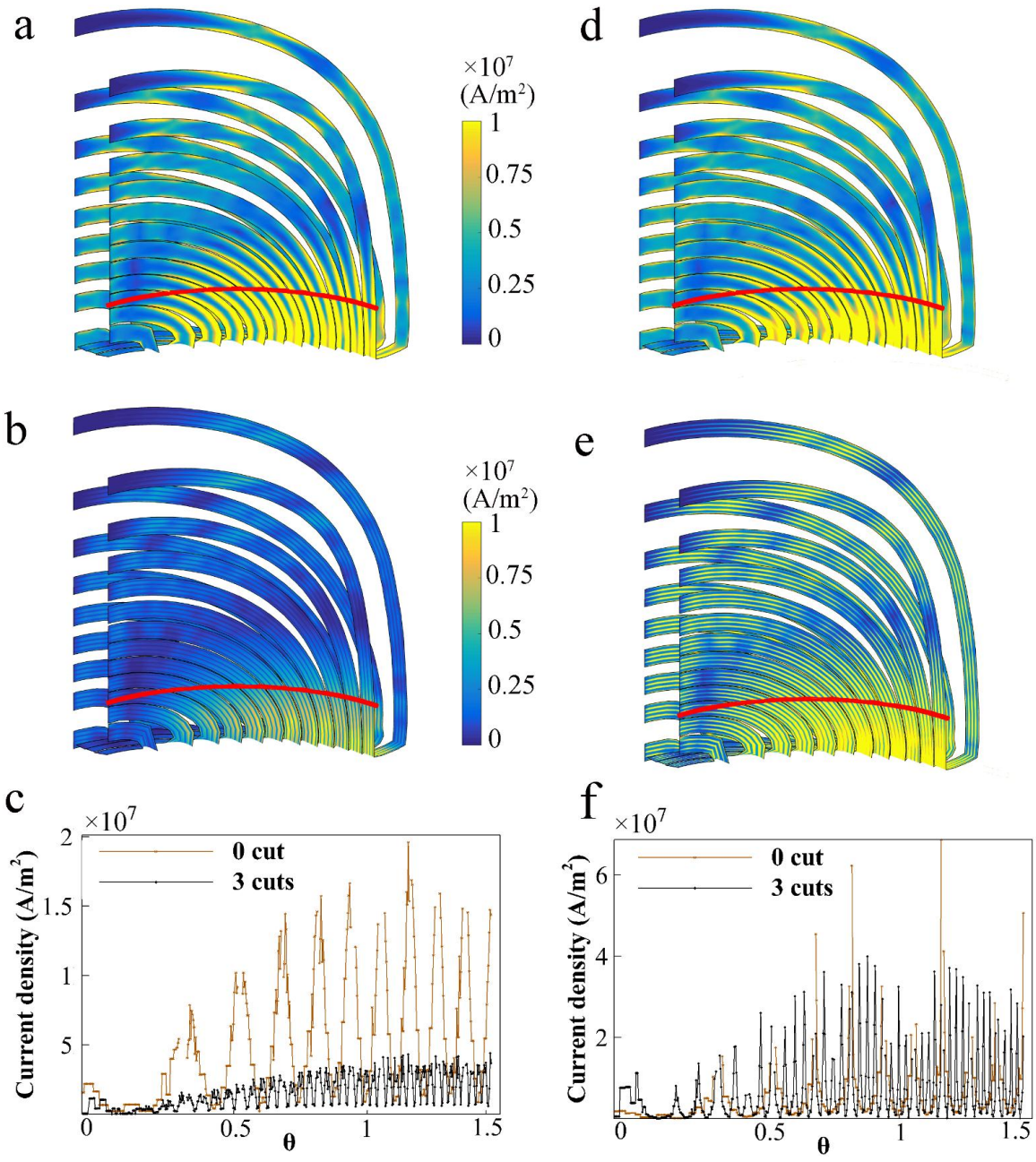

Figure 7.12 Current density in the passive *y*-coil, (a) no-cut (f = 1 kHz), (b) three cuts (f = 1 kHz), (c) spatial current density distribution along the red line indicated in Figure 7.12 5a–b, (d) no-cut (f = 10 kHz), (e) three cuts (f = 10 kHz), (f) spatial current density distribution along the red line indicated in Figure 7.12 5d–e (f = 10 kHz).

The power loss shown in Figure 7.13 produced in the passive y-gradient coil increases with the frequency. The passive coils with cuts dissipate less power at low frequencies, but more at frequencies higher than 4 kHz. At 1 kHz, the power is reduced by 40% for the coil with one cut and by 85% for the coil with four cuts.

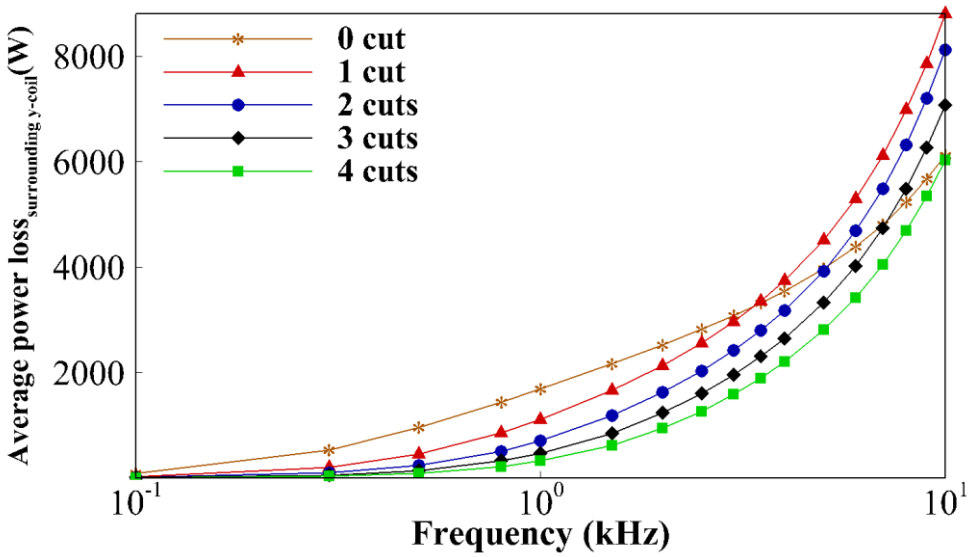

Figure 7.13 Average power loss dissipated by the passive y-coil for different cut numbers.

Figure 7.14 presents the real part of magnetic field generated by the eddy currents in the passive *y*-coil at the 1 kHz frequency. The field is calculated along the *x*-axis across the DSV for $y = z = 0$. Compared to the coil without cuts, the magnetic field induced by the eddy currents in the passive coil with cuts is smaller, which reduces to 34.7, 14.4, 7.2, 4 % for one to four cuts, respectively. The linearity of the secondary field induced by the eddy currents in the passive *y*-coil is shown in Table 7.2. The field is calculated at all the sampling points of the DSV. The gradient field values show that the eddy currents in the passive coils produce a linear secondary field for all coils. The gradient and the magnetic field leakage ratios have been significantly reduced for slit coils, and the field offsets of all the coils are small enough to be neglected.

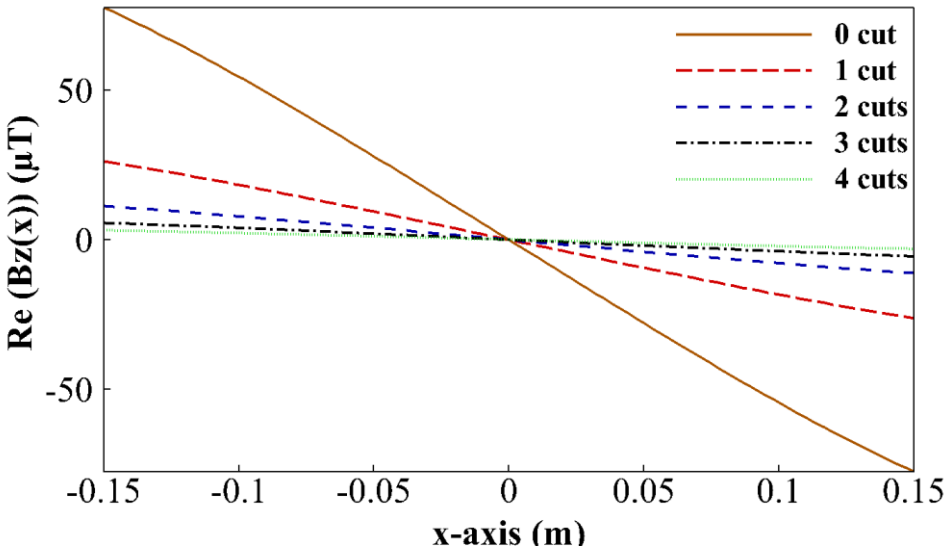

Figure 7.14 Real part of the magnetic field produced by the eddy currents in the passive coil with different cuts.

Table 7.2 Field Linearity

	Gradient (mT/m)	Offset(mT)	r^2	$\lambda_{leakratio}$
0 cut	-5.60e-4	-5.20e-8	0.9965	5.93
1 cut	-1.89e-4	-1.72e-8	0.9967	1.87
2 cuts	-8.07e-5	-7.32e-9	0.9967	0.78
3 cuts	-4.02e-5	-3.66e-9	0.9967	0.38
4 cuts	-2.24e-5	-2.04e-9	0.9967	0.21

B. Active coil performance

Figure 7.15 shows the color map of the current density distribution of the active *x*-coil without cuts and with three cuts at the 1 kHz and 10 kHz frequencies. The current density in the active *x*-coil with three cuts is slightly more uniform than that of the no-cut in some tracks at the 1 kHz frequency (the middle of the red line shown in Figure 7.15a and b). This is demonstrated by the current density distribution along the redlines in Figure 7.15c. The current density in the active coil without cuts has a larger peak value

and a smaller minimum value than the three cuts, and the current density is slightly higher at the cutting places. At a higher frequency, for example 10 kHz, this effect is more accentuated as shown in Figure 7.15d–e.

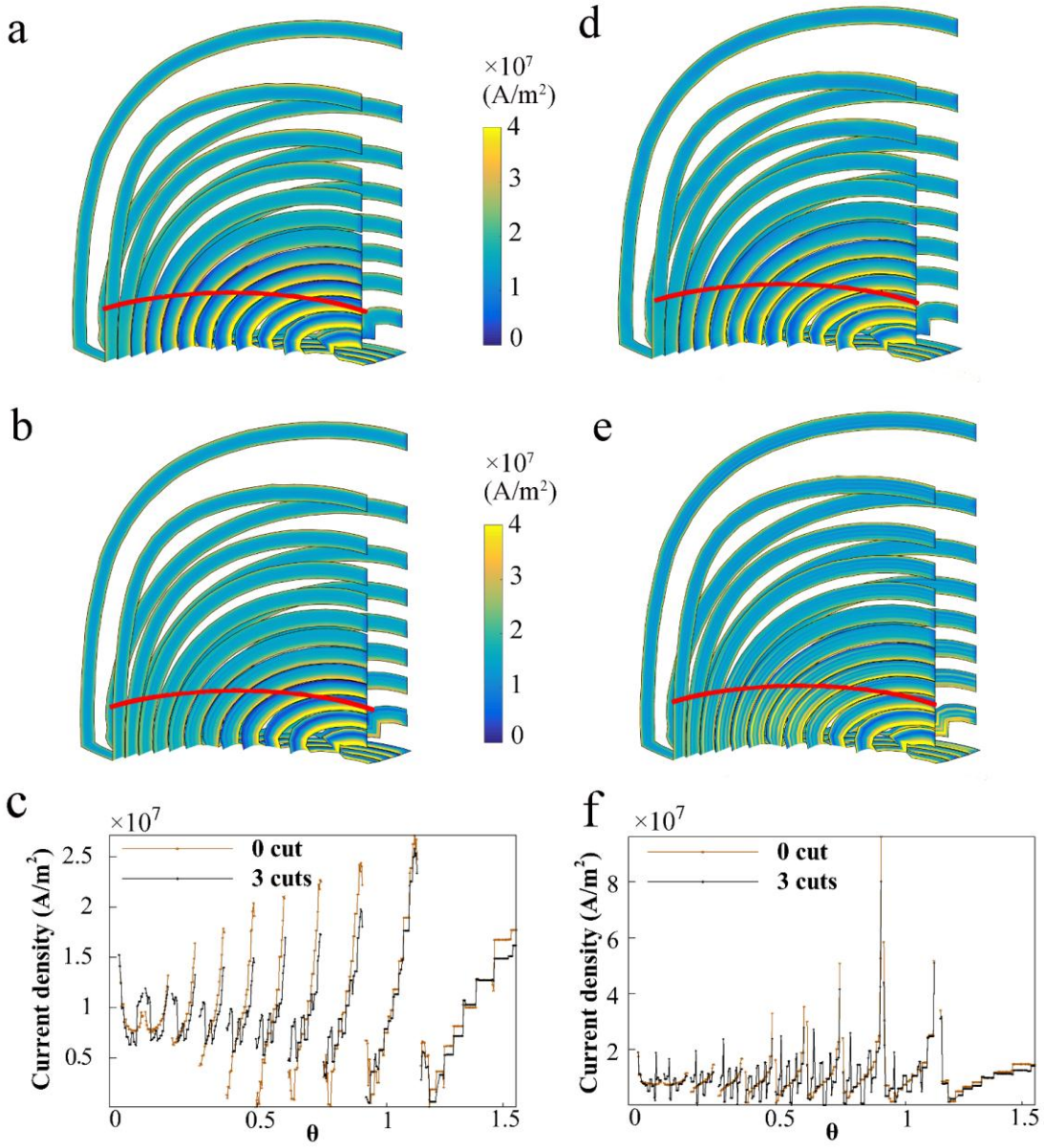

Figure 7.15 Current density in the active *x*-coil, (a) no-cut (f = 1 kHz), (b) three cuts (f = 1 kHz), (c) spatial current density distribution along the red line indicated in Figure 7.15 8a–b, (d) no-cut (f = 10 kHz), (e) three cuts (f = 10 kHz), (f) spatial current density distribution along the red line indicated in Figure 7.15d–e (f = 10 kHz).

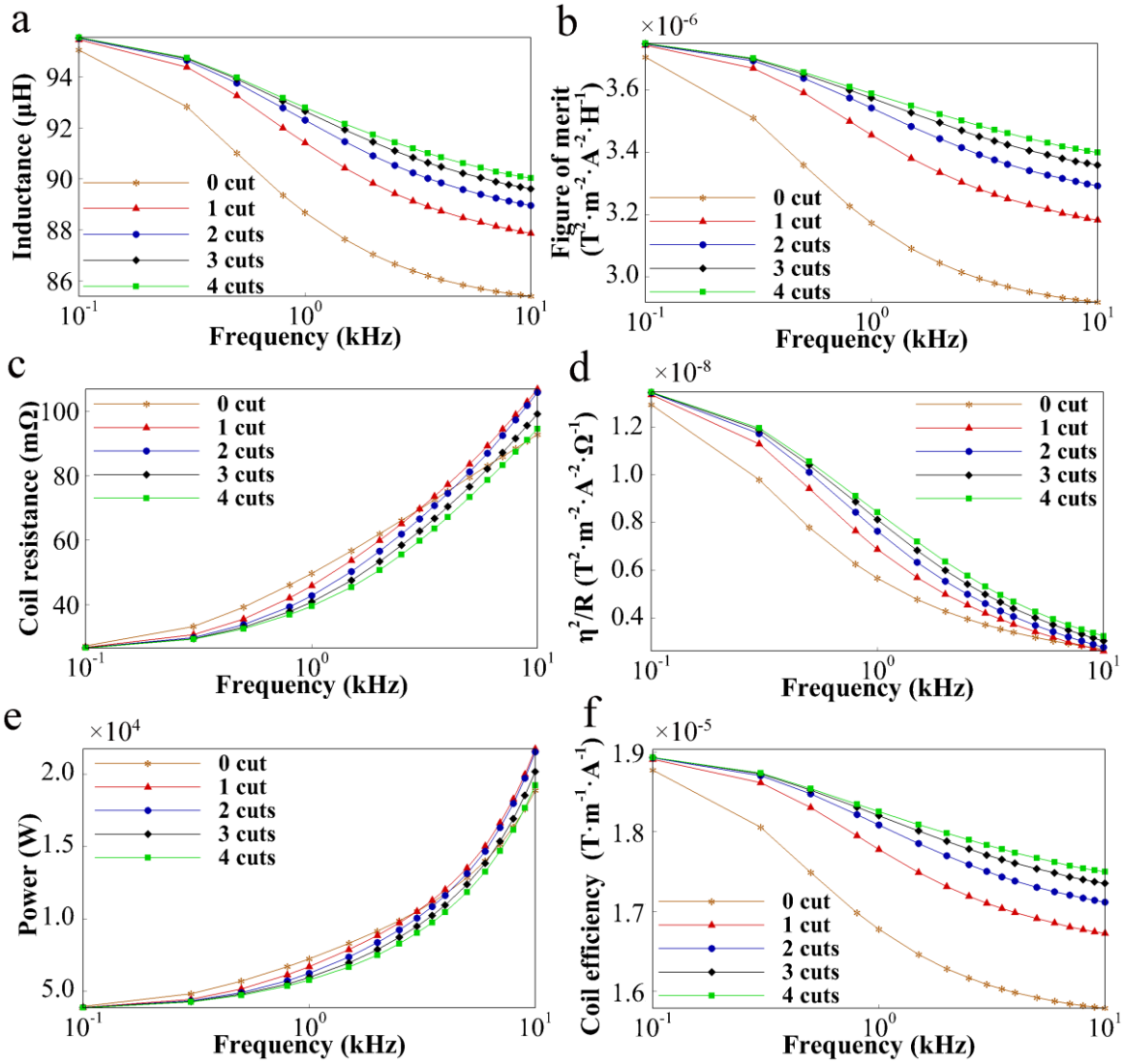

Figure 7.16 The performance of the active *x*-coil considering the passive coil, (a) inductance, (b) resistance, (c) Figure of Merit, (d) η^2/R, (e) average power loss, (f) efficiency.

Figure 7.16 shows the trends of inductance, resistance, FoM, η^2/R, total average power loss and coil efficiency of the active *x*-coil considering surrounding passive coils with different number of cuts. In general, the inductance, FoM and efficiency active *x*-coil increase with the cut numbers. Meanwhile, the differences for these performances increase with frequency. Compared with the coil with no cut, the inductance increases by 3.0, 3.8, 4.13 and 4.26% for the cuts numbered from one to four, respectively. Correspondingly, the efficiency increases by 8.5, 10.8, 11.6 and 11.9%, and the FoM increases by 5.7,

7.2, 7.8 and 8.0%. Furthermore, the η^2/R is improved with coil cuts at a low frequency, which was improved to 22.2% for one cut and 45.7% for four cuts.

7.3.2.3 Adaptive cutting vs completing cutting

A. Eddy currents in passive coils

The eddy current density in the passive coil with adaptive cutting shown in Figure 7.17 is similar at the cutting place to the complete cut in Figure 7.12. The power loss dissipated by the passive coil with adaptive cutting is similar to that produced by the complete cut, with differences comparable with the discretization error (Figure 7.17c).

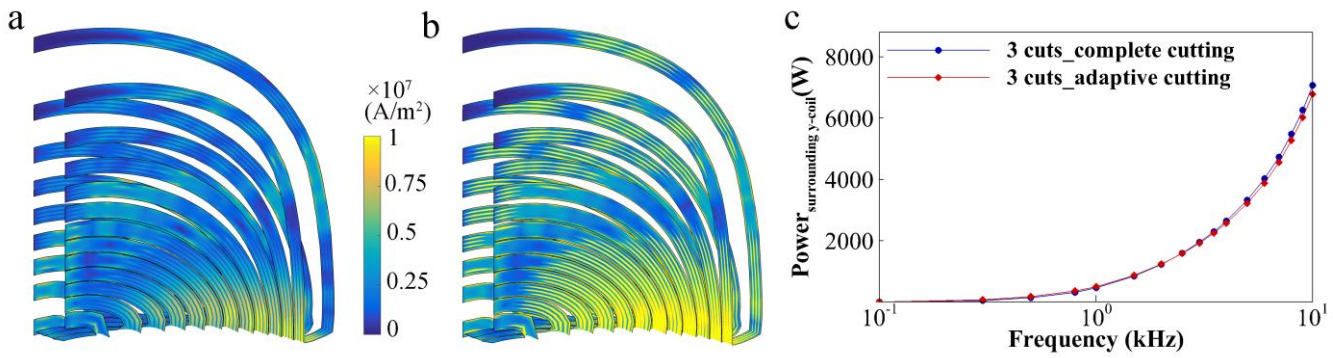

Figure 7.17 Eddy current density and average power loss in the passive *y*-coil with three adaptive cuts, (a) 1 kHz, (b) 10 kHz, (c) power loss.

B. Active coil performance

Figure 7.18 compares the performance of the active *x*-coil considering the passive coil with three cuts. The FoM, η^2/R, total power loss and efficiency of the coil with adaptive cutting are slightly smaller than that of the complete cutting. The inductance, FoM, total power loss and efficiency have the largest differences at the 10 kHz frequency; these are 0.48, 1.46, 4.03 and 0.89%, respectively. The resistance of the active coil is nearly the same for the two different cut strategies.

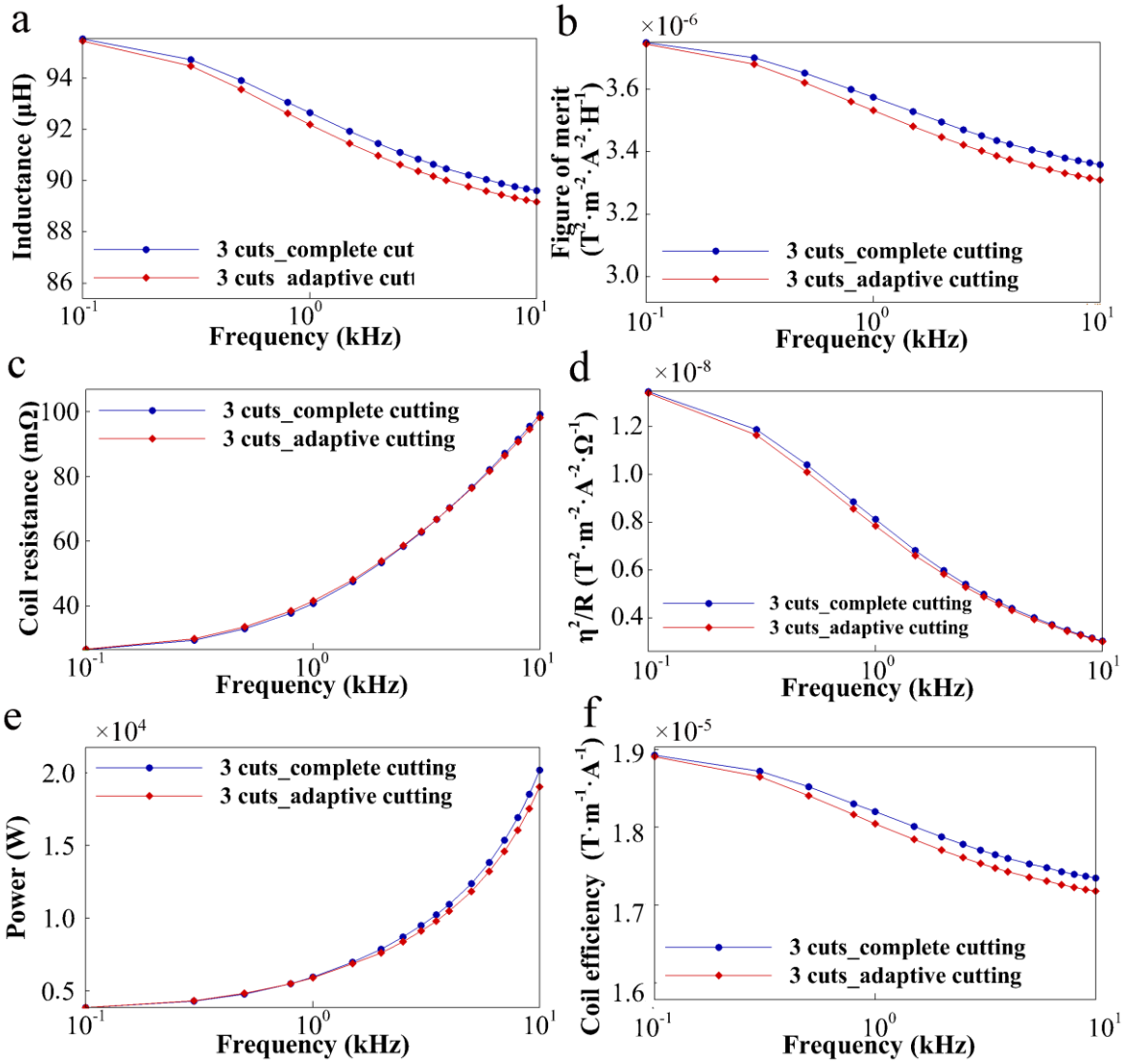

Figure 7.18 The performance of the active *x*-coil considering the passive coil with three complete and adaptive cuts, (a) inductance, (b) resistance, (c) Figure of Merit, (d) η^2/R, (e) average power loss, (f) efficiency.

7.3.3 Discussion

7.3.3.1 Experimental validation

As shown above, the simulation and experimental results are closely matched, with a certain amount of deviation that might be caused by the manufacturing tolerances on cutting or measurement errors associated with the ultra-thin PCBs copper and other sources. In the spiral coils with slits, the material

removed to allocate the cuts decreases the equivalent cross section and, consequently, slightly increases the resistance of the coil. This is more evident in the experiment, where the track width is not much larger than the cut width. As soon as the frequency increases, the losses caused by eddy currents become predominant and the use of cuts becomes effective in the reduction of the equivalent resistance. Consequently, the resistance of the coil with four cuts is higher than that of the no-cut coil at low frequencies, but lower at high frequencies.

7.3.3.2 Complete cutting

As shown in Figure 7.12a-c, at low frequencies the current density in the passive coils with cuts is reduced, owing to the blocking of the return path of the eddy currents in the passive coils. With an increase in frequency, however, the skin effects in the passive coils become more apparent. This behaviour can be explained by the interaction between the skin depth and the dimensions of the slit track. Going from 0.1 to 10 kHz, the penetration depth for copper with the properties reported in Table 1, ranges from 6.5 mm to 0.65 mm. For example, cutting the track into four parts means that the width of 30 mm is subdivided in four sub-tracks with 7.5 mm width each. This width is fairly similar to the skin depth at 100 Hz, but is much larger than that at 10 kHz. Consequently, at lower frequencies, two currents on the opposite sides of the sub-track interact with each other, leading to the combined-effect of loss reduction caused by area reduction and resistance increase, as introduced in Section IIB. On the other hand, at higher frequencies, the skin depth is much smaller than the sub-track width. Thus, the area reduction factor is effective, but the Ohmic resistance of the eddy currents does not increase significantly, because the skin depth is actually much smaller than the width of each sub-track and more edges are generated by the slits. Therefore, the current density is considerably spread over the complete sub-track width, as is appreciable in Figure 7.12f. Thus, the losses can be even higher in the passive coils with cuts than those with the uncut geometry. Fortunately, most frequency components in the gradient pulse are lower than 1 kHz.

The secondary field produced by the eddy currents in the passive coils is significantly reduced by cutting. In addition, the secondary field linearity is improved. This indicates that the secondary field generated by the eddy currents in the passive coils can be compensated for by the pulse pre-emphasis method [124].

The current density in the active coil tends to be uniform in the cut tracks where it overlaps the passive coil tracks, this is resulted in by the orthogonal magnetic field generated by the eddy currents in the

passive coil. Additionally, the current density at the corners of the tracks with larger curvature tends to be more uniform because of the slit structure.

The resistance increases with frequency, because of the reduced skin depth at high frequencies. The resistance reduces by cutting at low frequencies mainly because of the reduced eddy currents in the passive coil. The decrease of the resistance in the passive coil will lead to the decreased inductance in the active coil. Nevertheless, the inductance of the active coil increases faster with the number of cuts [150]; although the inductance is reduced by the decreased resistance at low frequencies, the inductance still increases with the cutting numbers. This behaviour can be explained by a lower mutual inductance effect between the two coils caused by the reduced eddy current path that, physically, leads to a higher apparent inductance as seen in the power supply side.

The average power loss in the active and passive coils is reduced by the coil cuts at low frequencies, owing to less induced eddy currents in the passive coils with cuts and lesser resistance. The gradient field related coil performance FoM, η^2/R and coil efficiency are improved, because the secondary field generated by the eddy currents in the passive coils is reduced by the cutting and the field direction is opposite to that produced by the gradient coil. In spite of the increment of the inductance in coils with cuts, the FoM is improved, because of the improvement in the gradient field. The inductance is increased by 3% for the coil with one cut, while the efficiency, FoM and η^2/R increase by 5.7, 8.5, and 22.2%, respectively. Furthermore, the benefit increases with the number of cuts. Therefore, cutting the gradient coils improves the coil efficiency, reduces the power dissipation in the gradient coil set.

7.3.3.3 Adaptive cutting vs completing cutting

We studied the complete cut, because it is not biased for the specific choice of the cut length and the threshold of the eddy current density. Nevertheless, from the manufacturing point of view, the complete cut may lead to a mechanical weakness, so a less intrusive action can be adopted. The results shown in Figure 7.17 and 11 demonstrate that the adaptive cutting can be as efficient as complete cutting.

7.3.4 Conclusion

In this work, we proposed a novel solution for reducing the eddy current effects induced by gradient coil intra-interactions. With a slit coil configuration, the average power loss and the impurity of the gradient field have been reduced over a large range of frequencies.

It was found that, at low frequencies, the power produced by a passive coil with cuts is reduced, which results in the reduction of the total power. At the 1 kHz frequency, for the coil with four cuts, the power produced by the passive coil was reduced to only 15% and the secondary magnetic field was reduced to only 4% of those in the no-cut coil. Furthermore, the coil performance had significant improvement after cutting the coil tracks.

8. Conclusion

The thesis investigates improvements to the MRI gradient coil technology, focusing on novel local gradient coil designs and eddy current management. To facilitate advanced brain imaging, an asymmetric head gradient coil is proposed and described in Chapter 4. In terms of the eddy currents caused by the rapid switching of the gradient coils, this thesis presents a series of comprehensive investigations (Chapters 5–7) with the intention to reduce eddy currents and improve gradient field linearity. It is hoped that the research in this thesis will assist in the development of a number of gradient coil systems including head coil inserts, conventional whole-body MRI and hybrid MRI-LINAC systems.

8.1 Contributions and implications

8.1.1 An improved asymmetrical head gradient coil design (Chapter 4)

A new head coil configuration was proposed to improve the performance of the asymmetric coils. This coil takes full advantages of the characteristic features of the asymmetric configurations and 3D structure. In the new coil, the primary and secondary coils were connected at the patient end thus accommodating additional surface area for the current flow. The service end was open to provide access to the shimming tray, cooling pipes and so on. The simulation result indicated that, compared to conventional designs, the new head coil showed a significant performance improvement for both transverse and longitudinal coils. It is hoped that the proposed coil will be particularly useful in the design of asymmetric head gradient coils with limitations on both inner and outer radii.

8.1.2 Skin and proximity effects in the gradient coils (Chapter 5)

The skin and proximity effects between coil tracks were investigated in terms of coil geometry and driven waveform. The MIM described in Chapter 3 was extended to study the skin and proximity effects caused by different coil widths and frequencies and the extended method was validated experimentally. When compared to the experimentally acquired results, the extended MIM was able to accurately estimate the skin and proximity effects in the coil tracks. This extended method was then used to analyse the designed coils with different coil track widths. The results indicated that it was inaccurate to evaluate a coil with

track width using a filamentary coil or using uniform current density and that the track width should be considered carefully during the coil design process to get a trade-off between coil parameters.

8.1.3 Cross-talk between gradient coils (Chapter 6)

This part concerns the intra-coil eddy currents in the gradient coils which were neglected previously. To study the impact of the track width on the cross-talk between coils, gradient coils with different track widths were designed and simulated. The study found that the intra-coil eddy currents are more significant for wide tracks. In addition, an optimal track width of 14 mm was determined for conventional coils and a track width of 20 to 24 mm for split coils to improve coil performance considering intra-coil eddy currents.

8.1.4 On the mitigation of cross-talk between gradient coils (Chapter 7)

In order to reduce the intra-coil eddy currents, a novel solution of applying lamination to the gradient coil tracks was proposed. Specifically, the coil tracks were slit along the direction of the current flow to create a different number of sub-tracks. Compared with the original uncut coils, eddy currents induced in the slit coils were significantly reduced over a large range of frequencies. The findings in this work present that slitting the coils tracks is an effective way to mitigate intra-coil eddy currents and improve the coil performance, and is a practical approach to apply in both conventional MRI scanner and hybrid MRI-LINAC systems.

8.1.5 Implications

This research has presented a series of original and creative research studies for asymmetric insertable head coil designs and eddy current reduction. In the various studies, the asymmetric head coil inserts had a relative small ROU, which results in substantial image distortions in head imaging. This thesis utilised the features of the asymmetric head coil configuration and designed a one-end-connect head coil (Chapter 4). It is hoped that this novel approach will benefit techniques that need fast switching gradients such as EPI and other diffusion imaging. This thesis also conducted a comprehensive study of intra-coil eddy currents. As indicated in the various studies, eddy currents are one of the bottlenecks of the gradient coils. However, the intra-coil eddy currents have not been studied in detail in previous investigations of gradient coils. This thesis conducted a comprehensive study of the conductive coupling between the coil tracks

(Chapter 5) and the gradient coils themselves (Chapter 6). A coil track slit strategy has been demonstrated to be effective in intra-coil eddy current mitigation (Chapter 7). The studies in this thesis reduced the intra-coil eddy currents and are likely to improve the resolution of the images produced by conventional MRI scanners and hybrid MRI-LINAC systems.

8.2 Limitations and future work

Future work will mainly focus on improvements to and evaluation of the head coils (Chapter 4) and the implementation of the eddy current reduction strategies proposed in this thesis. Practical validation of the eddy current reduction strategy using slits (Chapter 7) will be of particular interest.

8.2.1 Evaluation of the improved asymmetric head coils

The one-end-connect head coils have theoretically proven they have improved coil performance compared to the conventional coils. However, patient safety issues such as PNS have not yet been studied. In future work, a detailed safety analysis will be conducted to ensure the new design of the head coil is patient friendly. Furthermore, as described in Chapter 4, the proposed one-end-connect head coil has larger minimum wire spacing than the separated coils and the wires are sparser because of the extra field contribution from the connected surface. This larger minimum spacing reduces the peak temperature in the gradient coils [137] and a detailed thermal analysis and testing will be undertaken to further demonstrate the advantages of the design. In addition, in [153], it was found that the connected coil emitted a lower acoustic radiation. In our near future work, the safety, thermal and acoustic properties will be fully evaluated for the proposed one-end-connect head coil and then validated with experiments.

8.2.2 Evaluation of the slit coils

The slit coils have demonstrated their capacity to reduce eddy currents and enhance coil performance. Slitting the coil tracks alters the current distribution in the coil tracks and mechanical structures, thus affecting heating, acoustic and mechanical strength, which will be evaluated in our future work. Consequently, the slitting strategy may also be improved for the purpose of temperature control, acoustic noise reduction and mechanical strength enhancement.

9. Reference

[1] J. Jin, *Electromagnetic analysis and design in magnetic resonance imaging*: CRC press, 1998.

[2] T. F. Budinger, H. Fischer, D. Hentschel, H.-E. Reinfelder, and F. Schmitt, "Physiological effects of fast oscillating magnetic field gradients," *Journal of computer assisted tomography,* vol. 15, no. 6, pp. 909-914, 1991.

[3] M. S. Cohen, R. M. Weisskoff, R. R. Rzedzian, and H. L. Kantor, "Sensory stimulation by time‐varying magnetic fields," *Magnetic resonance in medicine,* vol. 14, no. 2, pp. 409-414, 1990.

[4] B. Zhang, Y. F. Yen, B. A. Chronik, G. C. McKinnon, D. J. Schaefer, and B. K. Rutt, "Peripheral nerve stimulation properties of head and body gradient coils of various sizes," *Magnetic resonance in medicine,* vol. 50, no. 1, pp. 50-58, 2003.

[5] D. C. Alsop, and T. J. Connick, "Optimization of torque‐balanced asymmetric head gradient coils," *Magnetic resonance in medicine,* vol. 35, no. 6, pp. 875-886, 1996.

[6] S. Crozier, K. Luescher, G. Hinds, W. U. Roffmann, and D. M. Doddrell, "Designs for an asymmetric gradient set and a compact superconducting magnet for neural magnetic resonance imaging," *Review of scientific instruments,* vol. 70, no. 10, pp. 4062-4066, 1999.

[7] S. Lee, J. Mathieu, and J. Piel, "Brain imaging with a dedicated asymmetric head-only gradient coil without peripheral nerve stimulation at 500 T/m/s." p. 0310.

[8] S. Crozier, W. U. Roffmann, K. Luescher, C. Snape-Jenkinson, L. K. Forbes, and D. M. Doddrell, "An "openable," high-strength gradient set for orthopedic MRI," *Journal of Magnetic Resonance,* vol. 139, no. 1, pp. 81-89, 1999.

[9] B. A. Chronik, and B. K. Rutt, "A comparison between human magnetostimulation thresholds in whole‐body and head/neck gradient coils," *Magnetic resonance in medicine,* vol. 46, no. 2, pp. 386-394, 2001.

[10] B. A. Chronik, A. Alejski, and B. K. Rutt, "Design and fabrication of a three‐axis edge ROU head and neck gradient coil," *Magnetic resonance in medicine,* vol. 44, no. 6, pp. 955-963, 2000.

[11] G. Ries, “Eddy current transients and forces in cryostat walls of superconducting solenoids,” *Magnetics, IEEE Transactions on*, vol. 24, no. 1, pp. 516-519, 1988.

[12] J. Kroot, S. van Eijndhoven, and A. van de Ven, “Eddy currents in a transverse MRI gradient coil,” *Journal of Engineering Mathematics,* vol. 62, no. 4, pp. 315-331, 2008.

[13] D. Hughes, S. Robertson, and P. Allen, “Intensity artifacts in MRI caused by gradient switching in an animal‐size NMR magnet,” *Magnetic resonance in medicine*, vol. 25, no. 1, pp. 167-179, 1992.

[14] D. Le Bihan, C. Poupon, A. Amadon, and F. Lethimonnier, “Artifacts and pitfalls in diffusion MRI,” *Journal of magnetic resonance imaging*, vol. 24, no. 3, pp. 478-488, 2006.

[15] E. A. Badeaf, and O. Craius, “Eddy Current Effects in superconducting Magnets,” *IEEE transactions on magnetics*, vol. 33, no. 2, 1997.

[16] F. Tang, H. Sanchez Lopez, F. Freschi, E. Smith, Y. Li, M. Fuentes, F. Liu, M. Repetto, and S. Crozier, “Skin and proximity effects in the conductors of split gradient coils for a hybrid Linac-MRI scanner,” *Journal of Magnetic Resonance,* vol. 242, pp. 86-94, 2014.

[17] F. Tang, F. Freschi, H. S. Lopez, M. Repetto, F. Liu, and S. Crozier, “Intra-coil interactions in split gradient coils in a hybrid MRI–LINAC system,” *Journal of Magnetic Resonance,* vol. 265, pp. 52-58, 2016.

[18] F. Tang, F. Freschi, M. Repetto, Y. Li, F. Liu, and S. Crozier, “Mitigation of Intra-coil Eddy Currents in Split Gradient Coils in a Hybrid MRI-LINAC System,” *IEEE Transaction on Biomedical Engineering*, 2016 (accepted).

[19] F. Bloch, “Nuclear induction,” *Physical review*, vol. 70, no. 7-8, pp. 460, 1946.

[20] E. M. Purcell, H. Torrey, and R. V. Pound, “Resonance absorption by nuclear magnetic moments in a solid,” *Physical review*, vol. 69, no. 1-2, pp. 37, 1946.

[21] R. A. Serway, and J. W. Jewett, *Physics for scientists and engineers with modern physics*: Nelson Education, 2013.

[22] N. F. Mott, E. Bullard, R. Fowler, and P. Kapitza, *The International Series of Monographs on Physics*: Oxford University Press In-8 °.

[23] D. Canet, “Nuclear magnetic resonance: concepts and methods,” 1996.

[24] E. Haacke, R. Brown, M. Thompson, and R. Venkatesan, "Magnetic Resonance Imaging: Physical Properties and equence Design," Wiley-Liss, New York, 1999.

[25] R. W. Brown, Y.-C. N. Cheng, E. M. Haacke, M. R. Thompson, and R. Venkatesan, *Magnetic resonance imaging: physical principles and sequence design*: John Wiley & Sons, 2014.

[26] W. Edelstein, G. Glover, C. Hardy, and R. Redington, "The intrinsic signal‐to‐noise ratio in NMR imaging," *Magnetic Resonance in Medicine,* vol. 3, no. 4, pp. 604-618, 1986.

[27] D. I. Hoult, and R. Richards, "The signal-to-noise ratio of the nuclear magnetic resonance experiment," *Journal of Magnetic Resonance (1969),* vol. 24, no. 1, pp. 71-85, 1976.

[28] T.-K. Truong, D. W. Chakeres, D. Q. Beversdorf, D. W. Scharre, and P. Schmalbrock, "Effects of static and radiofrequency magnetic field inhomogeneity in ultra-high field magnetic resonance imaging," *Magnetic resonance imaging,* vol. 24, no. 2, pp. 103-112, 2006.

[29] A. Maiorana, T. Scarabino, V. d'Alesio, M. Tosetti, M. Armillotta, and U. Salvolini, "High-Field MRI and Safety: II. Utilization," *High Field Brain MRI*, pp. 6-9: Springer, 2006.

[30] A. N. Garroway, P. K. Grannell, and P. Mansfield, "Image formation in NMR by a selective irradiative process," *Journal of Physics C: Solid State Physics,* vol. 7, no. 24, pp. L457, 1974.

[31] J. Pauly, D. Nishimura, and A. Macovski, "A k-space analysis of small-tip-angle excitation," *Journal of Magnetic Resonance (1969),* vol. 81, no. 1, pp. 43-56, 1989.

[32] M. N. Wilson, "Superconducting magnets," 1983.

[33] M. Just, H. Rösler, H. Higer, J. Kutzner, and M. Thelen, "MRI-assisted radiation therapy planning of brain tumors-clinical experiences in 17 patients," *Magnetic resonance imaging,* vol. 9, no. 2, pp. 173-177, 1991.

[34] J. F. Schenck, F. A. Jolesz, P. B. Roemer, H. E. Cline, W. E. Lorensen, R. Kikinis, S. G. Silverman, C. J. Hardy, W. D. Barber, and E. T. Laskaris, "Superconducting open-configuration MR imaging system for image-guided therapy," *Radiology,* vol. 195, no. 3, pp. 805-814, 1995.

[35] D. Verellen, M. De Ridder, N. Linthout, K. Tournel, G. Soete, and G. Storme, "Innovations in image-guided radiotherapy," *Nature Reviews Cancer,* vol. 7, no. 12, pp. 949-960, 2007.

[36] D. A. Jaffray, J. H. Siewerdsen, J. W. Wong, and A. A. Martinez, "Flat-panel cone-beam computed tomography for image-guided radiation therapy," *International Journal of Radiation Oncology* Biology* Physics,* vol. 53, no. 5, pp. 1337-1349, 2002.

[37] M. H. Smitsmans, J. De Bois, J.-J. Sonke, A. Betgen, L. J. Zijp, D. A. Jaffray, J. V. Lebesque, and M. Van Herk, "Automatic prostate localization on cone-beam CT scans for high precision image-

guided radiotherapy," *International Journal of Radiation Oncology* Biology* Physics,* vol. 63, no. 4, pp. 975-984, 2005.

[38] H. Shirato, S. Shimizu, K. Kitamura, T. Nishioka, K. Kagei, S. Hashimoto, H. Aoyama, T. Kunieda, N. Shinohara, and H. Dosaka-Akita, "Four-dimensional treatment planning and fluoroscopic real-time tumor tracking radiotherapy for moving tumor," *International Journal of Radiation Oncology* Biology* Physics,* vol. 48, no. 2, pp. 435-442, 2000.

[39] C. F. Serago, S. J. Chungbin, S. J. Buskirk, G. A. Ezzell, A. C. Collie, and S. A. Vora, "Initial experience with ultrasound localization for positioning prostate cancer patients for external beam radiotherapy," *International Journal of Radiation Oncology* Biology* Physics,* vol. 53, no. 5, pp. 1130-1138, 2002.

[40] J. Lattanzi, S. McNeeley, W. Pinover, E. Horwitz, I. Das, T. E. Schultheiss, and G. E. Hanks, "A comparison of daily CT localization to a daily ultrasound-based system in prostate cancer," *International Journal of Radiation Oncology* Biology* Physics,* vol. 43, no. 4, pp. 719-725, 1999.

[41] C. B. Caldwell, K. Mah, M. Skinner, and C. E. Danjoux, "Can PET provide the 3D extent of tumor motion for individualized internal target volumes? A phantom study of the limitations of CT and the promise of PET," *International Journal of Radiation Oncology* Biology* Physics,* vol. 55, no. 5, pp. 1381-1393, 2003.

[42] S. Janek, R. Svensson, C. Jonsson, and A. Brahme, "Development of dose delivery verification by PET imaging of photonuclear reactions following high energy photon therapy," *Physics in medicine and biology,* vol. 51, no. 22, pp. 5769, 2006.

[43] J. J. Lagendijk, B. W. Raaymakers, A. J. Raaijmakers, J. Overweg, K. J. Brown, E. M. Kerkhof, R. W. van der Put, B. Hårdemark, M. van Vulpen, and U. A. van der Heide, "MRI/linac integration," *Radiotherapy and Oncology,* vol. 86, no. 1, pp. 25-29, 2008.

[44] P. J. Keall, M. Barton, and S. Crozier, "The Australian Magnetic Resonance Imaging–Linac Program." pp. 203-206.

[45] J. Yun, K. Wachowicz, M. Mackenzie, S. Rathee, D. Robinson, and B. Fallone, "First demonstration of intrafractional tumor-tracked irradiation using 2D phantom MR images on a prototype linac-MR," *Medical physics,* vol. 40, no. 5, pp. 051718/1-051718/12, 2013.

[46] B. Fallone, B. Murray, S. Rathee, T. Stanescu, S. Steciw, S. Vidakovic, E. Blosser, and D. Tymofichuk, "First MR images obtained during megavoltage photon irradiation from a prototype integrated linac-MR system," *Medical physics,* vol. 36, no. 6, pp. 2084-2088, 2009.

[47] B. Raaymakers, J. Lagendijk, J. Overweg, J. Kok, A. Raaijmakers, E. Kerkhof, R. van der Put, I. Meijsing, S. Crijns, and F. Benedosso, "Integrating a 1.5 T MRI scanner with a 6 MV accelerator: proof of concept," *Physics in medicine and biology,* vol. 54, no. 12, pp. N229, 2009.

[48] B. Raaymakers, A. Raaijmakers, A. Kotte, D. Jette, and J. Lagendijk, "Integrating a MRI scanner with a 6 MV radiotherapy accelerator: dose deposition in a transverse magnetic field," *Physics in medicine and biology,* vol. 49, no. 17, pp. 4109, 2004.

[49] J. Lagendijk, B. Raaymakers, J. Overweg, J. Kok, E. Kerkhof, A. Raaijmakers, R. van der Put, I. Meijsing, S. Crijns, and F. Benedosso, "WE‐D‐BRC‐04: MR‐XRT at 1.5 T, the UMC Utrecht Hybrid MRI Linac System," *Medical Physics,* vol. 36, no. 6, pp. 2775-2775, 2009.

[50] S. Shvartsman, G. DeMeester, T. Eagan, S. Bates, and M. Savill, "A split gradient coil for high speed imaging with application to MRI-RT," *Proc. Int. Society For Magnetic Resonance in Medicine (Stockholm,),* 2010.

[51] G. D. DeMeester, J. F. Dempsey, J. L. Patrick, and S. M. Shvartsman, "Split magnetic resonance imaging system," Google Patents, 2011.

[52] S. M. Shvartsman, G. D. DeMeester, J. L. Patrick, and J. F. Dempsey, "Self-shielded gradient coil," Google Patents, 2014.

[53] N. Shaw, R. Ansorge, and T. Carpenter, "Commissioning and testing of split coil MRI system for combined PET-MR," *Proc Int Soc Magn Reson Med, Miami Beach, Florida,* vol. 13, pp. 407, 2005.

[54] L. Liu, A. Trakic, H. Sanchez Lopez, F. Liu, and S. Crozier, "An analysis of the gradient-induced electric fields and current densities in human models when situated in a hybrid MRI-LINAC system," *Physics in medicine and biology,* vol. 59, no. 1, pp. 233, 2014.

[55] P. T. While, M. S. Poole, L. K. Forbes, and S. Crozier, "Minimum maximum temperature gradient coil design," *Magnetic Resonance in Medicine,* vol. 70, no. 2, pp. 584-594, 2013.

[56] M. Poole, R. Bowtell, D. Green, S. Pittard, A. Lucas, R. Hawkes, and A. Carpenter, "Split gradient coils for simultaneous PET‐MRI," *Magnetic resonance in medicine,* vol. 62, no. 5, pp. 1106-1111, 2009.

[57] L. S. Petropoulos, and M. Morich, “Novel gradient coil set with an interstitial gap for interventional nuclear magnetic resonance applications,” *Magnetics, IEEE Transactions on,* vol. 33, no. 5, pp. 4107-4109, 1997.

[58] R. Kimmlingen, M. Gebhardt, J. Schuster, M. Brand, F. Schmitt, and A. Haase, “Gradient system providing continuously variable field characteristics,” *Magnetic resonance in medicine,* vol. 47, no. 4, pp. 800-808, 2002.

[59] S. Shvartsman, M. Morich, G. Demeester, and Z. Zhai, “Ultrashort shielded gradient coil design with 3D geometry,” *Concepts in Magnetic Resonance Part B: Magnetic Resonance Engineering,* vol. 26, no. 1, pp. 1-15, 2005.

[60] J. A. Overweg, V. Schulz, T. Solf, G. D. DeMeester, and M. A. Morich, "Split gradient coil and PET/MRI hybrid system using the same," Google Patents, 2012.

[61] V. Vegh, and Q. M. Tieng, "Wrapped edge gradient coil for MRI-PET animal imaging." p. 1526.

[62] L. Liu, H. S. Lopez, M. Poole, F. Liu, and S. Crozier, “Simulation and analysis of the interactions between split gradient coils and a split magnet cryostat in an MRI–PET system,” *Journal of Magnetic Resonance,* vol. 222, pp. 8-15, 2012.

[63] F. Liu, and S. Crozier, “An FDTD model for calculation of gradient-induced eddy currents in MRI system,” *Applied Superconductivity, IEEE Transactions on,* vol. 14, no. 3, pp. 1983-1989, 2004.

[64] C. Ham, J. Engels, G. Van de Wiel, and A. Machielsen, “Peripheral nerve stimulation during MRI: effects of high gradient amplitudes and switching rates,” *Journal of Magnetic Resonance Imaging,* vol. 7, no. 5, pp. 933-937, 1997.

[65] J. A. Den Boer, J. D. Bourland, J. A. Nyenhuis, C. L. Ham, J. M. Engels, F. X. Hebrank, G. Frese, and D. J. Schaefer, “Comparison of the threshold for peripheral nerve stimulation during gradient switching in whole body MR systems,” *Journal of Magnetic Resonance Imaging,* vol. 15, no. 5, pp. 520-525, 2002.

[66] H. Sanchez Lopez, M. Poole, and S. Crozier, “An improved equivalent magnetization current method applied to the design of local breast gradient coils,” *Journal of Magnetic Resonance,* vol. 199, no. 1, pp. 48-55, 2009.

[67] R. Turner, D. Le Bihan, J. Maier, R. Vavrek, L. K. Hedges, and J. Pekar, “Echo-planar imaging of intravoxel incoherent motion,” *Radiology,* vol. 177, no. 2, pp. 407-414, 1990.

[68] P. B. Roemer, "Transverse gradient coils for imaging the head," Google Patents, 1993.

[69] A. Abduljalil, A. Aletras, and P. M. Robitaille, "Torque free asymmetric gradient coils for echo planar imaging," *Magnetic resonance in medicine,* vol. 31, no. 4, pp. 450-453, 1994.

[70] R. Kimmlingen, E. Eberlein, M. Gebhardt, B. Hartinger, R. Ladebeck, R. Lazar, T. Reese, J. Riegler, F. Schmitt, and G. Sorensen, "An easy to exchange high performance head gradient insert for a 3T whole body MRI system: first results," *Proc. Intl. Soc. Magn. Reson. Med. Sci. Meet. Exhib,* vol. 11, pp. 1630, 2004.

[71] J. Cohen-Adad, J. McNab, T. Benner, M. Descoteaux, A. Mareyam, V. Wedeen, and L. Wald, "Improving high-resolution Q-Ball imaging with a head insert gradient: Bootstrap and SNR analysis." p. 1606.

[72] T. Vaughan, L. DelaBarre, C. Snyder, J. Tian, C. Akgun, D. Shrivastava, W. Liu, C. Olson, G. Adriany, and J. Strupp, "9.4 T human MRI: preliminary results," *Magnetic resonance in medicine,* vol. 56, no. 6, pp. 1274-1282, 2006.

[73] R. Bowtell, and A. Peters, "Analytic approach to the design of transverse gradient coils with co‐axial return paths," *Magnetic resonance in medicine,* vol. 41, no. 3, pp. 600-608, 1999.

[74] S. K. Lee, J. B. Mathieu, D. Graziani, J. Piel, E. Budesheim, E. Fiveland, C. J. Hardy, E. T. Tan, B. Amm, and T. K. F. Foo, "Peripheral nerve stimulation characteristics of an asymmetric head‐only gradient coil compatible with a high‐channel‐count receiver array," *Magnetic Resonance in Medicine,* 2015.

[75] B. C. A. Jean-Baptiste Mathieu, Silke Lechner-Greite, Seung-Kyun Lee, Ek Tsoon Tan, Thomas K-F Foo, John F Schenck, Matt A Bernstein, and John Huston, "Design of High Performance Gradient Coil for 3T Head Specialty Scanner," *International Society for Magnetic Resonance in Medicine*, pp. 2588, 2012.

[76] L. Liu, H. Sanchez-Lopez, F. Liu, and S. Crozier, "Flanged-edge transverse gradient coil design for a hybrid LINAC-MRI system," *Journal of Magnetic Resonance,* vol. 226, pp. 70-78, 2013.

[77] H. Sanchez Lopez, F. Freschi, A. Trakic, E. Smith, J. Herbert, M. Fuentes, S. Wilson, L. Liu, M. Repetto, and S. Crozier, "Multilayer integral method for simulation of eddy currents in thin volumes of arbitrary geometry produced by MRI gradient coils," *Magnetic Resonance in Medicine,* 2013.

[78] S. Pissanetzky, "Minimum energy MRI gradient coils of general geometry," *Measurement Science and Technology,* vol. 3, no. 7, pp. 667, 1992.

[79] M. S. Poole, "Improved equipment and techniques for dynamic shimming in high field MRI," Sir Peter Mansfield Magnetic Resonance Centre, University of Nottingham, 2007.

[80] S. Hidalgo‐Tobon, "Theory of gradient coil design methods for magnetic resonance imaging," *Concepts in Magnetic Resonance Part A,* vol. 36, no. 4, pp. 223-242, 2010.

[81] R. Turner, "Minimum inductance coils," *Journal of Physics E: Scientific Instruments,* vol. 21, no. 10, pp. 948, 1988.

[82] R. Turner, "Gradient coil design: a review of methods," *Magnetic Resonance Imaging,* vol. 11, no. 7, pp. 903-920, 1993.

[83] R. Bowtell, and P. Robyr, "Multilayer gradient coil design," *Journal of Magnetic Resonance,* vol. 131, no. 2, pp. 286-294, 1998.

[84] C. Boesch, R. Gruetter, and E. Martin, "Temporal and spatial analysis of fields generated by eddy currents in superconducting magnets: optimization of corrections and quantitative characterization of magnet/gradient systems," *Magnetic resonance in medicine,* vol. 20, no. 2, pp. 268-284, 1991.

[85] L. Liu, H. Sanchez-Lopez, M. Poole, F. Liu, and S. Crozier, "Simulation and analysis of the interactions between split gradient coils and a split magnet cryostat in an MRI–PET system," *Journal of Magnetic Resonance,* vol. 222, pp. 8-15, 2012.

[86] J. R. Foster, D. A. Hall, A. Q. Summerfield, A. R. Palmer, and R. W. Bowtell, "Sound‐Level Measurements and Calculations of Safe Noise Dosage During EPI at 3 T," *Journal of Magnetic Resonance Imaging,* vol. 12, no. 1, pp. 157-163, 2000.

[87] W. A. Edelstein, T. K. Kidane, V. Taracila, T. N. Baig, T. P. Eagan, Y. C. N. Cheng, R. W. Brown, and J. A. Mallick, "Active‐passive gradient shielding for MRI acoustic noise reduction," *Magnetic resonance in medicine,* vol. 53, no. 5, pp. 1013-1017, 2005.

[88] T. Reese, O. Heid, R. Weisskoff, and V. Wedeen, "Reduction of eddy‐current‐induced distortion in diffusion MRI using a twice‐refocused spin echo," *Magnetic Resonance in Medicine,* vol. 49, no. 1, pp. 177-182, 2003.

[89] J. Kroot, S. van Eijndhoven, and A. van de Ven, "Eddy currents in a gradient coil, modeled as circular loops of strips," *Journal of Engineering Mathematics,* vol. 57, no. 4, pp. 333-350, 2007.

[90] J. Van Vaals, and A. Bergman, "Optimization of eddy-current compensation," *Journal of Magnetic Resonance (1969),* vol. 90, no. 1, pp. 52-70, 1990.

[91] P. Jehenson, M. Westphal, and N. Schuff, "Analytical method for the compensation of eddy-current effects induced by pulsed magnetic field gradients in NMR systems," *Journal of Magnetic Resonance (1969),* vol. 90, no. 2, pp. 264-278, 1990.

[92] R. Turner, and R. Bowley, "Passive screening of switched magnetic field gradients," *Journal of Physics E: Scientific Instruments,* vol. 19, no. 10, pp. 876-879, 1986.

[93] P. Mansfield, and B. Chapman, "Active magnetic screening of coils for static and time-dependent magnetic field generation in NMR imaging," *Journal of Physics E: Scientific Instruments,* vol. 19, no. 7, pp. 540, 1986.

[94] P. Mansfield, and B. Chapman, "Multishield active magnetic screening of coil structures in NMR," *Journal of Magnetic Resonance (1969),* vol. 72, no. 2, pp. 211-223, 1987.

[95] D. F. a. E. Eberlein, "The New, High-Performance MR Gradient System XR 80/200. Design, Benefits and Safe Operation," 2013.

[96] Y. Chen, R. Mittra, and P. Harms, "Finite-difference time-domain algorithm for solving Maxwell's equations in rotationally symmetric geometries," *Microwave Theory and Techniques, IEEE Transactions on,* vol. 44, no. 6, pp. 832-839, 1996.

[97] A. Canova, G. Gruosso, and M. Repetto, "Integral methods for analysis and design of low-frequency conductive shields," *Magnetics, IEEE Transactions on,* vol. 39, no. 4, pp. 2009-2017, 2003.

[98] H. Sanchez Lopez, M. Poole, and S. Crozier, "Eddy current simulation in thick cylinders of finite length induced by coils of arbitrary geometry," *Journal of Magnetic Resonance,* vol. 207, no. 2, pp. 251-261, 2010.

[99] H. Sanchez Lopez, F. Liu, M. Poole, and S. Crozier, "Equivalent magnetization current method applied to the design of gradient coils for magnetic resonance imaging," *Magnetics, IEEE Transactions on,* vol. 45, no. 2, pp. 767-775, 2009.

[100] C. Cobos Sanchez, S. G. Garcia, L. D. Angulo, C. M. De Jong Van Coevorden, and A. Rubio Bretones, "A divergence-free BEM method to model quasi-static currents: Application to MRI coil design," *Progress In Electromagnetics Research B,* vol. 20, pp. 187-203, 2010.

[101] R. A. Lemdiasov, and R. Ludwig, "A stream function method for gradient coil design," *Concepts in Magnetic Resonance Part B: Magnetic Resonance Engineering,* vol. 26, no. 1, pp. 67-80, 2005.

[102] K. J. Binns, C. Trowbridge, and P. Lawrenson, *The analytical and numerical solution of electric and magnetic fields*: Wiley, 1992.

[103] D. R. Wilton, A. Glisson, D. Schaubert, O. Al-Bundak, and C. M. Butler, "Potentials integrals for uniform and linear source distributions on polygonal and polyhedral domains," *IEEE Transactions on Antennas and Propagation,* vol. 32, no. 3, pp. 276-281, 1984.

[104] R. D. Graglia, "On the numerical integration of the linear shape functions times the 3-D Green's function or its gradient on a plane triangle," *Antennas and Propagation, IEEE Transactions on,* vol. 41, no. 10, pp. 1448-1455, 1993.

[105] F. Freschi, and M. Repetto, "A general framework for mixed structured/unstructured PEEC modelling," *APPLIED COMPUTATIONAL ELECTROMAGNETICS SOCIETY JOURNAL,* vol. 23, pp. 200-206, 2008.

[106] T. F. Eibert, and V. Hansen, "On the calculation of potential integrals for linear source distributions on triangular domains," *Antennas and Propagation, IEEE Transactions on,* vol. 43, no. 12, pp. 1499-1502, 1995.

[107] D. Sievers, T. F. Eibert, and V. Hansen, "Correction to "On the calculation of potential integrals for linear source distributions on triangular domains"," *Antennas and Propagation, IEEE Transactions on,* vol. 53, no. 9, pp. 3113-3113, 2005.

[108] H. Sanchez Lopez, F. Freschi, A. Trakic, E. Smith, J. Herbert, M. Fuentes, S. Wilson, L. Liu, M. Repetto, and S. Crozier, "Multilayer integral method for simulation of eddy currents in thin volumes of arbitrary geometry produced by MRI gradient coils," *Magnetic Resonance in Medicine,* vol. 71, no. 5, pp. 1912-1922, 2014.

[109] P. J. Basser, J. Mattiello, and D. LeBihan, "MR diffusion tensor spectroscopy and imaging," *Biophysical journal,* vol. 66, no. 1, pp. 259, 1994.

[110] P. Mansfield, "Multi-planar image formation using NMR spin echoes," *Journal of Physics C: Solid State Physics,* vol. 10, no. 3, pp. L55, 1977.

[111] R. Turner, and D. Le Bihan, "Single-shot diffusion imaging at 2.0 Tesla," *Journal of Magnetic Resonance (1969),* vol. 86, no. 3, pp. 445-452, 1990.

[112] E. C. Wong, A. Jesmanowicz, and J. S. Hyde, "High-resolution, short echo time MR imaging of the fingers and wrist with a local gradient coil," *Radiology,* vol. 181, no. 2, pp. 393-397, 1991.

[113] R. Turner, R. Vavrek, J. Maier, and D. Le Bihan, "EPI diffusion imaging of the brain at 1.5 Tesla without motion artifact using a localized head gradient coil." p. 1123.

[114] D. Tomasi, R. Xavier, B. Foerster, H. Panepucci, A. Tannús, and E. Vidoto, "Asymmetrical gradient coil for head imaging," *Magnetic resonance in medicine,* vol. 48, no. 4, pp. 707-714, 2002.

[115] W. B. Handler, C. T. Harris, T. J. Scholl, D. L. Parker, K. C. Goodrich, B. Dalrymple, F. Sass, and B. A. Chronik, "New head gradient coil design and construction techniques," *Journal of Magnetic Resonance Imaging,* vol. 39, no. 5, pp. 1088-1095, 2014.

[116] E. Smith, F. Freschi, M. Repetto, and S. Crozier, "A Method for Reducing Secondary Field Effects in Asymmetric MRI Gradient Coil Design," *IEEE Transactions on Biomedical Engineering,* vol. 63, no. 5, pp. 924-932, 2016.

[117] M. S. Poole, and N. Jon Shah, "Convex optimisation of gradient and shim coil winding patterns," *Journal of Magnetic Resonance,* vol. 244, pp. 36-45, 2014.

[118] F. Tang, F. Liu, F. Freschi, Y. Li, M. Repetto, L. Giaccone, Y. Wang, and S. Crozier, "An improved asymmetric gradient coil design for high-resolution MRI head imaging," *Physics in Medicine and Biology,* 2016 (accepted).

[119] M. S. Poole, P. T. While, H. Sanchez Lopez, and S. Crozier, "Minimax current density gradient coils: analysis of coil performance and heating," *Magnetic Resonance in Medicine,* vol. 68, no. 2, pp. 639-648, 2012.

[120] K. C. Chu, and B. K. Rutt, "MR gradient coil heat dissipation," *Magnetic resonance in medicine,* vol. 34, no. 1, pp. 125-132, 1995.

[121] S. M. Lechner-Greite, J. Mathieu, and B. C. Amm, "Simulation Environment to Predict the Effect of Eddy Currents on Image Quality in MRI," *Applied Superconductivity, IEEE Transactions on,* vol. 22, no. 3, pp. 4402104-4402104, 2012.

[122] F. Tang, F. Freschi, H. Sanchez Lopez, M. Repetto, F. Liu, and S. Crozier, "Intra-coil interactions in split gradient coils in a hybrid MRI-LINAC system," *Journal of Magnetic Resonance,* 2016.

[123] A. Ganin, and K. F. King, "Automatic measurement of gradient field distortion," Google Patents, 2001.

[124] R. Wysong, D. Madio, and I. J. Lowe, "A novel eddy current compensation scheme for pulsed gradient systems," *Magnetic resonance in medicine,* vol. 31, no. 5, pp. 572-575, 1994.

[125] R. Bowtell, and P. Mansfield, “Gradient coil design using active magnetic screening,” *Magnetic resonance in medicine,* vol. 17, no. 1, pp. 15-21, 1991.

[126] S. Crozier, and D. M. Doddrell, “Gradient-coil design by simulated annealing,” *Journal of Magnetic Resonance, Series A,* vol. 103, no. 3, pp. 354-357, 1993.

[127] G. N. Peeren, “Stream function approach for determining optimal surface currents,” *Journal of Computational Physics,* vol. 191, no. 1, pp. 305-321, 2003.

[128] M. Poole, and R. Bowtell, “Novel gradient coils designed using a boundary element method,” *Concepts in Magnetic Resonance Part B: Magnetic Resonance Engineering,* vol. 31, no. 3, pp. 162-175, 2007.

[129] H. S. Lopez, M. Poole, and S. Crozier, “An improved equivalent magnetization current method applied to the design of local breast gradient coils,” *Journal of Magnetic Resonance,* vol. 199, no. 1, pp. 48-55, 2009.

[130] M. A. Brideson, L. K. Forbes, and S. Crozier, “Determining complicated winding patterns for shim coils using stream functions and the target‐field method,” *Concepts in Magnetic Resonance,* vol. 14, no. 1, pp. 9-18, 2002.

[131] M. Urdaneta, R. Probst, P. Stepanov, I. Weinberg, and S. Fricke, "Goodbye wires and formers: 3-D additive manufacturing and fractal cooling applied to construction of MRI gradient coils." pp. 2479-2482.

[132] J. M. B. Kroot, *Analysis of eddy currents in a gradient coil*: Springer, 2006.

[133] H. S. Lopez, F. Liu, M. Poole, and S. Crozier, “Equivalent magnetization current method applied to the design of gradient coils for magnetic resonance imaging,” *Magnetics, IEEE Transactions on,* vol. 45, no. 2, pp. 767-775, 2009.

[134] A. Kameari, “Transient eddy current analysis on thin conductors with arbitrary connections and shapes,” *Journal of Computational Physics,* vol. 42, no. 1, pp. 124-140, 1981.

[135] C. Geuzaine, and J.-F. Remacle, “Gmsh,” 2009.

[136] M. Poole, P. Weiss, H. S. Lopez, M. Ng, and S. Crozier, “Minimax current density coil design,” *Journal of Physics D: Applied Physics,* vol. 43, no. 9, pp. 095001, 2010.

[137] M. S. Poole, P. T. While, H. S. Lopez, and S. Crozier, “Minimax current density gradient coils: analysis of coil performance and heating,” *Magnetic Resonance in Medicine,* vol. 68, no. 2, pp. 639-648, 2012.

[138] P. T. While, J. G. Korvink, N. J. Shah, and M. S. Poole, “Theoretical design of gradient coils with minimum power dissipation: Accounting for the discretization of current density into coil windings,” *Journal of Magnetic Resonance,* vol. 235, pp. 85-94, 2013.

[139] M. A. Richard, N. J. Mastandrea Jr, and D. A. Lampman, "Gradient coils with reduced eddy currents," Google Patents, 1998.

[140] A. Trakic, H. Wang, F. Liu, H. S. Lopez, and S. Crozier, “Analysis of transient eddy currents in MRI using a cylindrical FDTD method,” *Applied Superconductivity, IEEE Transactions on,* vol. 16, no. 3, pp. 1924-1936, 2006.

[141] M. Poole, H. Sanchez Lopez, O. Ozaki, H. Kitaguchi, I. Nakajima, S. Urayama, K.-I. Sato, H. Fukuyama, and S. Crozier, “Simulation of gradient-coil-induced eddy currents and their effects on a head-only HTS MRI magnet,” *Applied Superconductivity, IEEE Transactions on,* vol. 21, no. 6, pp. 3592-3598, 2011.

[142] M. A. Morich, J. L. Patrick, and G. D. DeMeester, "Magnetic resonance gradient sheet coils," Google Patents, 1995.

[143] I. V. Kinanen, "Arrangement to minimize eddy currents in MR imagers," Google Patents, 1996.

[144] C. L. G. Ham, and J. Konijn, "MRI apparatus," Google Patents, 2004.

[145] D. Fischer, and E. Eberlein, “The New, High-Performance MR Gradient System XR 80/200. Design, Benefits and Safe Operation,” *MAGNETOM Flash. 2/2013.* www.siemens.com/magnetom-world 2013.

[146] L. L. Grigsby, *Electric power generation, transmission, and distribution*: CRC press, 2012.

[147] F. Romeo, and D. Hoult, “Magnet field profiling: analysis and correcting coil design,” *Magnetic Resonance in Medicine,* vol. 1, no. 1, pp. 44-65, 1984.

[148] W. A. Edelstein, and F. Schenck, "Current streamline method for coil construction," Google Patents, 1989.

[149] P. D. Agarwal, “Eddy-current losses in solid and laminated iron,” *American Institute of Electrical Engineers, Part I: Communication and Electronics, Transactions of the,* vol. 78, no. 2, pp. 169-181, 1959.

[150] Y. Chung, and J. Galayda, *Effect of Eddy Current in the Laminations on the Magnet Field*, Argonne National Laboratory, 1992.

[151] M. G. Sementchenko, "Gradient coils for magnetic resonance meeting," Google Patents, 2000.

[152] J. Gyselinck, L. Vandevelde, J. Melkebeek, P. Dular, F. Henrotte, and W. Legros, "Calculation of eddy currents and associated losses in electrical steel laminations," *Magnetics, IEEE Transactions on*, vol. 35, no. 3, pp. 1191-1194, 1999.

[153] Y. Wang, F. Liu, Y. Li, F. Tang, and S. Crozier, "Asymmetric gradient coil design for use in a short, open bore magnetic resonance imaging scanner," *Journal of Magnetic Resonance*, 2016.